# Memristive Crossbar Array-based Frameworks for Image Analysis and Classification

**Ph.D. Thesis**


**By**

**Kumari Jyoti**



**DEPARTMENT OF ELECTRICAL ENGINEERING**

**INDIAN INSTITUTE OF TECHNOLOGY INDORE**



**NOVEMBER 2024**

# Memristive Crossbar Array-based Frameworks for Image Analysis and Classification

**A THESIS**

*Submitted in partial fulfillment of the requirements for the award of the degree*

*of*

**DOCTOR OF PHILOSOPHY**

*by*

**KUMARI JYOTI**

**DEPARTMENT OF ELECTRICAL ENGINEERING**

**INDIAN INSTITUTE OF TECHNOLOGY INDORE**

**NOVEMBER 2024**

# INDIAN INSTITUTE OF TECHNOLOGY INDORE

## CANDIDATE'S DECLARATION

I hereby certify that the work which is being presented in the thesis entitled **"Memristive Crossbar Array-based Frameworks for Image Analysis and Classification"** in the partial fulfilment of the requirements for the award of the degree of **Doctor of Philosophy** and submitted in the **Department of Electrical Engineering, Indian Institute of Technology Indore**, is an authentic record of my own work carried out during the time period from **October, 2019** to **November, 2024** under the joint supervision of **Prof. Shaibal Mukherjee**, Professor, Department of Electrical Engineering, IIT Indore and **Prof. Ram Bilas Pachori**, Professor, Department of Electrical Engineering, IIT Indore.

The matter presented in this thesis has not been submitted by me for the award of any other degree of this or any other institute.

Jyoti Tiwari. 13-05-2025

Signature of the student with date

**KUMARI JYOTI**

---

This is to certify that the above statement made by the candidate is correct to the best of our knowledge.

S. Mukherjee 13/5/2025

Signature of Thesis Supervisor #1 with date

**(PROF. SHAIBAL MUKHERJEE)**

13.05.2025

Signature of Thesis Supervisor #2 with date

**(PROF. RAM BILAS PACHORI)**

---

Kumari Jyoti has successfully given her Ph.D. Oral Examination held on 13th May 2025.

S. Mukherjee 13/5/2025

Signature of Thesis Supervisor #1 with date

**(PROF. SHAIBAL MUKHERJEE)**

13.05.2025

Signature of Thesis Supervisor #2 with date

**(PROF. RAM BILAS PACHORI)**

---

**ACKNOWLEDGEMENTS**

First of all, I would like to express my sincere appreciation to my thesis supervisor **Prof. Shaibal Mukherjee** and **Prof. Ram Bilas Pachori**, Professor, Department of Electrical Engineering IIT Indore for his generous guidance, support, monitoring, constant encouragement, timely suggestions and the detailed discussion without which this work would not have been possible. He consistently allowed this thesis to be my own work, but he steered me in the right direction whenever he thought I needed it.

I am extremely grateful to my doctoral committee members **Prof. Vimal Bhatia** and **Dr. Sumanta Samal** for their encouragement, valuable advice, questions, insightful comments and co-operation throughout the work.

My sincere thanks go to **Prof. Suhas S. Joshi**, Director, IIT Indore for providing the essential experimental facilities. I want to acknowledge the support provided by sophisticated instrumentation center (SIC) at IIT Indore.

I would like to express my sincere gratitude to Ministry of Human Resource Development (MHRD) or Ministry of Education (MoE), Government of India, for providing me doctoral fellowship from October 2019 to March, 2023. In addition, I would like to thank Technology innovation hub, TIH-IOT foundation, IIT Bombay for providing me with a doctoral fellowship from March 2023 to October, 2024 under the TIH-IoT CHANAKYA Fellowship Program. I would also like to thank IIT Indore for providing national travel grant to attend and present a research work.

I would like to express my wholehearted thanks to Hybrid Nanodevice Research Group (HNRG) and Signal Analysis Research Lab (SARL) past and present members for their help and support during the research work. I want to express my gratitude to my close friends for their unwavering support and assistance that has been invaluable throughout this journey and completing it would have been impossible without their moral encouragement. I would also like to express my gratitude to my friends and teachers from graduation, post graduations and Ph.D. for continually inspiring me at various times.

Above all, my deepest gratitude is reserved for my family: **Mr. Balmeshwar Tiwari (**Grandfather**), Mr. Krishna Nandan Tiwari (**Father**), Mrs. Shail Kumari (**Mother**),** and my sisters**, Ms. Kumari Uma, Ms. Kumari Asha, and Ms. Khushboo Tiwari.** Their endless love, care, support, and encouragement have been my greatest source of strength. I couldn't have imagined completing this challenging journey without their unwavering presence by my side.

Finally, a special acknowledgment with my deepest gratitude goes to **Dr. Ranveer Singh**, my mentor and my love, for being my rock through the final phase of this journey. His unwavering support and guidance have not only shaped my professional path but have also enriched my personal life in ways I could never have imagined.

KUMARI JYOTI

***Dedicated to my family and friends***

# LIST OF PUBLICATIONS

(A) Outcomes from Ph.D. thesis work:

A1. In refereed journals:

1. **Kumari Jyoti**, Mohit Gautam, Sanjay Kumar, Sai Sushma, Ram Bilas Pachori, Shaibal Mukherjee, “Memristive Crossbar Array-based Computing Framework for DWT with Application in Medical Image Processing”, *IEEE Transactions on Emerging Topics in Computing*, pp. 766-779, vol. 12, no. 3, 2024. (**IF: 5.9**)
2. **Kumari Jyoti**, Sai Sushma, Saurabh Yadav, Pawan Kumar, Ram Bilas Pachori, Shaibal Mukherjee, “Automatic Diagnosis of COVID-19 with MCA inspired TQWT-based Classification of Chest X-ray Images”, *Computer in Biology and Medicine*, vol. 152, no. 106331, pp. 1-11, January 2023. (**IF: 7.7**)
3. **Kumari Jyoti**, Saurabh Yadav, Chandrabhan Patel, Mayank Dubey, Pradeep Kumar Chaudhary, Ram Bilas Pachori, and Shaibal Mukherjee, “Implementation of FBSE-EWT Method in Memristive Crossbar Array Framework for Automated Glaucoma Diagnosis from Fundus Images,” *Biomedical Signal Processing and Control*, Accepted, 2024. (**IF: 5.1**)
4. **Kumari Jyoti**, Lokesh Kumar Hindoliya, Chandrabhan Patel, Mayank Dubey, Sumit Chaudhary, Ram Bilas Pachori, and Shaibal Mukherjee, “Memristive Model based Automated Framework for Pneumonia Classification,” *Progress in Artificial Intelligence*. (**IF: 2.0**) [Under Review]
5. **Kumari Jyoti**, Lokesh Kumar Hindoliya, Animesh Paul, Saurabh Yadav, Manoj Kumar, Deepak Kumar, Ram Bilas Pachori, and Shaibal Mukherjee, “Early Detection of Multiclass of Soybean Disease using Memristive Model via Leaf Images,”. [Under Submission]

A2. In refereed conferences:

1. **Kumari Jyoti**, Sai Sushma, Ram Bilas Pachori and Shaibal Mukherjee, Activation Function based on Window Function of Memristive Crossbar in Artificial Neural Network, 21st International Workshop on The Physics of Semiconductor Devices (IWPSD-2021), IIT Delhi, December 14th-17th, 2021.
2. **Kumari Jyoti**, Saurabh Yadav, Pawan Kumar, Ram Bilas Pachori and Shaibal Mukherjee, Image Processing using Memristive Crossbar Array Model based Model for Biomedical Imaging, IEEE Electron Devices Society Workshop on Devices and Circuits 2023, January 26-28, 2023. (Accepted for oral presentation)

3. **Kumari Jyoti**, Sai Sushma, Ram Bilas Pachori and Shaibal Mukherjee, Automatic Diagnosis of Infectious Lung Diseases with Memristive Crossbar Array Device-based Model using Machine Learning, 38th Madhya Pradesh Young Scientist Congress, Samrat Ashok Technological Institute, Vidisha (MP), March 17 - 19, 2023.

**B:** Other outcomes outside of the Ph.D. thesis work:

**B1. Patent:**

1. SILICON COMPATIBLE YTTRIA-BASED MEMRISTIVE CROSSBAR ARRAY AND A METHOD OF FABRICATION THEREOF. Inventors: Shaibal Mukherjee, Sanjay Kumar, Mangal Das, **Kumari Jyoti**, Patent No. 202121013663, Published, 25/06/2021. Patent No. 515267, GRANTED, February 26, 2024.

**B2. In Peer-reviewed Journals**

1. Sanjay Kumar, Rajan Agrwal, Mangal Das, **Kumari Jyoti**, Pawan Kumar, and Shaibal Mukherjee, "Analytical model for memristive systems for neuromorphic computation", *Journal of Physics D: Applied Physics*, vol. 54, (355101), 2021. **(IF: 3.4)**
2. Saurabh Yadav, Sanjay Kumar, **Kumari Jyoti**, Manoj Kumar, Deepak Singh, Yogesh Rajwade, Ram Bilas Pachori, and Shaibal Mukherjee, "Wavelet Packet Transform-enabled Memristive Crossbar Array for Soybean Leaf Early Disease Classification", *Progress in Artificial Intelligence*. (Under Review).

**B3. In Proceedings of International Conference**

1. Sumit Chaudhary, Chandrabhan Patel, Brahmadutta Mahapatra, **Kumari Jyoti**, Mayank Dubey, Saurabh Yadav, and Shaibal Mukherjee, "Ultrasensitive Detection of $Pb^{2+}$ Ions in Water using $WS_2$ Nanoflowers," 2024 IEEE 24th International Conference on Nanotechnology (NANO), Gijon, Spain, pp. 214-218, 2024.
2. Chandrabhan Patel, **Kumari Jyoti**, Mayank Dubey, Myo Than Htay, and Shaibal Mukherjee, Novel 2D transition metal dichalcogenide based memory crossbar for real-time image processing using conventional computing paradigm, EM-NANO 2023 in Kanazawa Japan, 5-8th June 2023.
3. Sumit Chaudhary, Saurabh Yadav, **Kumari Jyoti**, Pawan Kumar, Ram Bilas Pachori and Shaibal Mukherjee, Memristive Crossbar Array Model based Computing using DWT for Application in Agriculture Image Processing, IEEE

Electron Devices Society Workshop on Devices and Circuits 2023, January 26-28, 2023. (Accepted for oral presentation)

4. Sumit Chaudhary, Pawan Kumar, **Kumari Jyoti**, Myo Than Htay and Shaibal Mukherjee, Analysis of Cut-off and Maximum Oscillation Frequency of Oxide HEMT with MgO Spacer Layer, 6th Organic and Inorganic Electronics Symposium, Chuo-ku, Niigata City, Japan, June 11, 2022.
5. Sanjay Kumar, Mangal Das, **Kumari Jyoti**, Amit Shukla, Abhishek Kataria, and Shaibal Mukherjee, Analytical Modelling of $Y_2O_3$-based Memristive System for Artificial Neuron Applications, 5th IEEE International Conference on Emerging Electronics (ICEE-2020), IIT Delhi, India, November 26-28, 2020.

# TABLE OF CONTENTS

**Chapter 6: MCA Model for Early Detection of Various Soybean Diseases Through Leaf Image Analysis**



**Chapter 7: Conclusion and Future Scope**



**References**

# LIST OF FIGURES

# LIST OF FIGURES

# LIST OF TABLES

# LIST OF TABLES

# ACRONYMS

| | |
|---|---|
| 2D TMD | *Two-dimensional transition metal dichalcogenide* |
| ANN | *Artificial Neural Networks* |
| ASIC | *Application Specific Integrated Circuit* |
| CMOS | *Complementary Metal Oxide Semiconductor* |
| CNN | *Convolutional Neural Networks* |
| CT | *Computed Tomography* |
| DIBS | *Dual Ion Beam Sputtering* |
| DL | *Deep Learning* |
| EEG | *Electroencephalogram* |
| ECG | *Electrocardiogram* |
| FESEM | *Field Emission Scanning Electron Microscopy* |
| FT | *Fourier Transform* |
| FBSE-EWT | *Fourier Bessel Series Expansion Empirical Wavelet Transforms* |
| FPR | *False Positive Rate* |
| HRS | *High Resistance State* |
| HPF | *High-Pass Filter* |
| IDM | *Integrated Disease Management* |
| IoT | *Internet of Things* |
| JPEG | *Joint Photographic Experts Group* |
| LRS | *Low Resistance State* |
| LPF | *Low-Pass Filter* |
| MCA | *Memristive Crossbar Array* |
| MED | *Maximum Error Deviation* |
| MIS | *Metal-Insulator Semiconductor* |

| | |
|---|---|
| MRI | *Magnetic Resonance Imaging* |
| MSRAM | *Memristive Static Random-Access Memory* |
| MSE | *Mean Square Error* |
| ONH | *Optic Nerve Head* |
| PCNN | *Pulse Coupled Neural Network* |
| PSNR | *Peak Signal-to-Noise Ratio* |
| RDT | *Rapid Diagnostic Test* |
| RESNET | *Residual Neural Network* |
| RTPCR | *Real-Time Reverse Transcription-Polymerase Chain Reaction* |
| ROC | *Region of convergence* |
| RLE | *Run Length Encoding* |
| SARSCOV2 | *Severe Acute Respiratory Syndrome Coronavirus 2* |
| SVD | *Singular Value Decomposition* |
| SSIM | *Structural Similarity Index* |
| SVM | *Support Vector Machines* |
| TQWT | *Tunable Q-Wavelet Transform* |
| TPR | *True Positive Rate* |
| WPT | *Wavelet Packet Transform* |

# NOMENCLATURE

| | |
|---|---|
| μW | *Microwatts* |
| eV | *Electron Volts* |
| *V* | *Voltage* |
| *I* | *Current* |
| $^{o}$C | *Degree Celcius* |
| min | *Minute* |
| s | *Seconds* |
| sccm | *Standard Cubic Centimeters per Minute* |
| nm | *Nanometer* |
| Ω | *Ohm* |
| dB | *deciBel* |

# ABSTRACT

## Memristive Crossbar Array-based Frameworks for Image Analysis and Classification

by


Kumari Jyoti

Department of Electrical Engineering

Indian Institute of Technology Indore

Supervisor: Prof. Shaibal Mukherjee, and Prof. Ram Bilas Pachori



This thesis explores application of an yttrium oxide ($Y_2O_3$)-based memristive crossbar array (MCA) model, MCA developed through a dual ion beam sputtering system, for high cyclic stability in resistive switching applications. The experimentally obtained data from the fabricated MCA was validated against an analytical MCA-based model, showing excellent alignment with experimental results. Utilizing this validated model, we applied it to biomedical image processing, specifically in analysing computed tomography (CT) and magnetic resonance imaging (MRI) images, through a two-dimensional image decomposition technique. By employing varying decomposition levels and threshold values, we evaluated reconstructed image quality through metrics such as peak signal-to-noise ratio (PSNR), structural similarity index (SSIM), and mean square error (MSE). In our analysis, MRI and CT scan images exhibited compression ratios of 21.01% and 47.81% using Haar and 18.82% and 46.05% with biorthogonal wavelets. Brightness analysis showed significant improvements in image quality, with increases of 103.72% for CT scans and 18.59% for MRI images using Haar wavelets. These findings underscore the potential of the MCA-based model for image compression, facilitating reduced computation times and storage requirements in biomedical engineering.

In light of the COVID-19 pandemic, the MCA model is further applied to a two-dimensional tunable *Q*-wavelet transform (TQWT) for decomposing chest X-ray images from two distinct datasets, supporting rapid and cost-effective COVID-19 detection for further diagnosis.

TQWT achieved optimal results in terms of PSNR and SSIM at a quality factor ($Q$) of 4, oversampling rate ($r$) of 3, and decomposition level ($J$) of 2. Processed images were then classified using ResNet50 and AlexNet convolutional neural networks (CNNs), achieving average accuracies of 98.82% and 94.64% for small and large datasets, respectively, outperforming conventional deep learning methods. Compared to CMOS-based technology, the proposed approach offers enhanced accuracy with lower power, area, and cost requirements, making it a viable solution for rapid and accurate COVID-19 detection.

The MCA model also demonstrated high efficacy in detecting lung diseases like pneumonia. Using chest X-ray images from two datasets, this study employed a TQWT and MCA-based model to classify lung conditions through CNNs, achieving an average accuracy of 99.24% with EfficientNet and significant gains in efficiency over other conventional methods. Additionally, the novel $Y_2O_3$-MCA model, with a custom-designed activation function, showed a classification efficiency of 99.94%, surpassing the conventional sigmoid function.

This thesis also covers digit recognition and glaucoma detection. For digit recognition, a convolutional neural network (CNN) with a ReLU activation function was applied to the MNIST dataset, yielding efficient feature extraction and storage through a memristive system. In glaucoma detection, the integration of MCA with two-dimensional Fourier-Bessel series expansion empirical wavelet transforms (2D FBSE-EWT) and EfficientNet CNN achieved a high PSNR of 26.23 dB and SSIM of 95.38%, resulting in an impressive 94.15% accuracy in glaucoma classification. Further applications in agriculture demonstrated the model's capacity to classify soybean leaf diseases with an accuracy of 94.3%, presenting a scalable and sustainable solution for real-time disease monitoring in agriculture.

The $Y_2O_3$-based MCA model presents a versatile and powerful tool for diverse applications in biomedical imaging, disease diagnosis, and agriculture. Its robust performance in image compression, classification accuracy, and energy efficiency highlights the potential of memristive systems to address real-world challenges in cost-sensitive and data-intensive fields.

Future research will aim to integrate this memristive model with Internet of Things (IoT) devices for continuous monitoring in healthcare and agriculture, allowing for real-time data acquisition and processing. Additional work will also focus on refining classification algorithms to enhance accuracy and robustness further, making the system adaptable to various other applications in machine learning and deep learning frameworks.

# Chapter 1

# Introduction

## 1.1. Motivation

The most familiar basic circuit elements describing the relation between the parameters in a circuit like voltage ($v$), current ($i$), charge ($q$), and flux ($\phi$) are resistors, capacitors, and inductors as shown in Fig. 1.1. Leon Chua proposed a new fundamental circuit element in 1971, which would relate flux and charge and hence complete symmetry [1]. He named it the ‘memory resistor,’ or memristor, theorizing that it could retain its last applied state and switch between states accordingly. Also postulated that a memristor’s *I-V* characteristic is a unique hysteresis loop which is slightly pinched. The very first physical realization of the element was successful in 2008 when a team of HP researchers which was led by Stanley Williams fabricated a device that mimicked the *I-V* characteristics of a memristor [2]. Afterwards, the exploration in the field of memristors and its applications has been continuing [2,3].

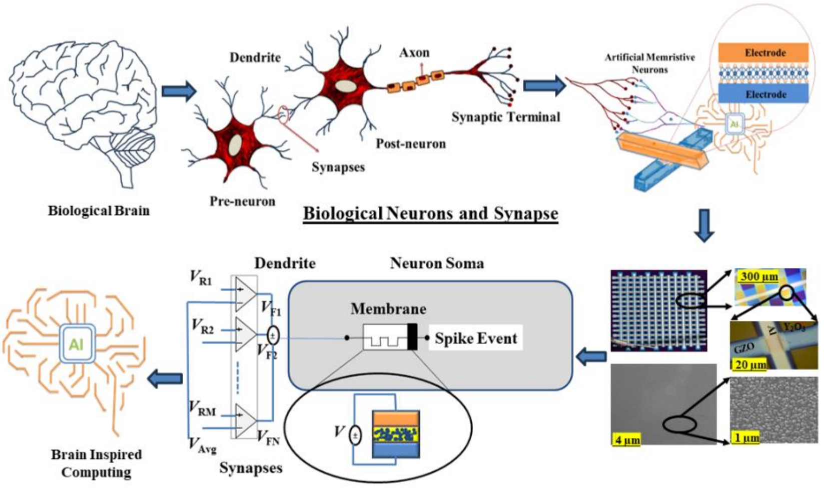


Figure 1. 1**:** *Schematic shows image processing using MCA based model*

Because a memristor's dynamic characteristic is based on the previous history of applied voltages and currents passed through it, a memristor model can be described by two different equations. One of them establishes the relationship between the current and voltage across it while the other equation establishes the relationship between the state variable, an intrinsic property of the memristor, and time [3, 4].

As shown in Fig. 1.1, the performance of the biological brain in terms of brain-inspired computing is modelled using memristive devices. In biological systems, neurons and synapses include dendrites positioned between pre-neurons and post-neurons via synapses. Information is transferred to the synaptic terminal through the axon, which functions similarly to artificial memristive neurons. This study uses an analytical model of a memristive device, featuring a structure with gallium zinc oxide (GZO) as the bottom electrode, aluminum (Al) as the top electrode, and $Y_2O_3$ as the resistive switching layer [5]. The memristive device-based model is activated by voltage (v) corresponding to pixel values $V_{R1}$, $V_{R2}$, ..., $V_{RM}$, with a normalizing voltage $V_{Avg}$. It generates spike events via the membrane, analogous to the soma of a neuron [5]. The concept of memristive biological neurons is inspired by the intricate structure and complex functioning of biological neurons found in the human brain. These artificial neurons mimic the way biological neurons process and transmit information, utilizing memristive devices to emulate synaptic behaviours such as learning and memory retention. Memristive biological neurons hold significant potential in the realm of artificial intelligence, particularly for tasks that require efficient and accurate image classification. By leveraging the unique properties of memristors, these neurons can process vast amounts of data swiftly and with high precision, thereby enhancing the performance of AI systems in recognizing and categorizing images [5]. A memristive model-based framework, characterized by lower power consumption compared to CMOS based systems, has the potential to scale these technological constraints. When it comes to tasks like pattern processing, the memristive model shows better processing speed and energy efficiency than Von Neumann circuits especially when applied to neural networks [5]. Extensive research has been conducted on utilizing memristive model for various applications, including neuromorphic computing particularly in neural network applications.

## 1.2. Memristor

A memristor device can be controlled by current, voltage, charge or flux as per the equations 1.1, 1.2, 1.3 and 1.4 given below [1]:

$$v(t) = M\big(q(t)\big)i(t) \qquad (1.1)$$

$$i(t) = W\big(\phi(t)\big)v(t) \qquad (1.2)$$

$$W(\phi) = \frac{dq(\phi)}{d\phi} \qquad (1.3)$$

$$M(q) = \frac{d\phi(q)}{dq} \qquad (1.4)$$

where *M*, the memristance, has the unit of resistance (Ω) and *W*, the memductance, has the unit of conductance ($\Omega^{-1}$) including *v*, *i*, *q*, ϕ represents voltage, current, charge and flux with time, '*t*'. The memristor acts like a resistor when there is no variation in *M*. The memristance, *M* is the functional relation between the charge held in the memristor and magnetic flux as shown in Fig. 1.2 (a). This increases when the electric current flowing through the device is in one direction. When the current flowing through the device is along the opposite direction, the memristance decreases [4-7]. Then when power supply is absent, the electrical resistance freezes until power is restored, then the memristor will remember the last state of the resistance, this is the unique property of the memristor and this property is the essence of its non-volatility which makes it suitable for many applications such as resistive random-access memory (RRAM) [8], neuromorphic computing [9], logic gates [10], etc.

Traditional architectures, such as von Neumann machines, encounter limitations when addressing the computational demands of image processing. Memory bottlenecks and data transfer inefficiencies often hinder the real-time processing of large and complex image datasets [4, 5]. Memristors, characterized by their non-volatile nature and analog resistance changes, present a paradigm shift by enabling in-memory computing directly within the storage unit. This aligns seamlessly with the requirements of image processing, where simultaneous data processing and storage are paramount [6]. The motivation extends beyond the mere optimization of computational efficiency. Memristors, when configured in crossbar arrays, exhibit neuromorphic properties, mirroring the synaptic behaviour of the human brain. This opens avenues for advanced image recognition systems that can learn and adapt, thereby enhancing the overall capabilities of image processing applications. The potential energy efficiency gains afforded by memristive image processing systems are noteworthy [7]. The non-volatile nature of memristors eliminates the constant power requirements for data retention, reducing overall power consumption. This holds significant implications for portable and edge computing devices, where energy efficiency is a critical concern.

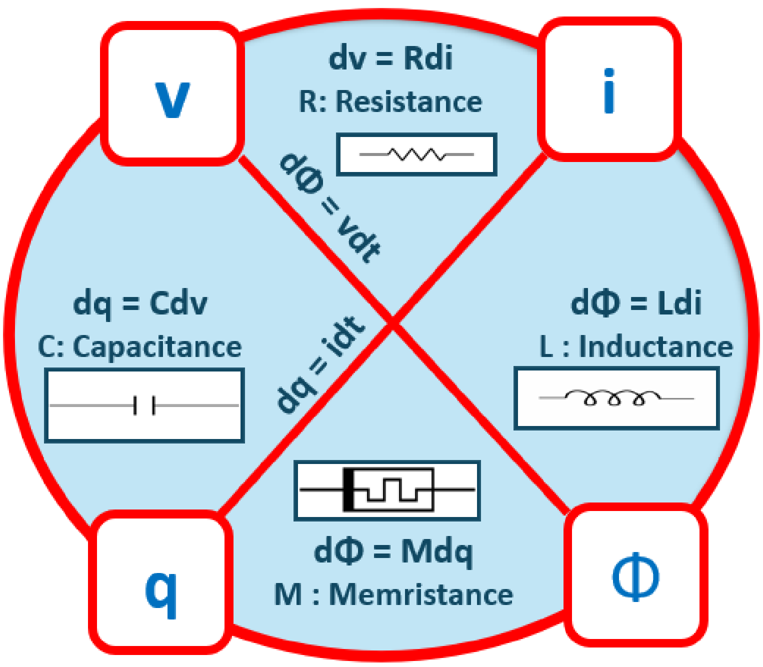


(a)

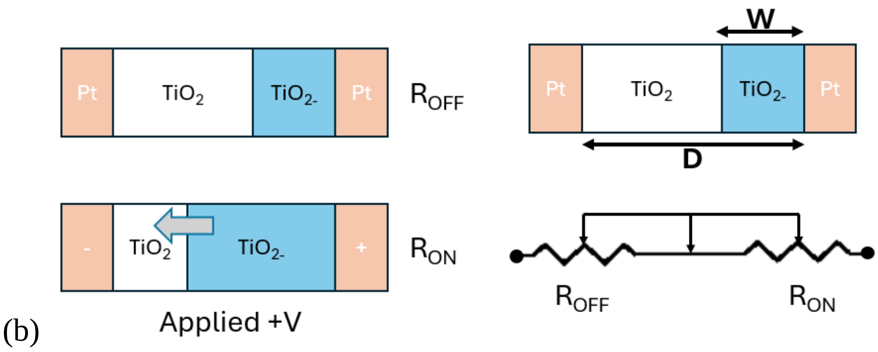


Figure 1. 2*: Relationship between (a) fundamental circuit elements and basic circuit parameters, and (b) the operation of a memristive device.*

Applications that are based on memristive devices need an appropriate model for research and during the simulation of the system. The first ever practical model of a memristor was introduced by the scientists of HP lab. The HP memristor model works on the principle of the drift of oxygen vacancies. The HP lab memristor model comprises of Pt/$TiO_2$/Pt sandwiched structure as shown in Fig.1.2. Positively charged oxygen vacancies are present on one side of the $TiO_2$ oxide layer in the HP lab's model. It is sandwiched between the two layers of platinum [11]. The doped part of oxide layer has low resistance behaviour while the high resistance behaviour is demonstrated by an undoped portion of the oxide layer. On an application of appropriate voltage, the drift of ions in the middle of doped and undoped region leads to a variation in the doped region's width, the doped region's width is considered as the state variable [12]. Also, when the doped region's width is nearly zero, the memristor reaches a high resistance state (HRS) and when the width of the region approaches a boundary, the memristor reaches a low resistance state (LRS). Since the dimensions of memristor are very small (~nm), a low excitation in the supply can lead to a variation in the doped region, in this way the resistance of the device fluctuates in between HRS and LRS [3].

## 1.3. Image Decomposition

The integration of memristors emerges as a compelling and innovative approach, motivated by the intrinsic properties of these memory resistors. Image processing tasks often demand efficient storage, rapid retrieval, and intricate pattern recognition, posing challenges to conventional computing architectures. The motivation behind incorporating memristors lies in their unique ability to revolutionize the way we handle and manipulate visual data [13].

Memristor, and the concept is used for doped and undoped interface and interface between electrodes. The doped region changes according to the input signal that has been applied. Also, in this model, the vacancies can drift over the complete length of a memristor. But it has been reported that the vacancies drift in a non-linear way near the interfaces of the boundary [14]. That is due to the non-linear drift of vacancies caused by a large electric field even for a small excitation signal. Another problem in the linear drift model is non-zero boundary conditions, i.e., the state variable never reaches zero. Which indicates the scarcity of oxygen vacancies and because of the lack of undoped region, the doped region is not able take the complete length because of which the memristor cannot work [14].

The memristive systems are promising candidates for next-generation high performance [1, 2], dense computing architecture [2-4], and data storage [3, 4] applications and could also be used to realize Boolean operations [2]. The memristor based memory architecture has offered higher density as a data storage medium as compared to common architectures [1]. Memristive system offers many outstanding physical characteristics such as non-volatile nature [2, 3], low leakage current [5], and nano-level device dimension [6]. Further, it is widely recognized that the energy consumption in memristive devices and circuits is significantly less which further attracts a substantial global interest in in-memory computation [3, 4], image processing [6], neuromorphic computation [7], and logic operations [2]. Moreover, memristive systems are being applied in various fields of image processing, such as pattern recognition and edge detection [8]. Zhu *et* *al* [9] have recently demonstrated an algorithm for memristive crossbar array (MCA)-based image enhancement. Further, Cai *et al* [10] and Mannion *et al* [8] have proposed methods for feature extraction and analysis using memristor based networks. Owing to their attractive properties such as non-volatility [5] and compatibility with the complementary metal-oxide semiconductor (CMOS) fabrication process [1, 11], memristive devices are one of the most suitable substitutes for next generation memory technologies [2, 12]. To achieve substantially high-density memories, MCA architecture is utilized which offers a matrix-like structure [13]. Such MCA-based analytical model is used for image processing by taking natural basis function for computation as it shows an analogy memory functionality and is also able to perform parallel computing tasks known as memcomputing which consists of array-like structures [14, 15]. These structures have large numbers of MCA on board were complex, and/or neuromorphic computations take place.

Our research group has demonstrated the fabrication of memristive device based on $Y_2O_3$ oxide [6, 14] and developed the analytical models [7]. These developed analytical models show a strong correlation with the reported data of fabricated MCA by incorporating the non-linear behaviour [13, 14]. Further, these models are also utilized to analyse the various neuromorphic characteristics such as learning behaviour and synaptic plasticity of the MCA and are immensely beneficial for the implementation of hardware for neural systems. $Y_2O_3$- based MCA architecture has been fabricated by utilizing a dual ion beam sputtering (DIBS) system [6]. The DIBS system is used to deposit the insulating layer, bottom electrode, and resistive switching layer as it produces high-quality thin films with better compositional stoichiometry, low surface roughness, and provides excellent adhesion at room temperature as compared to other sputtering systems [6, 14]. DIBS supports controlled deposition and provides ease of fabrication as the number of defects in different regions of the film can be suitably controlled by modifying oxygen partial pressure during thin film growth [6]. These MCA fabricated experimental results used to design analytical model, that analytical model further used in image processing.

## 1.4. Image Classification

MCA brings a new opportunity for the advancement of computer technology as well as the development of image processing, which includes importing the image via image acquisition tools, analysing, and manipulating the image. Generally, software or hardware techniques can be used to implement image compression methods [15]. Software techniques generally rely on image compression approaches by employing the forward transform phase which consists of a vector-matrix multiplication and matrix transpose. Due to large computational costs and unrealistic memory requirements, such procedures are not appropriate for real-time applications [15-17]. Furthermore, the memristor based synaptic devices with inherent learning and memory functions are more suitable for image compression methods. These synaptic devices are realized through a metal-insulator semiconductor (MIS) structure that offers nonlinear transmission characteristics, long-term plasticity, and short-term plasticity which are beneficial for the transmission and storage of compressed images [5]. In today's world of Big Data analysis and emerging IoT applications across various domains of security, healthcare [17], social media, large scientific and engineering experiments, and image compression plays a crucial role in efficient storage and fast communication by removing redundant data [4, 18].

COVID-19, caused by the novel SARS-CoV-2 virus can be understood as a type of pneumonia [19]. Patients diagnosed with COVID-19 suffer from dry cough, sore throat, and fever which may lead to organ failure [20]. The most prevalent method to diagnose COVID-19, the real-time reverse transcription-polymerase chain reaction (RT-PCR) test takes around 10 to 15 hours to produce the result, making the diagnosis process very slow [21]. Another way to diagnose COVID-19 is the rapid diagnostic test (RDT) which takes 30 minutes to give the result. Even though the RDT method is faster, it is less reliable [22]. There is a need to explore other methods for COVID-19 diagnosis, especially in a populous country like India and many countries in the Asian subcontinent. Various studies have shown that COVID-19 affects the lungs of the patient. Hence chest X-ray images of suspected patients are the most feasible method to detect COVID-19 at an early stage [4]. Clinical imaging data are one of the most crucial diagnostic bases in all COVID-19 diagnostic data. Unfortunately, drawing the target area of medical images manually is a time-consuming and laborious task. It increases the burden on the clinicians given the complexity. Therefore, computer technology can be used to diagnose the disease using medical imaging techniques [13]. Deep learning techniques, which are a subset of machine learning techniques, have been explored to diagnose COVID-19 automatically using chest X-ray images [23]. Convolutional neural networks (CNNs), specially designed for images, are a class of deep neural networks in deep learning [24]. Residual neural network (ResNet) is a deep CNN, which is used for feature extraction and classification [8]. ResNet50 has been applied in various image recognition and classification applications such as metastatic cancer recognition [9], hyperspectral image classification [10], and chromosome classification [11]. On the other hand, AlexNet is an 8-layer model with 5 convolutional layers and 3 fully connected layers [12], which has various applications in image processing like identification of maize leaf disease [13], COVID-19 virus detection, and power equipment classification [14], scene image classification [15]. ResNet50 and AlexNet are two CNN models explored in this work for the classification of chest X-ray images that are preprocessed by a wavelet decomposition technique called tunable Q-wavelet transform (TQWT) [18-25]. The images are decomposed by setting TQWT parameters, namely quality factor ($Q$), oversampling rate ($r$), and the number of decomposition levels ($J$), to their optimized values. TQWT is described in detail in the later sections. The usage of TQWT to decompose the input chest X-ray images for classification application using an MCA-based model is novel and has not been reported elsewhere to the best of the author's knowledge. Performance of proposed model computed for two-class classification of chest X-ray image databases such as COVID-19 and normal class.

The current ongoing deep learning technologies are based on CMOS circuits which have more operations in computation [17], area consumption, energy consumption [18], processing time, and power consumption [26]. These technological limitations can be overcome using the MCA as these significantly reduce the power consumption as compared to the CMOS-based conventional systems [20]. MCA is gaining popularity in various domains of image processing, such as pattern recognition and edge detection [5].

MCA is more efficient in terms of energy as well as processing time as compared to the traditional Von Neumann circuits in some applications such as pattern processing [22-27]. The energy consumption of a memristor-based RRAM is less which attracts a lot of attention to in-memory computation for various applications [17]. Various studies on memristor-based accelerator architectures and memristor-based architectures for neuromorphic applications have been previously published. In conventional CMOS-based neural networks, the neurons are represented by capacitors that are bulky and occupy a large area, thus making the integration of a large number of neurons in a chip extremely challenging. On the other hand, by representing the neural parameters with the resistance state of memristor cells [25], an MCA can work as a dot-production engine and can eliminate the data transfer overhead of numerous neural weights.

Glaucoma, primarily occurs due to an imbalance between fluid production and drainage, resulting in increased pressure on the optic nerve head (ONH) and subsequent damage [23, 24]. As a leading cause of blindness, glaucoma often manifests without early-stage symptoms [25]. The condition is characterized by elevated fluid pressure within the optic nerve, resulting from a blockage in the eye's drainage system, ultimately causing damage to the ONH [26, 27]. Deterioration of the optic nerve can be detected through fundus images, leading to structural alterations in the optic nerve head and impacting vision [27].

It is crucial to prioritize early detection and diagnosis of glaucoma owing to its cause blindness in the absence of prompt intervention [25]. Recently, biomedical imaging technique has emerged as a formidable tool for the non-invasive detection and diagnosis of a wide variety of human diseases [26]. The biomedical imaging field, stemming from the discovery of X-ray [3] has seen the development of diverse imaging models, including electromagnetic spectrum, radio, ultrasound, microscope, and others imaging techniques [5]. Moreover, eye diseases can be similarly detected early by employing biomedical imaging techniques, particularly fundus imaging [5]. Among the diseases that can be detected and diagnosed from fundus images, glaucoma detection and diagnosis is an active area of research due to the potential severity of the condition. Glaucoma can take different forms, the most common is primary open angle glaucoma, which gradually affects vision [25]. There is also angle closure glaucoma, where eye pressure suddenly spikes, requiring urgent attention [26, 27]. Some individuals experience normal tension glaucoma, where eye pressure remains normal, but vision is still in danger. Secondary glaucoma and different types can result from various eye or body conditions, making it vital to pinpoint the specific type for the right treatment and the protection of your eyesight [24]. The proposed research aims to precisely categorize fundus images, to detect signs of glaucoma or normal conditions, particularly in cases where the cup size varies. Early detection of glaucoma is paramount in preventing long-term vision loss [26].

In recent years, several automated machine-learning algorithms have been developed for glaucoma diagnosis using fundus images. Encompassing those different approaches have been explored, such as artificial neural networks (ANN) [6], support vector machines (SVM) [7], Gabor transform [8], Radon transform [9], wavelet-based decompositions [5], and deep learning (DL) techniques [11]. However, these methods employ various image preprocessing techniques, and classification algorithms using CNNs to detect glaucoma. Henceforth, DL ensemble EfficientNetb0 model using two-dimensional Fourier Bessel series expansion empirical wavelet transforms (2D FBSE-EWT) with MCA based model has shown promising performance in glaucoma detection and diagnosis compared to traditional machine learning and DL algorithms [11]. Furthermore, the traditional methods have encountered several challenges in decomposing 2D signals, due to limitations such as interference, incompatibility with non-stationary signals, lack of adaptability, and limited scale coverage [3]. While the 2D FBSE-EWT [21] is adaptive in nature, it suffers from interference and redundancy issues in image spectrum segmentation. The proposed method introduces various advantages 2D FBSE-EWT employs non-stationary basis functions, enhancing its suitability for real-world signal representation and analysis compared with Fourier transform (FT). The 2D FBSE-EWT techniques utilize grouping operations, enabling the attainment of any decomposition level in a single computation, without distortion of amplitude and phase in the filtered signal. Boundary detection in the 2D FBSE-EWT domain using the instantaneous frequency method imparts robustness to noise. 2D FBSE-EWT exclusively provides positive frequencies to real signals, facilitating the straightforward implementation of the adaptive wavelet transform. The length of 2D FBSE-EWT coefficients is half that of the signal, allowing the 2D FBSE-EWT method to effectively separate closely spaced frequency components [3, 12]. Thus, this work investigates the motivation and significance of employing 2D FBSE-EWT as an effective technique for expanding functions in such domains.

In this paper, an advanced approach is proposed using FBSE-based spectrum instead of FT based spectrum for improved segmentation and boundary identification [13, 14]. The method introduces a 2D FBSE-EWT with MCA-based model, incorporating multi-frequency scales for boundary detection. The proposed methods are then applied to fundus image decomposition and classification for glaucoma disease detection and diagnosis. 2D FBSE-EWT is particularly well-suited for non-stationary signals as it employs non-stationary Bessel functions as a basis set represented as Bessel 0 and Bessel 1 of order 0 and order 1, respectively. Unlike the FT, FBSE exclusively represents real signals with positive frequencies, simplifying the application of filter-based decomposition techniques and reducing distortion. Furthermore, 2D FBSE-EWT generates unique coefficients of the same length as the original signal, providing twice the frequency resolution compared to FT. These unique characteristics make 2D FBSE-EWT a compact representation option for wide-band signals, capitalizing on the non-stationary characteristics and amplitude modulation of Bessel functions, which can be advantageous for various applications [1-3].

Deep learning technologies currently rely on CMOS circuits, which suffer from drawbacks such as high computation operations, area consumption, energy consumption, processing time, and power consumption [15] compared to the MCA-based model. To overcome these limitations, MCA-based model offers a promising solution by significantly reducing power consumption compared to conventional CMOS-based systems [16]. The adoption of MCA-based model has gained power in image processing domains, including pattern recognition and edge detection, due to its advantages as mentioned above.

Patients who have infectious lung diseases exhibit symptoms such as fever, sore throat, and dry cough, which can ultimately lead to organ failure [1]. Pneumonia is a severe respiratory infection that can be life-threatening, especially for the elderly, infants, and individuals with compromised immune systems. Early detection is crucial for effective treatment and better patient outcomes. Leveraging advanced technologies like memristive device-based model in conjunction with CNNs offers a promising approach for improving the accuracy and speed of pneumonia detection using chest X-ray images. Although RT-

PCR is the most widely used method for detecting pneumonia, COVID-19, and lung cancer, it is a time-consuming process that takes 10 to 15 hours to provide results [2]. Therefore, densely populated countries need to explore alternative diagnostic techniques for identifying infectious lung diseases. Chest X-rays are the most effective method for identifying infectious lung diseases at an early stage since COVID-19, pneumonia, and lung cancer all affect the lungs [3]. However, manually outlining the target area of medical images is a time-consuming and labour-intensive process, placing a greater burden on clinicians.

Therefore, medical imaging techniques can automate the diagnosis process [4]. Machine learning methods, specifically deep learning techniques, have been applied to automatically diagnose infectious lung diseases by analysing chest X-ray images [5]. CNNs are a type of neural network that is particularly useful for image processing, are used for feature extraction and classification. EfficientNetb0 model of deep CNN that is used in image recognition and classification applications is used in propsed work [6]. It has been used to identify various diseases, including lung cancer, hyperspectral image classification, and chromosome identification [7-9]. Additionally, the NASNet model which consists fully connected layers and convolutional layers with varying numbers of layers, has been used for image processing in infectious lung disease detection, power equipment fault detection, and maize leaf early disease identification [10].

This research explores the application of two CNN models, EfficientNetb0 and NASNet in the classification of chest X-ray images that have been pre-processed using TQWT. [11]. Wavelet transforms, which possess the ability to localize offer multiresolution features, have found extensive usage in several image processing applications, such as edge detection and image compression. The TQWT parameters were optimized to obtain the decomposed images, which were then classified into the two classes of pneumonia and healthy chest x-ray images. This research marks the establishment of the application of TQWT in decomposing chest X-ray images for classification through the memristive model. Traditional deep learning technologies are dependent on CMOS circuits, which are restricted by significant computational operations, area demands, energy consumption, processing time constraints, and power consumption requirements [5].

A memristive model-based framework, characterized by lower power consumption compared to CMOS based systems, has the potential to scale these technological constraints. When it comes to tasks like pattern processing, the memristive model shows better processing speed and energy efficiency than Von Neumann circuits especially when applied to neural networks [5]. Extensive research has been conducted on utilizing memristor based architectures for various applications, including neuromorphic computing particularly in neural network applications.

The memristive model can function as a vector matrix multiplication, that eliminates the necessity for transferring large amounts of neural weights data, making them highly compatible substitutes for CMOS based neural networks. To address the limitations of previous studies, this research aims to optimize the TQWT parameters for image decomposition and utilize the memristive model to conduct mathematical research on the 2D TQWT for further applications in image decomposition and classification. The processed images are utilized for computational diagnosis and early disease detection of pneumonia and other infectious lung diseases via CNN models, which analyze chest X-ray images. Memristive model-based devices present an advantage in image processing due to their simultaneous storage and processing capabilities, non-volatile memory, and adaptability. This offers the potential for the development of more efficient and intelligent systems in image processing applications with cost effectiveness. The key benefits of using MCA based model in computational tasks include high density, low power consumption, and the ability to perform parallel computations, making them ideal for implementing neural networks.

Another application is performed for agriculture domain, where soybean is one of the most valuable crops globally, providing a significant source of protein and oil for human consumption and animal feed. However, soybean production is frequently threatened by a range of diseases that affect the leaves, leading to substantial yield losses and compromised crop quality. Multiclass soybean leaf disease refers to the concurrent presence of multiple disease types on soybean leaves, each caused by different pathogens with distinct symptoms and management requirements. Common soybean leaf diseases include bacterial blight, frogeye leaf spot, brown spot, downy mildew, and cercosporin leaf blight. Effective management of these diseases necessitates accurate identification, as misdiagnosis can lead to inappropriate treatment and further crop damage. Integrated disease management (IDM) strategies, which combine cultural practices, resistant varieties, chemical controls, and biological methods, are essential for mitigating the impact of these diseases. The complexity of managing multiclass soybean leaf diseases is further compounded by challenges such as pathogen evolution, climate change, and the development of resistance to fungicides and bactericides. As such, ongoing research and advancements in diagnostic tools, breeding for resistance, and understanding pathogen ecology are critical for developing sustainable management practices. This thesis aims to explore the intricacies of multiclass soybean leaf disease, emphasizing the importance of integrated management strategies and the need for continual innovation to safeguard soybean production. This research work carried out image analysis and classification using MCA based model for the application in healthcare and agriculture domain.

## 1.5. Thesis Organization

The organizational structure of the thesis is outlined as follows:

**Chapter 1** explain the proposed work focuses on improving image processing techniques using a combination of wavelet families, CNNs, and MCA. It aims to enhance images, classify elements within them, and decompose them into finer details. Wavelet transforms allow multi-resolution analysis, capturing intricate image features. CNNs excel in automatically learning and extracting features for accurate classification. MCA based model, known for their efficiency and low power consumption, will be used to accelerate these processes. This integrated approach is expected to create a robust and efficient framework for advanced image processing tasks.

**Chapter 2** Different decomposition techniques used for image decomposition in healthcare and agriculture include the Discrete Cosine Transform (DCT), Discrete Wavelet Transform (DWT), Tunable Q-Factor Wavelet Transform (TQWT), Empirical Wavelet Transform (EWT), two dimensional Fourier-Bessel Series Expansion-based Empirical Wavelet Transform (2D FBSE-EWT), and Wavelet Packet Transform (WPT). These methods help in breaking down images into their constituent parts, enabling detailed analysis and processing. This facilitates the enhancement of image quality and improves decision-making processes in healthcare for tasks such as medical imaging and diagnostics, as well as in agriculture for monitoring crop health and analysing plant characteristics.

**Chapter 3** The DWT integrated with a MCA-based model is used for biomedical image enhancement, employing Haar and biorthogonal wavelets. This approach is compared with other wavelet families, also considering optimized wavelet series and decomposition levels. This comparison aims to determine the most effective wavelet techniques for enhancing image quality, thereby improving the clarity and diagnostic value of biomedical images.

**Chapter 4** Image decomposition using the TQWT for chest X-ray images is applied to the early detection and diagnosis of pneumonia through a MCA based model. This method optimizes various TQWT parameters to produce high-quality reconstructed images, thereby improving the accuracy and reliability of lungs infection like COVID-19 and pneumonia diagnoses from chest X-ray images.

**Chapter 5** Using 2D FBSE-EWT for image decomposition facilitates the early detection of glaucoma disease using fundus images. The memristive model employed in this process saves energy, power, and area consumption due to the reduced number of operations, which directly impacts the cost of the device, making it more efficient and economical for medical diagnostics.

**Chapter 6** The focus is on the early detection of diseases in soybean crops through leaf image classification using WPT, covering multiple classes of soybean diseases identified from leaf images. The project also delineates the development of an Android/iOS application customized for real-time and remote monitoring purposes. This application offers a detailed retrospective analysis of disease occurrences in specific fields, providing insights on a daily, weekly, and monthly basis regarding the types of diseases detected in soybean crops through leaf image classification.

**Chapter 7** Thesis encapsulates a brief overview of the conducted research, highlighting its key findings and contributions. Furthermore, it delineates prospective paths for future exploration, proposing potential directions for ongoing research endeavours within this domain.

# Chapter 2

# Integration of MCA Model with Image Decomposition Techniques

## 2.1. Introduction

Image decomposition techniques have become indispensable tools in various fields, particularly in healthcare and agriculture, due to their ability to break down images into fundamental components for detailed analysis and processing. This chapter explores several prominent decomposition methods, including the Discrete Cosine Transform (DCT), Discrete Wavelet Transform (DWT), Tunable Q-Factor Wavelet Transform (TQWT), Empirical Wavelet Transform (EWT), two dimensional Fourier-Bessel Series Expansion-based Empirical Wavelet Transform (2D FBSE-EWT), and Wavelet Packet Transform (WPT). Each of these techniques offers unique advantages and applications, enhancing image quality and facilitating improved decision-making processes.

## 2.2. Discrete Wavelet Transform

Initially, the DCT is widely used in image processing for its ability to represent images in the frequency domain. It transforms spatial domain data into a sum of cosine functions at various frequencies [5]. DCT is particularly effective in compressing images, reducing the amount of data required to store high-quality images [15]. In healthcare, DCT is used in medical imaging techniques such as MRI and CT scans, where it helps in reducing noise and improving image clarity. This transformation aids in accurate diagnosis and analysis. In agriculture, DCT assists in monitoring crop health by enhancing the visualization of various plant characteristics.

The DWT enables multi-resolution analysis of images, offering both spatial and frequency domain localization with an advantage over the

DCT, which provides frequency information alone [16]. This dual localization makes DWT particularly effective for analysing non-stationary signals. In medical imaging, DWT is widely used for image denoising and compression, resulting in clearer and more precise visuals that enhance diagnostic accuracy [17]. In agricultural applications, DWT is valuable for analysing multispectral images, which plays a crucial role in assessing soil characteristics and crop health.

In this work, DWT is a powerful mathematical tool used in image processing and analysis. It decomposes a signal into different frequency components, each with a resolution matched to its scale, making it particularly effective for analysing non-stationary signals with time-varying frequency content [28-32]. The DWT has extensive applications across diverse fields, including image compression, denoising, and biomedical signal processing. By utilizing wavelet basis functions that are localized in both time and frequency domains, the DWT offers a distinct advantage over Fourier transforms, which rely on sinusoidal basis functions. This property allows wavelets to effectively represent data with sharp transitions and localized features. Through multi-resolution analysis, the DWT enables a layered examination of signals at various scales, making it a powerful tool for complex image processing tasks. It decomposes the signal into approximate (low-frequency) and detail (high-frequency) components at various levels, capturing both coarse and fine details. Filter Banks provides in the DWT is implemented using a series of high-pass and low-pass filters. The input image is passed through these filters, and the outputs are down sampled by a factor of two, separating the images into different frequency bands [15, 16].

Wavelet families have several families of wavelets, each with different characteristics. Common wavelets include Haar, Daubechies, Symlets, and Coiflets. The choice of wavelet depends on the specific application and the nature of the image being analysed as seen in K. Jyoti *et al.* There are many applications like image compression using DWT is used in image compression algorithms, such as JPEG2000 [17,32]. It allows for efficient representation of image data by concentrating energy in a few coefficients, enabling significant compression with minimal loss of quality. In image denoising, the DWT effectively reduces noise while retaining crucial features [33-42]. By applying thresholding to the detail coefficients, noise can be minimized without compromising essential information. For feature extraction, DWT plays a key role in applications like texture analysis and pattern recognition, capturing vital characteristics of the signal that aid in classification and analysis [17, 32]. In biomedical applications, DWT is used for analysing ECG, EEG, and other physiological signals. It helps in detecting abnormalities, such as arrhythmias or epileptic seizures, by isolating relevant frequency components [17]. Mathematical foundation is the original signal can be reconstructed from the approximation and detail coefficients through the inverse DWT [5]. Advantages of DWT is locality in DWT that provides both time and frequency localization, making it suitable for analysing signals with transient characteristics. Sparsity shows many natural signals have sparse representations in the wavelet domain, which is beneficial for compression and denoising [17]. Multi-resolution in the multi-resolution nature allows for analysing signals at different scales, capturing both global and local features. Also, there are limitations like shift sensitivity in DWT that can be sensitive to shifts in the input signal, leading to variations in the wavelet coefficients for similar signals with slight shifts [32]. Boundary effects at the edges of the signal, the finite length can cause artifacts due to boundary conditions. The DWT is a versatile tool in signal processing, offering unique advantages for analysing and processing non-stationary signals. Its ability to decompose signals into different frequency components with varying resolutions makes it indispensable in applications ranging from image compression to biomedical signal analysis [33]. Despite its limitations, the DWT remains a cornerstone in the field, continuously evolving with new wavelet designs and computational techniques.

## 2.3. Tunable *Q*-Factor Wavelet Transform

TQWT [18, 43-44] is an advanced wavelet transform that allows for the adjustment of the *Q*-factor, making it highly adaptable to various signal characteristics. This adaptability makes TQWT particularly useful in healthcare for analysing biomedical signals and images with varying properties. For example, TQWT can enhance the detection of subtle features in medical images, which is critical for early diagnosis of diseases. In agriculture, TQWT aids in the detailed analysis of plant and soil characteristics, leading to better crop management practices.

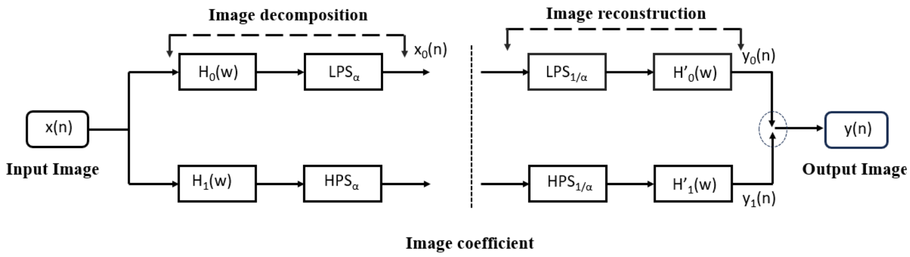


Figure 2.1: *TQWT analysis and synthesis filter bank.*

In image processing, many wavelets have limitations on their constant quality factor. Quality factor (*Q*) is a fixed parameter determined by the basis function and the number of decomposition levels. To ensure consistency in the oscillatory behavior of the image being transformed, the Q of the wavelet transform must match that of the image [11]. Most wavelet transforms, such as DWT have a fixed *Q* value that can negatively impact the quality of the reconstructed output image. To mitigate this problem, Selesnick *et al.* proposed the TQWT technique [11], which is a nonlinear signal decomposition method capable of selecting an appropriate *Q* based on the signal being decomposed. TQWT works effectively with one dimensional signal such as EEG signals, speech, and cardiac sounds [2, 7, 8]. It may also be applicable for two-dimensional signals like images with varying textures. The TQWT method comprises parameters such as *Q*, redundancy (*r*), and the number of decomposition levels (*J*), where *J*+1 sub-bands are produced for *J* decomposition levels, each represented by *v*. The proposed research employs the TQWT technique to break down chest

X-ray images from both large and small datasets by utilizing optimized $Q$, $r$, and $J$ values, as detailed in [11]. Furthermore, the MCA-based model considers the number of sub-band coefficients, referred to as '$v$' in TQWT for the application of image decomposition. The decomposed image coefficients are stored in MCA based model, where each cross point holds a coefficient value [5, 16, 17]. Input image coefficient values are fed along the rows of the memristive model, and image retrieval is performed using the current values collected along the columns, as depicted the level decomposition. CNNs are a class of deep learning models particularly effective in image processing tasks. It automatically and adaptively learns spatial hierarchies of features from input images, making them highly suitable for medical imaging applications, such as detecting pneumonia from chest X-rays images. The pre-trained CNN models employing inception residual blocks for image classification during the training process. The initial phase involves decomposing the chest X-ray images utilizing the TQWT technique, and subsequently determining the optimal values for the TQWT parameters. The decomposition parameters are then set to their optimal values for pre-processing of images. After image decomposition at each level, sub-bands with both lower and higher frequency components are obtained. At each iteration, sequential decomposition is carried out for the higher levels of the sub-bands, focusing exclusively on the coefficient originating from the approximation component. The transfer functions of the low-pass and high-pass filter banks are denoted as responses $H_0(\omega)$ and $H_1(\omega)$, respectively. In the subsequent decomposition stage, the low-pass coefficient obtained from the initial stage functions as the input. Scaling operations are applied following both the low-pass and high-pass filters at each stage. Equations (1), (2), (3), (4), and (5) demonstrate the relationships between the parameters $Q$ and $r$ and the low-pass scaling factor (LPS $\alpha$) and high-pass scaling factor (HPS $\beta$), respectively.

$$Q = (2-\beta)/\beta \tag{1}$$

$$r = \beta/(1\text{-}\alpha) \tag{2}$$

The TQWT wavelet employs the two-channel filter banks mentioned above to iteratively apply low-pass filtering to the image decomposition it into $J$+1 narrowband components. Fig. 2.1 illustrates the decomposition process for a three-layer TQWT. For perfect reconstruction, the frequency responses $H_0(\omega)$ and $H_1(\omega)$, of the TQWT must satisfy the following conditions:

$$H_0^2(\omega) + H_0^2(\omega) = 1 \tag{3}$$

Among them, $H_0(\omega)$ and $H_1(\omega)$ defined as,

$$H_0(\omega) = \begin{cases} 1, & |\omega| \leq (1-\beta)\pi, \\ \theta\left(\frac{\omega+(\beta-1)\pi}{\alpha+\beta-1}\right), & [1-\beta]\pi \leq |\omega| \leq \alpha\pi, \\ 0, & \alpha\pi \leq |\omega| \leq \pi \end{cases} \tag{4}$$

$$H_1(\omega) = \begin{cases} 0, & |\omega| \leq (1-\beta)\pi, \\ \theta\left(\frac{\alpha\pi-\omega}{\alpha+\beta-1}\right), & [1-\beta]\pi \leq |\omega| \leq \alpha\pi, \\ 1, & \alpha\pi \leq |\omega| \leq \pi \end{cases} \tag{5}$$

The identification of optimal values of $Q$, $r$, and $J$ is essential to allow TQWT to pre-process chest X-ray images. Afterward, an analytical framework is utilized to formulate a computational strategy cantered on memristive model, with the goal of effectively storing the decomposed images.

## 2.4. Fourier-Bessel Series Expansion-based Empirical Wavelet Transform

2D FBSE-EWT combines the principles of Fourier and wavelet transforms, providing a comprehensive analysis of image components. This hybrid approach is beneficial in medical imaging for enhancing image resolution and contrast, which are critical for accurate diagnosis and treatment planning. In agricultural applications, 2D FBSE-EWT facilitates detailed analysis of spectral data, aiding in the monitoring of crop development and detection of stress factors.

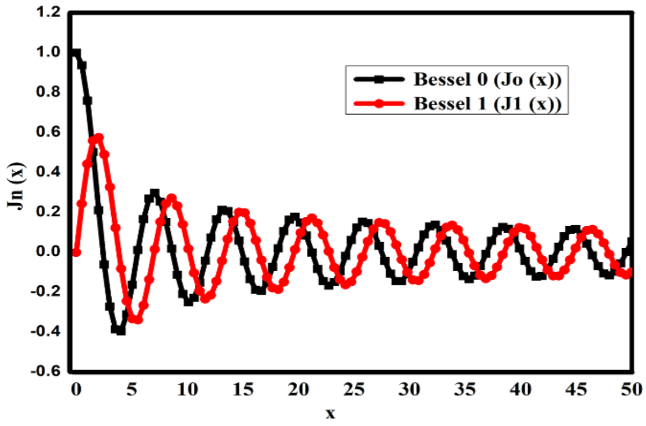


Figure 2.2: *Plot of basis functions using sine and cosine for the Fourier transform representation*

In this work, DL ensemble EfficientNetb0 model using 2D FBSE-EWT with MCA based model has shown promising performance in glaucoma detection and diagnosis compared to traditional machine learning and DL algorithms [44-46]. Furthermore, the traditional methods have encountered several challenges in decomposing 2D signals, due to limitations such as interference, incompatibility with non-stationary signals, lack of adaptability, and limited scale coverage [17]. While the 2D FBSE-EWT [39] is adaptive in nature, this method can be considered as an improved version of 2D EWT method [40]. The proposed method introduces various advantages 2D FBSE-EWT employs non-stationary basis functions, enhancing its suitability for real-world signal representation and analysis compared with FT. The 2D FBSE-EWT techniques utilize grouping operations, enabling the attainment of any decomposition level in a single computation, without distortion of amplitude and phase in the filtered signal. Boundary detection in the 2D FBSE-EWT domain using the instantaneous frequency method imparts robustness to noise. 2D FBSE-EWT exclusively provides positive frequencies to real signals, facilitating the straightforward implementation of the adaptive wavelet transform. The length of 2D FBSE-EWT coefficients is half that of the signal, allowing the 2D FBSE-EWT method to effectively separate closely spaced frequency components [23]. Thus, this work investigates the motivation and significance of employing 2D FBSE-EWT as an effective technique for expanding functions in such domains.

This work proposes an advanced approach using an FBSE-based spectrum in place of the traditional FT-based spectrum to improve segmentation and boundary identification [23]. The method introduces a 2D FBSE-EWT model integrated with an MCA-based approach, incorporating multi-frequency scales for effective boundary detection. The proposed technique is applied to fundus image decomposition and classification for the detection and diagnosis of glaucoma.

As illustrated in Fig. 2.2, the 2D FBSE-EWT is particularly suited for non-stationary signals, employing non-stationary Bessel functions (Bessel 0 and Bessel 1 of orders 0 and 1, respectively) as its basis set [17]. Unlike the FT, which represents both positive and negative frequencies, the FBSE exclusively captures real signals with positive frequencies, simplifying filter-based decomposition and reducing distortion. Additionally, the 2D FBSE-EWT produces unique coefficients that match the original signal's length, offering twice the frequency resolution of FT. These distinct properties make the 2D FBSE-EWT a compact representation for wide-band signals, leveraging the non-stationary characteristics and amplitude modulation capabilities of Bessel functions, which offer advantages across various applications [15-17].

In this work, the authors utilized first-order FBSE, as it demonstrated superior results for full-scale images compared to order zero FBSE [3], motivating its use in the proposed methodology. Mathematical expression of order one FBSE of signal $x(l)$ of length $L$ is shown in Equations (6) respectively, where $B_k$ are the coefficients of order one FBSE respectively, which are expressed in Equations (7). Here, $J_1(.)$ are Bessel functions of order one respectively. Parameter $\zeta_k$ denotes the $k^{th}$ positive roots of equation J1(.) = 0.

$$x(l) = \sum_{k=1}^{L} B_k J_1\left(\frac{\zeta_k l}{L}\right), \quad l = 0,1,\ldots,L-1 \tag{6}$$

$$B_k = \frac{2}{L^2\big(J_1(\zeta_k)\big)^2} \sum_{l=0}^{L-1} l\, x(l) J_1\left(\frac{\zeta_k l}{L}\right) \tag{7}$$

DL technologies currently rely on CMOS circuits, which suffer from drawbacks such as high computation operations, area consumption, energy consumption, processing time, and power consumption [16] compared to the MCA-based model. To overcome these limitations, MCA-based model offers a promising solution by significantly reducing power consumption compared to conventional CMOS-based systems [17]. The adoption of MCA-based model has gained power in image processing domains, including pattern recognition and edge detection, due to its advantages as mentioned

## 2.5. Wavelet Packet Transform

WPT extends the traditional wavelet transform by providing a finer decomposition of signals, making it particularly effective for analysing complex signals [47, 48]. This capability is valuable in image processing within healthcare and agriculture, as it enhances the resolution and clarity of medical images, supporting greater diagnostic accuracy. In agriculture, WPT is applied to hyperspectral images to extract detailed information about plant health and soil properties, which is crucial for precision farming.

Together, decomposition techniques such as DCT, DWT, TQWT, EWT, 2D FBSE-EWT, and WPT play a vital role in improving image quality and facilitating informed decision-making in healthcare and agriculture. By breaking down images into their fundamental components, these methods enable detailed analysis and processing, ultimately contributing to better outcomes in both fields.

# Chapter 3

# MCA-based Computing Framework for Image Enhancement and Decomposition using DWT

## 3.1. Introduction

The obtained experimental results $Y_2O_3$-based MCA are validated with an analytical MCA based model, which exhibits extremely well fitting with the corresponding experimental data. Moreover, the experimentally validated analytical model is further used for biomedical image analysis, specifically computed tomography (CT) scan and magnetic resonance imaging (MRI) images by utilizing the 2-dimensional image decomposition technique. The different levels of decomposition are used for different threshold values which help to analyse the quality of the reconstructed image in terms of peak signal-to-noise ratio (PSNR), structural similarity index (SSIM), and mean square error (MSE). For the MRI and CT scan images, at the first decomposition level, the data compression ratio of 21.01%, and 47.81% with Haar and 18.82%, and 46.05% with biorthogonal wavelet are obtained. Furthermore, the impact of brightness is also analysed which shows a sufficient increment in the quality of output image by 103.72% and 18.59% for CT scan and MRI image, respectively for Haar wavelet. The proposed MCA based model for image processing is a novel approach to reduce the computation time and storage for biomedical engineering.

## 3.2. Description of proposed techniques

Memristive systems are promising candidates for next-generation high performance [3, 49], dense computing architecture [3-5], and data storage [4, 5] applications and could also be used to realize Boolean operations [3]. The memristor based memory architecture has offered higher density as a data storage medium as compared to common architectures [49]. Memristive system offers many outstanding physical characteristics such as non-volatile nature [3, 4], low leakage current [6], and nano-level device dimension [7]. Further, it is widely recognized that the energy consumption in memristive devices and circuits is significantly less which further attracts a substantial global interest in in-memory computation [4, 5], image processing [7], neuromorphic computation [8], and logic operations [3]. Moreover, memristive systems are being applied in various fields of image processing, such as pattern recognition and edge detection [9]. Zhu *et al* [10] have recently demonstrated an algorithm for MCA model-based image enhancement.

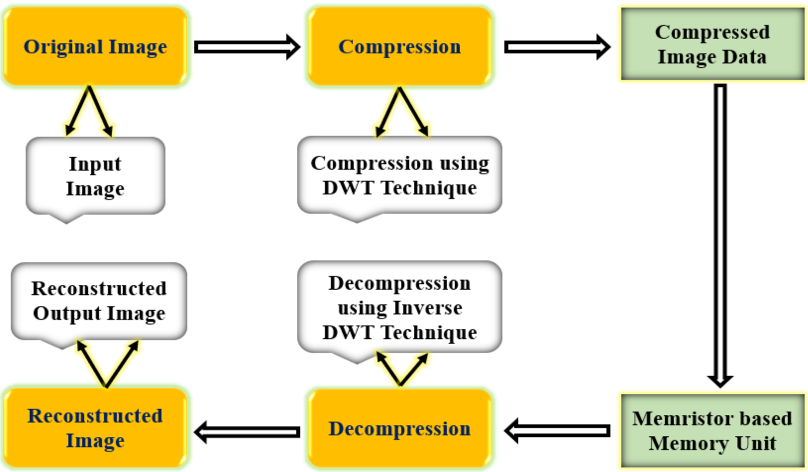


Figure 3.1: Flow chart of image processing technique using the memristive system.

Further, Cai *et al* [11] and Mannion *et al* [9] have proposed methods for feature extraction and analysis using memristor based networks. Owing to their attractive properties such as non-volatility [6] and compatibility with the CMOS fabrication process [12, 49], memristive devices are one of the most suitable substitutes for next generation memory technologies [3, 50]. To achieve substantially high-density memories, a MCA architecture is utilized which offers a matrix-like structure [13]. Such MCA-based analytical model is used for image processing by taking natural basis function for computation as it shows an analogy memory functionality and is also able to perform parallel computing tasks known as memcomputing which consists of array-like structures [14]. These structures have large numbers of MCA on board were complex, and neuromorphic computations take place.

### 3.2.1. MCA based model

Our research group has demonstrated the fabrication of memristive device based on $Y_2O_3$ oxide [6] and developed the analytical models [8]. $Y_2O_3$ has been chosen as the switching layer in the MCA due to its exceptional electrical, structural, and dielectric properties, which make it highly suitable for resistive switching applications. $Y_2O_3$ has been chosen as the switching layer in the MCA design due to several key advantages. Its wide bandgap of approximately 5.5 eV ensures excellent insulation properties and high thermal stability, which are essential for reliable resistive switching [6]. The switching mechanism in $Y_2O_3$ is primarily governed by the formation and rupture of conductive filaments composed of oxygen vacancies, enabling stable and repeatable switching characteristics [90]. Additionally, $Y_2O_3$ facilitates low-power operation due to its favourable defect chemistry and controlled oxygen vacancy dynamics, making it an ideal candidate for energy-efficient memory and neuromorphic computing applications [120]. Another significant advantage is its compatibility with CMOS technology, allowing seamless integration into conventional semiconductor fabrication processes, which is crucial for large-scale MCA implementations. Moreover, $Y_2O_3$ exhibits superior endurance and retention properties compared to other oxides, ensuring long-term reliability in memristive devices. Given these benefits, $Y_2O_3$ is a highly promising material for high-performance, non-volatile memory, neuromorphic computing, and logic-in-memory applications, making it a suitable choice for the switching layer in MCA. These developed analytical models show a strong correlation with the reported data of fabricated MCA by incorporating the non-linear behaviour [13, 14].

Further, these models are also utilized to analyse the various neuromorphic characteristics such as learning behaviour and synaptic plasticity of the MCA and are immensely beneficial for the implementation of hardware for neural systems. $Y_2O_3$ based MCA architecture has been fabricated by utilizing a dual ion beam sputtering (DIBS) system [6]. The DIBS system is used to deposit the insulating layer, bottom electrode, and resistive switching layer as it produces high-quality thin films with better compositional stoichiometry, low surface roughness, and provides excellent adhesion at room temperature as compared to other sputtering systems [6, 14]. DIBS supports controlled deposition and provides ease of fabrication as the number of defects in different regions of the film can be suitably controlled by modifying oxygen partial pressure during thin film growth [6]. XRD patterns of yttria thin films at lower temperature (100-200℃) show sharp diffraction peaks, indicating high crystallinity. yttria thin films at 300℃ exhibits a broad peak, suggesting a near-amorphous structure with short-range ordering [120]. Yttria thin films at 400℃ displays no distinct peaks, confirming its amorphous nature. Yttria thin films at 500℃ demonstrates multiple diffraction peaks, revealing a polycrystalline structure [120]. The results show a clear transition from crystalline to amorphous and back to polycrystalline structure across the samples. MCA which depicted that the deposited material layers have perfectly aligned with each other to form cross point structure.

$$I(t) = \begin{Bmatrix} a_1 x(t)\sinh\big(b_1 V(t)\big), & V_i(t) \geq 0 \\ a_2 x(t)\sinh\big(b_2 V(t)\big), & V_i(t) < 0 \end{Bmatrix} \tag{1}$$

$$dx/dt = \begin{cases} G\big(V(t)\big)e^{-\alpha_p U(x-x_p)(x-x_p)}\left(1+\left(w_p-1\right)U\left(x-x_p\right)\right), V(t) > 0 \\ G\big(V(t)\big)e^{\alpha_n U(x_p-x)(x_p-x)}\left(1+\left(w_n-1\right)U\left(x_p-x\right)\right), \; V(t) < 0 \end{cases} \tag{2}$$

$$G\big(V(t)\big) = \begin{Bmatrix} A_p\big(e^{V(t)}-1\big), & V(t) > 0 \\ -A_n\big(e^{-V(t)}-1\big), & V(t) < 0 \end{Bmatrix} \tag{3}$$

$$w_p = \frac{x_p - x}{x_n} + 1 \tag{4}$$

$$w_n = \frac{x}{x_P} \tag{5}$$

Equation (1) describes the current-voltage (*I*-*V*) relationships for the discussed MCA based model [8]. In this *I-V* equation, various variable parameters such as $a_1$, $a_2$, $b_1$, and $b_2$ are used to emulate the resistive switching response of the analytical model. Here, the fitting parameters, $b_1$, and $b_2$ are used to control the conductivity slope of the resistive switching response, and $a_1$ ($7\times10^{-4}$) and $a_2$ ($3.9\times10^{-5}$) are used as the experimental fitting parameters. The $x(t)$ is defined as a state variable and $V(t)$ is the input applied voltage. The variation in the state variable ($x(t)$) is defined by equation (2) and is influenced by a range of parameters, including the programming voltage ($G(V(t))$), control parameters for the rate of change of the state variable ($\alpha_p$, $\alpha_n$) with a value of 1.2, the magnitude of exponentials ($A_p$, $A_n$) with a value of 0.0021, and the constant values determining the boundedness of state variable represented by $x_n$ and $x_p$, set to 0.3 and 0.7, respectively.

Furthermore, the determination of the boundedness of the state variable relies on the unit step function $U(t)$, as defined in equations (3). The *I-V* relationship is dependent on $x(t)$, and here, the coefficients collected from wavelet transform are considered as state variables in the image compression process, which provides a significant change in the device resistance [8]. The range of $x(t)$ is defined between 0 and 1, which directly influences the device conductivity which is again associated with the image quality. Further, equations (4) and (5) describe the window function for the discussed model [8]. Here, one additional boundary condition is imposed i. e., $x_p + x_n = 1$ over the window function which further provides better controllability over the analytical model. The analytical parameter values and their physical interpretation are also shown in Table 3.1.

TABLE 3.1
PHYSICAL INTERPRETATION AND VALUE OF PARAMETERS FOR ANALYTICAL MODELING

| Parameters | Numerical values | Physical interpretation |
|---|---|---|
| $a_1$ | 7 × 10−4 | Experimental fitting parameters |
| $a_2$ | 3.9 × 10−5 | Experimental fitting parameters |
| $b_1$ | 3.8 | Conductivity slope controlling parameter |
| $b_2$ | 1.5 | Conductivity slope controlling parameter |
| $\alpha_p$, $\alpha_n$ | 1.2 | Control parameters for the rate of change of state |

| | | |
|---|---|---|
| | | variable |
| $x_p$ | 0.7 | Constant for determining the bounded- ness of state variable |
| $A_p$, $A_n$ | 0.0021 | Magnitude of exponentials |
| $x_n$ | 0.3 | Constant for determining the bounded-ness of state variable |

The proposed analytical model [8] has better accuracy than the previously reported model [39]. The proposed model has a maximum error deviation (MED) of 16.66%, while the previous model has an MED of 36.8%. The proposed model was validated by comparing its results to the experimental results of a single $Y_2O_3$ MCA based device [8]. The electrical performance of $Y_2O_3$ MCA was fabricated and characterized by researchers for the purpose of image processing. Owing to practically minimal leakage current, which offers long-endurance, fast write time, and compact cell size, a two-terminal MCA has demonstrated superior storage and information processing capabilities, making it a potential building block for in-memory computing. This supports parallel computing and provides energy-efficient computing thereby combining processing and storage by using the same physical elements of the MCA based system.

### 3.2.2. MCA Fabrication

MCA brings a new opportunity for the advancement of computer technology as well as the development of image processing, which includes importing the image via image acquisition tools, analysing, and manipulating the image. Generally, software or hardware techniques can be used to implement image compression methods [15]. Software techniques generally rely on image compression approaches by employing the forward transform phase which consists of a vector-matrix multiplication and matrix transpose. Due to large computational costs and unrealistic memory requirements, such procedures are not appropriate for real-time applications [15, 16]. Furthermore, the memristor based synaptic devices with inherent learning and memory functions are more suitable for image compression methods. These synaptic devices are realized through a metal-insulator semiconductor

(MIS) structure that offers nonlinear transmission characteristics, long-term plasticity, and short-term plasticity which are beneficial for the transmission and storage of compressed images [6]. In today's world of big data analysis and emerging IoT applications across various domains of security, healthcare [17], large scientific and engineering experiments, and image compression plays a crucial role in efficient storage and fast communication by removing redundant data [5, 32].

Several studies have explored using memristive systems for image processing, highlighting the need for high storage capacity and fast access [13]. One of these studies proposed a memristive system that employs three distinct MCA, with one for computation, another for storing coefficients of row-column transformation, and the last for preserving compressed data of the original image for image decomposition and storage [33, 34]. Zhu *et al* [10] employed memristance, the internal resistance of the device, as a parameter for adjusting and mitigating the noise effect (fogging) in the image being used. However, Zhu *et al* [10, 35] did not establish a direct relationship between memristance ($M$) and the adjusting parameters, leading to limitations in their reported model's effectiveness. In contrast, our presented model utilizes conductivity-controlled parameters to directly influence the device current, which in turn affects the image properties. While Zhu *et al* [10] used a filamentary-type memristor (NiO as a resistive switching layer) for digital image processing, the authors employ an interfacial-type memristor ($Y_2O_3$ as a resistive switching layer) for analog image processing. In our model, the device conductance varies according to pixel values, allowing for more precise control over image processing. Bettayeb *et al* [36] utilized filtered images (processed with random spray retinex (RSR)) to implement in-memory computation tasks for image enhancement using a 65 nm CMOS technology and SPICE circuit simulator.

However, filtered images inherently reduce the noise margin, resulting in reduced accuracy compared to experimental data. In proposed work, one performs image compression and enhancement processes using a pure memristor model without any filter implementation, showcasing the fundamental capabilities of memristor-based image enhancement and computation tasks. Bettayeb *et al* [36] introduced the retinex algorithm for spatial colour processing in a probabilistic manner, which occasionally yields averaged local intensity minima, reducing the error rate. On the other hand, authors choose not to employ spatial colour mapping that prevent the occurrence of averaged local intensity minima. Instead, we directly consider the original pixel values during the processing stage.

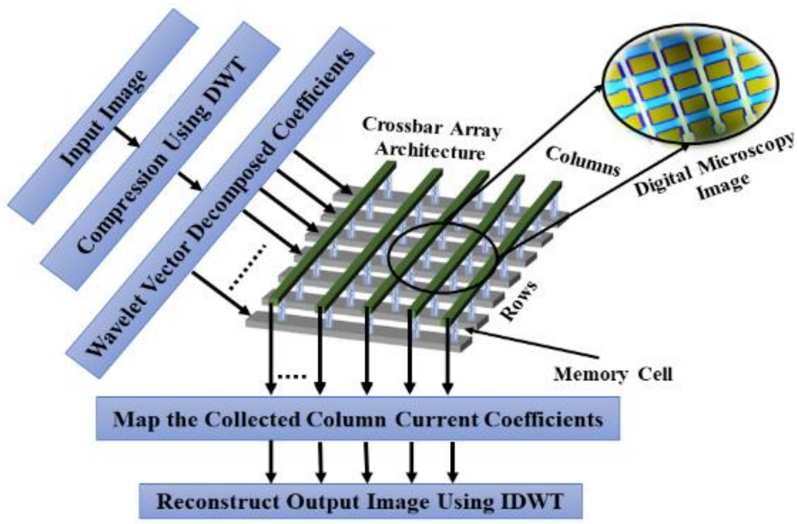


Figure 3.2: Image pixel values in form of vector stored in MCA based device, and digital microscope image of a section of the fabricated

Analog in-memory computing is enabled by the MCA design, which saves electrical power and storage space as compared to the standard digital methods [5]. The MCA not only offers a more convenient storage format for binary images but also offers a new greyscale storage method [40]. In this work, mentioned values of various variable parameters are used to simulate the MCA based model for image compression. Moreover, in this proposed work, the biological image computation and assessment are comprehensively analysed by utilizing MCA based model with the more efficient two-dimensional wavelet transform. Further, it should be noted that the variations in the

MCA non-linearity can be studied by changing the values of the conductive slope controlling parameter as described in the analytical model. The effect of the device's non-linearities on the quality of reconstructed output images. This model can be directly mapped into a crossbar in hardware where the wave decomposition vector is obtained after decomposition as inputs, along the rows of the MCA, and the output coefficients for reconstruction are obtained along the columns.

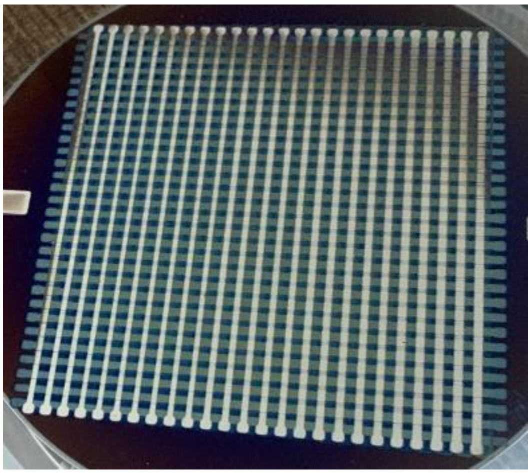

Figure 3.3: Digital camera image of fabricated memristive crossbar array of (30×25) on a 3-inch Si substrate (top view).

An analytical model for MCA can also be used in artificial neural networks and intelligent information processing [40]. As a result, an analytical MCA based model for image compression can provide significant benefits in the domain of in-computing and image processing. The MCA size of (30×25) which is realized by utilizing the DIBS system is shown in Fig. 3.3. A cleaned 3-inch silicon (100) wafer is used as a substrate for the fabrication of (30×25) crossbar array. After the proper cleaning process [14], a layer of polycrystalline $Y_2O_3$ is deposited with the help of the DIBS system [14] to function as an insulating layer. During insulating layer deposition, a pure $Ar^+$ environment with substrate temperature is maintained at 100 °C [14]. In the next step, Ga-doped ZnO (GZO) layer is deposited in the presence of pure $Ar^+$ to function as a bottom electrode (BE) [6]. The developed BE is 100 nm thick and is very conducting ($5.4\times10^{-4}$ Ω.cm) in nature. The developed layer of GZO is then patterned via the shadow mask method. The contact developed between the GZO (Ga-doped ZnO) bottom electrode and Si is a Schottky contact. This is primarily due to the difference in work functions between GZO and Si, which creates a potential barrier at the interface, leading to rectifying behavior. The presence of this Schottky barrier is crucial for certain device applications, as it influences charge transport properties, leakage currents, and overall device performance [6]. The minimum feature size is fixed at 1000 µm. Next, a layer of 50 nm amorphous $Y_2O_3$ [6] is grown which acts as a switching layer (SL) and pattern via shadow mask. A layer of amorphous $Y_2O_3$ is formed under the conditions of 300 °C substrate temperature, and a 2:3 Ar to $O_2$ ratio in the assist ion source of DIBS. At the final step of fabrication, a layer of Al is deposited over $Y_2O_3$ SL. This layer is of 70 nm thickness and is deposited using a direct-current magnetron sputtering system and acts as a top electrode (TE) of the crossbar array and has a line width of 300 to 600 µm. To characterize the fabricated crossbar array design, a semiconductor parameter analyzer (SPA-4200A) is used to perform electrical measurements of the crossbar array. After the fabrication and performance evaluation, it is essential to analytically investigate the outcome of a device or system to understand the underlying physics. The analytical model helps one to analyse the possible factors triggering any deviation in the response of the fabricated electronic device from its ideal behaviour. In the following section, a detailed analytical model has been discussed which helps to understand the device’s behaviour. The discussed analytical model exhibits a promising way to simulate the MCA for image processing applications. The step-by-step fabrication methodology, including substrate preparation, deposition of the switching layer, and electrode patterning, is thoroughly described [14]. To ensure clarity, the process begins with cleaning a 3 inch low-resistivity, n-type Si (100) substrate using trichloroethylene, acetone, and isopropyl alcohol under sonication. The substrate is then subjected to $Ar^+$ plasma etching to remove the native $SiO_2$ layer, followed by the deposition of a 150 nm polycrystalline $Y_2O_3$ insulating layer. A 100 nm Ga-doped ZnO (GZO) bottom electrode (BE) is subsequently deposited and patterned using a metal shadow mask. A 50 nm amorphous $Y_2O_3$ resistive switching layer (SL) is then deposited, maintaining precise process conditions. Finally, a 70 nm Al top electrode (TE) is deposited using DC magnetron sputtering, with the TE line width varied between 600 μm and 300 μm to study its impact on device characteristics [14]. Regarding dimensional specifications, the thesis explicitly provides details such as, spacing between two bottom electrodes is 300 μm, width of the electrodes is 1000 μm (for BE) and varied from 600 to 300 μm (for TE), pixel size of the $Y_2O_3$ switching layer is corresponding to the electrode dimensions (normalized between 0 to 1), and spacing between two top electrodes is 300 μm.

### 3.2.3. Decomposition Techniques

Additionally, Dong *et al* [34] proposed an adaptive memristive pulse coupled neural network (PCNN) for image processing, while Mannion *et al* illustrated a way to use memristive-based potential divider to perform edge detection in images. Our literature review has identified several limitations and drawbacks in existing techniques for computed tomography (CT) scan, magnetic resonance imaging (MRI), and other medical imaging modalities. These limitations include limited contrast, speckle noise, algorithm computational complexity, lack of standardization in evaluation [37], and the need for improved texture and image enhancement [38]. The research gaps include limited focus, lack of interdisciplinary approach, limited discussion on energy, power, and area consumption that directly affect cost of the device [13].

In this work, the researchers fabricated and characterized the electrical performance of $Y_2O_3$ MCA for the application of image processing. As our research group leading in the field of $Y_2O_3$-based memristors, it is important to note that $Y_2O_3$ has several advantages over other transition metal oxide materials such as $TiO_2$, $HfO_2$, $SiO_2$, ZnO, and $Ta_2O_5$ [6]. $Y_2O_3$ is a more suitable material candidate for MCA structures due to its physical properties, such as high dielectric constant, low lattice mismatch, transparency, and Schottky behaviour with aluminium [6]. The electrical characterizations obtained through experimentation were validated by utilizing an analytical model [8]. This analytical model, which was specifically designed for computational work, was further employed for performing image compression. The proposed MCA-based model was applied to a greyscale input image of resolution (512×512), and decomposition techniques were applied to it. Image compression was performed with varied DL, and the decomposed image was imposed through the MCA-based model at source. An inverse decomposition operation was performed on the processed image for reconstruction purposes at the receiver's end.

The discussed MCA based model assists in the storage of a compressed image with less power consumption in a small area as compared to conventional technology based on the application specified integrated circuit (ASIC) for storing biomedical images [4, 5]. The decomposed image coefficients are stored in the MCA by mapping the coefficient values to appropriate voltage levels. As shown in Fig. 3.2, the mapped voltages are fed to the crossbar array along the rows. For reconstruction of the images, the column currents are collected, and then these values are used to perform the inverse wavelet transform operation. Fig. 3.2 shows the storage mechanism and a digital microscope image of the fabricated MCA that indicates the deposited material layers are perfectly aligned with each other to form cross-point structures. The most significant benefit of the suggested analytical model given here is that it offers designers and engineers useful feedback when designing MCA based systems for a variety of real-time applications. The designer can use this model to check the accuracy and efficiency of an MCA based system and would be able to comprehend the behaviour and interactions of the MCA based system better with the aid of the given analytical modelling. Moreover, the discussed analytical model will be more equipped to deal with the overall system's complexity. Owing to the immense popularity of multimedia, the demand for the powerful representation of various types of data is huge. There is a pressing need to minimize the amount of data to be transmitted and protected from unauthorized access. Images are extensively used in multimedia applications, therefore, a good compression and encryption scheme for images has substantial applications.

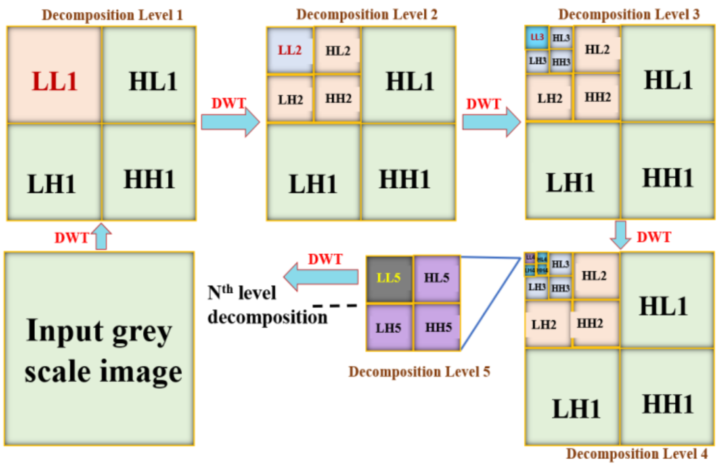


Figure 3.4: Stepwise decomposition process of an image.

It is known that the image decomposition technique gives rise to wave decomposition vectors in a single array that can be used as input signals in the MCA for image compression and encryption [34]. Table 3.2 shows the in-depth comparison of our work with other existing decomposition techniques. It can be perceived that the application of MCA-based model is more compatible with the DWT image decomposition technique compared to DCT and signal vector decomposition (SVD) [41-46]. DWT provides substantial improvement in picture quality at high compression ratio due to better energy compaction properties with different locations and scale of wavelet transform having lesser computational complexity [5, 46], and these special properties are not present in SVD and DCT [41].

| TABLE 3.2<br>COMPARISON OF EXISTING DECOMPOSITION TECHNOLOGIES WITH THE PROPOSED WORK | | | |
|---|---|---|---|
| **Technology** | **Images** | **PSNR (dB)** | **SSIM** |
| DCT | Magnetic resonance imaging (MRI) | 18.9153 | 0.6718 |
| | Computed tomography (CT) scan | 12.3299 | 0.6172 |
| SVD | MRI | 17.5627 | 0.6129 |
| | CT Scan | 14.4363 | 0.4396 |
| Our Work | MRI (without brightness) | 19.1451 | 0.6774 |
| | MRI (with brightness) | 22.4299 | 0.7441 |
| | CT Scan (without brightness) | 12.3299 | 0.6674 |
| | CT Scan (with brightness) | 24.97 | 0.8542 |

In the process of decomposition, wavelet analysis has become a destination for many applications due to the usage of various basis functions in the form of distinct mother wavelets [42, 43, 51]. It is well-known that a wavelet is a zero-mean, and quickly fading wave-like oscillation [51]. Unlike sinusoids, which have infinite duration, wavelets have a limited duration. Further, wavelets are available in a variety of sizes, and forms and wavelet transform are used to suppress noise, which is out of the frequency band of the input signal [42, 52]. There are various types of wavelets, among which the Haar wavelet is the most straightforward technique, mostly used in image processing [52]. In this work, 512×512 greyscale MRI and CT scan images [53, 54] are used to perform the comparative analysis using seven different wavelets, such as Haar, Debauchies, Symlet, Coiflets, Biorthogonal, Reverse biorthogonal, and Fejer Korovokin. Each category of mother wavelet has several sub-wavelets [55]. A series of all the wavelets which have been used in this work are represented as Haar, db2, sym4, coif2, bior1.5, rbio3.1, and fk14, respectively.

In 2D-DWT, the image is applied to high-pass and low-pass filters, according to the different DL required. To compress an image using 2D-DWT, down sampling is performed to obtain approximation coefficients of the image with only low frequency components. The low-pass filter (LPF) calculates the averages of the coefficients causing a smoothing effect on the image, while the high-pass filter (HPF) produces the details coefficients of an image. Both LPF and HPF will give separate frequency sub-bands in each DL, for which approximation coefficients of previous levels are considered as an input for the next DL. In every step of decomposition, four sub-bands will be received as the output, as mentioned earlier, and shown in Fig. 4. The sub-band LL will provide an approximation coefficient with low frequency components having the maximum amount of information, LH sub-band extracts the horizontal features, HL sub-band extracts vertical details of an input image and HH sub-band provides the diagonal features [10]. It is worth noting that the number of times the decomposition is performed will give the number of transformation levels which will reduce the complexity of computation [4, 5].

The obtained coefficients, after performing image decomposition, as shown in Fig. 3.2, are used as wave decomposition vectors and input to the MCA. After applying different DL, the wavelet coefficients are stored in wave decomposition vectors ($C_1$, $C_2$, $C_3$…, $C_n$) as state variables in the MCA device. These coefficients have the same normalized pixel value of an image as input voltages in the crossbar array. Retrieving the result involves summing up currents from each column, following Kirchhoff's current law, and using sensors to obtain corresponding voltages. Our research group holds a leading position in $Y_2O_3$-based memristor research, offering numerous advantages.

## 3.3. Result and Discussion

### 3.3.1. Characterization of MCA

For the structural and materials characterizations of the fabricated MCA, optical microscopy, and field emission scanning electron microscopy (FESEM) are used which help to visualize the perfect crosspoint structure and amorphous nature of the deposited thin film which acts as switching layer. The amorphous $Y_2O_3$ is a promising candidate to realize highly stable MCA, as reported previously [6, 14].

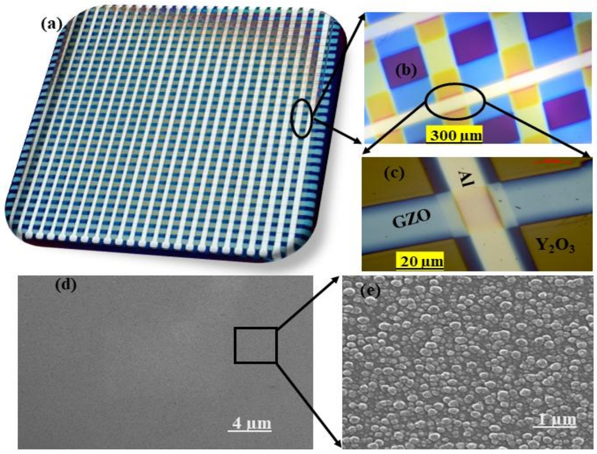


Figure 3.5: (a) A digital image of the fabricated MCA (top view): optical microscopy images in (b) normal view and (c) magnified view; (d-e) FESEM image of amorphous $Y_2O_3$ switching layer at different scales.

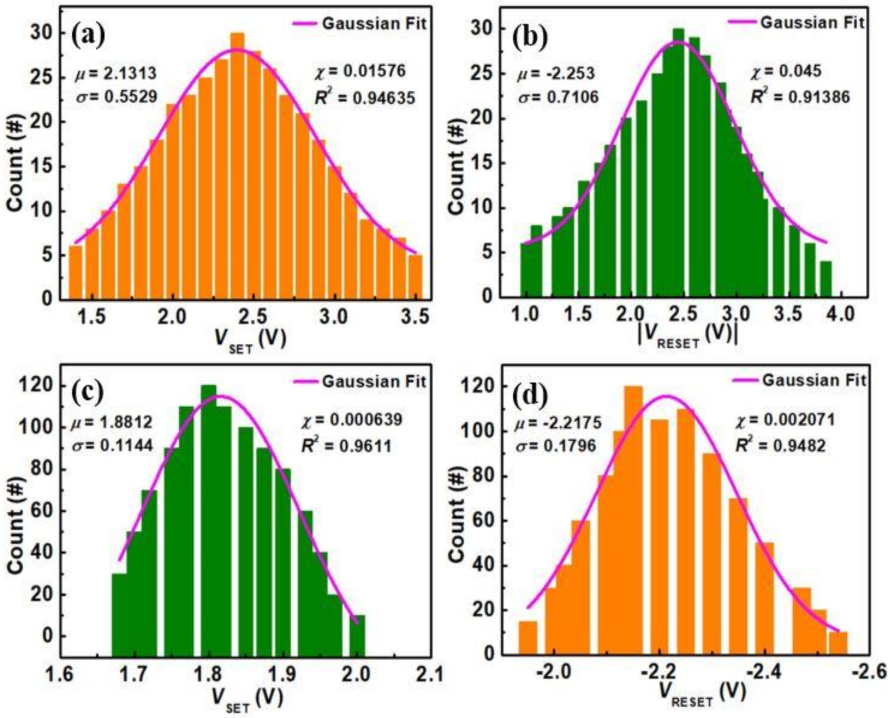


Figure 3.6: D2D statistical distribution of (a) VSET and (b) VRESET for 30 devices in the MCA fitted with Gaussian curves; C2C statistical distribution for 120 cycles of (c) VSET and (d) VRESET in a single memristor in the MCA with Gaussian fitting.

Fig. 3.5(a) shows the fabricated crossbar array while Fig. 3.5(b) and 3.5(c) show the optical microscopy images at the different scales. As seen from Fig. 3.5(c), the fabricated crossbar array has a perfect crosspoint structure, which is desirable in an MCA to avoid any electrical shortage in memory cells via top and bottom electrodes. The FESEM results reveal the $Y_2O_3$ which confirms the amorphous nature of the deposited thin film, as shown in Fig. 3.5(d-e). To study the resistive switching electrical characteristics of the developed MCA based device, a triangular waveform with a peak-to-peak voltage of ±3 V is applied as an input voltage to the MCA based system. The switching characteristics of the fabricated device and analytical model are depicted in Fig. 3.7(a). The perfectly aligned layers forming a crosspoint structure in the array the purple-colored layer corresponds to the $Y_2O_3$.

The pinched hysteresis loop observed is indicative of the MCA-based system's characteristics [36]. The analytical model shows an extremely well correlation with the experimentally obtained result. The analytical data shows 98.7% $R^2$ fitting with the corresponding experimental data of the fabricated MCA. Morphological analysis of the resistive switching layer of one of the important performance parameters of a MCA based device is the average value of the current ratio ($I_{\text{Ratio}}$) obtained between the high resistance state (HRS) and low resistance state (LRS). In Fig. 3.6 (b), the performance of the device remains unaltered up to ~$7.5 \times 10^5$ switching cycles, after which a reduction to ~30 is observed in the value of $I_{\text{Ratio}}$. A high average value of $I_{\text{Ratio}} >$ 200 defines that the MCA-based devices present in the crossbar array are reliable and stable. In case of retention analysis, the HRS and LRS are separated from each other up to $1.5 \times 10^5$ s with $I_{\text{Ratio}} > 200$. After an interval of $1.5 \times 10^5$ s, the value of $I_{\text{Ratio}}$ is decreased to ~30 as shown in Fig. 3.6(c). It should be noted that the high memory window between HRS and LRS is beneficial to achieve high endurance and retention properties. The statistical analysis matching with the Gaussian fitting curves is seen in the statistical distribution of $V_{\text{SET}}$ for both devices-to-device (D2D) and cycle-to-cycle (C2C), as shown in Fig. 3.6.

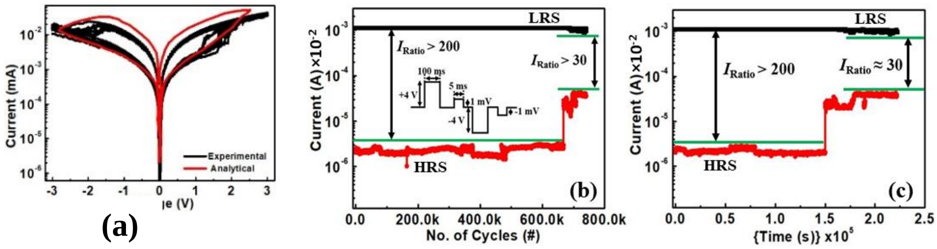


Figure 3.7: (a) Semi-logarithmic resistive switching characteristic of the fabricated crossbar array structure fitted with validated data; (b) endurance measurement up to 7.5×10$^5$ cycles and degradation in the current ratio is found at nearly 7.5×10$^5$ cycles, and the inset shows the applied input programming voltage pulse; (c) retention measurement of the fabricated device up to 2.25×10$^5$ s and degradation is found at nearly 1.5×10$^5$ s.

The goodness-of-fit ($\chi^2$) and the error coefficient ($R^2$) have estimated values of 0.01576 and 0.94635, respectively, for $V_{SET}$ and 0.045 and 0.91386, respectively, for $V_{RESET}$ for D2D variability, as shown in Fig. 3.7 (a) and (b). The $\chi^2$ and $R^2$ have estimated values of 0.000639 and 0.9611, respectively, for $V_{SET}$ and 0.002071 and 0.9482, respectively, for $V_{RESET}$, respectively, for $V_{SET}$, as shown in Fig. 3.7 (c) and (d).

### 3.3.2. Proposed Work Formulation

For the image quality assessment, various parameters such as PSNR, SSIM, and MSE are used. These assessment parameters are helpful to quantify the reduction in image quality due to compression done by utilizing as discussed MCA based model [8]. These assessment parameters can be computed, as shown by equations (6-10):

$$Compression\ Ratio(CR) = \left[\frac{\substack{Non-zero\ element \\ in\ input\ Image}}{\substack{Non-zero\ element \\ in\ output\ Image}}\right] \quad (6)$$

$$Data\ compression\ (\%) = \left[\frac{N-N_1}{N}\right] \times 100 \quad (7)$$

where $N$ and $N_1$ show the size of the uncompressed image and compressed image at different DL.

$$PSNR(I,C) = 10\ log10\left[\frac{M\times N}{MSE(I,C)}\right] \quad (8)$$

$$MSE(I,C) = \left[\frac{1}{M\times N}\right]\sum_{i=0}^{M}\ \sum_{j=0}^{N}\left(I_{ij} - C_{ij}\right)^2 \quad (9)$$

where, $M \times N$ is the resolution of an uncompressed image, and $i, j$ is coordinates in 2D image.

$$SSIM(I, C) = l\ (I, C)\ c\ (I, C)\ s\ (I, C) \tag{10}$$

where, '$l$', '$c$', and '$s$' stands for luminesces, contrast, and structural similarity, respectively.

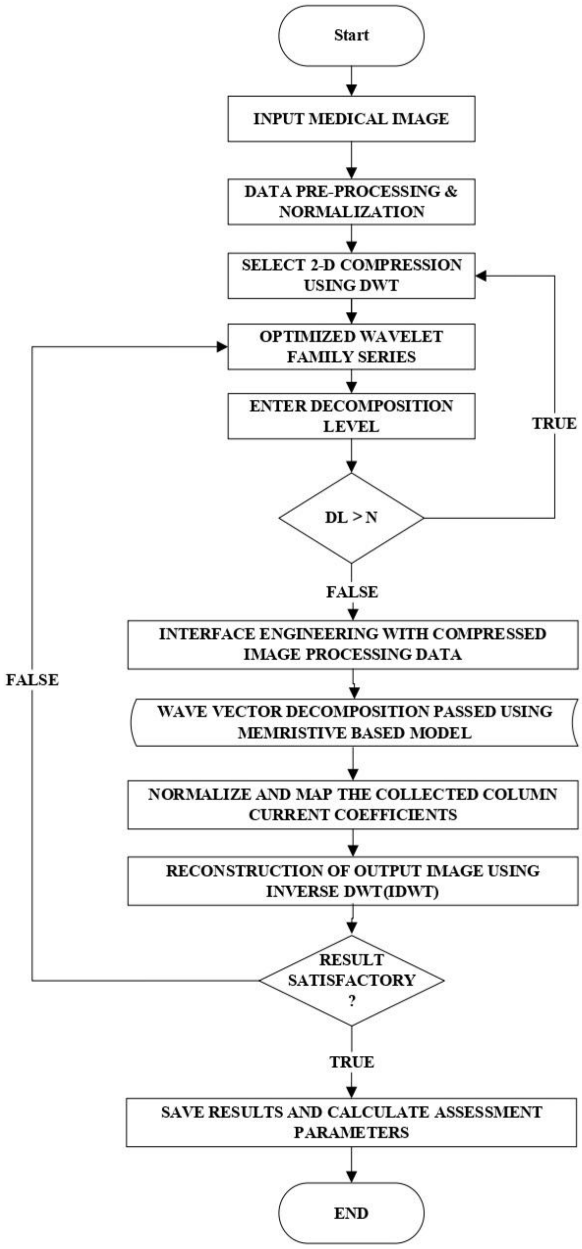


Fig. 3.8: Simulation flow chart.

The compression ratio (CR) is defined as the number of non-zero elements of the original image over the non-zero elements of the compressed image [46], as mentioned in equation (6). The term compression is explained mathematically in equation (7). Data compression can be calculated by taking the ratio of the difference in the sizes of the input and reconstructed output image to the input image [56, 57]. The quality of the reconstructed output image (C) can be directly obtained from the value of PSNR [58] and the PSNR is given by the ratio between the peak or maximum intensity power of an image to the noise encountered in the image as given in equation (8). The PSNR value approaches infinity as MSE approaches zero; this shows that a higher PSNR value provides a better image quality [58]. MSE values can be evaluated by using equation (9). The SSIM is calculated by modelling image distortions as a combination of three factors that are the loss of correlation, luminance distortion, and contrast distortion [57] and is given by equation (10). The simulation part of the work, as described earlier, is shown via a flow chart in Fig. 8 to see how MCA-based model is incorporated for image compression.

### 3.3.3. Effect of Brightness/Quality on the Reconstructed Image via Different Mother Wavelets

The DWT offers significant picture quality improvement at high compression ratios due to its superior energy compaction properties, involving wavelet transform at various locations and scales with lower computational complexity [46]. Images are tainted by noise during acquisition, compression, and transmission, causing distortion and loss of information present in the image [59-61]. There are many sources of noise in digital images mainly due to environmental conditions of the imaging sensor, electronic transmission of image data, and interference in the transmission channel [59]. Image compression can be achieved by removing these redundancies in an image wherever possible. According to DWT, the most important information in the image is present in high amplitudes, while less important information is associated with very low amplitude of signal [61].

In order to discard the low-amplitude information, the thresholding method is used which compresses the data. The wavelet transforms provide a high compression ratio along with a good quality of reconstruction [62]. It can be used for easy denoising of an image. The denoise image is obtained by considering only a limited number of higher coefficients present in the DWT spectrum and then performing the inverse transform of the DWT spectrum [60, 61]. MATLAB simulations are performed to analyse the effect of compression on the MRI and CT scan images. These images are considered since they are one of the most essential parameters for medical diagnosis. CT scan has been deployed as an effective tool for diagnosis of COVID-19, and MRI has been effective for diagnosis of Alzheimer's disease [61]. In this study, a specific series of different mother wavelets compatible with the discussed MCA-based model are employed to achieve optimized results for image compression.

The discussed analytical MCA based model is used to compress and store both MRI and CT scan images [8]. It is widely known that the different wavelets have different levels of compatibility with images; thus, any mother wavelet cannot be configured as the best for a particular image since its compatibility is different for different applications and models [61].

Among different mother wavelets, Haar and biorthogonal wavelets exhibit a better quality of reconstructed output image as compared to other mother wavelets which are depicted in Fig. 9. The technical reason behind their best performance compared with other wavelets is, the Haar wavelet [62-64] having basis function which is very simple and easily compatible with the nature of the image and biorthogonal [64] basis function makes resemblance with the decomposed image that provides better quality of reconstructed output image. The highest quality of reconstructed output images of MRI and CT scan is 18.9938 dB, and 12.2567 dB using Haar mother wavelet, respectively. The second-best quality is obtained by using biorthogonal mother wavelet i.e., 11.5654 and 19.0168 dB for CT scan and MRI images, respectively. For increasing the brightness, the intensity of each pixel is increased by a specific value which affects the quality of the output image and optimizes the performance of the image compression system. The increment in the quality of the output image by the insertion of some constant value resembles the effect of an amplifier towards the end of a signal receiver. To graphically explore this effect, as shown in the inset of Fig. 3.9, on the addition of a constant value of ‘65’ to the CT scan output image and a multiplication factor of ‘2’ to the MRI output image the percentage of quality of the reconstructed image further enhances to produce optimized results. Also, it can be noted that the effect of brightness is most prominent when symlet mother wavelet is used to decompose CT scan and Fejer Korovokin mother wavelet is used to decompose MRI image, as presented in Table 3.3. The size of CT scan image is 228 Kilo Bytes (KB), and the size of MRI image is 73.3 KB. In vector matrix multiplication, the higher number of samples in matrix multiplication of a larger image size affects the quality of the output image at a higher scale. In the case of MRI image, less amount of data is stored in the wave decomposition vector as compared to that for the CT scan image because of the smaller image size, and this results in a smaller change in the quality of the output image for MRI as compared to that for CT scan. Therefore, the quality of the MRI images is better than that of the CT scan images, which can be perceived by the values of assessment parameters in Table 3.4 and 3.5 for MRI images, and Table 3.6 and 3.7 for CT scan images, respectively. The effect of image size on the degradation in the quality of output image is shown in Table 3.4, and Table 3.5 for MRI images and Table 3.6, and Table 3.7 for CT scan images. Table 3.4 shows the degradation in the quality of the output image in terms of PSNR, SSIM, and MSE with the increment in DL of MRI image using Haar mother wavelet. The similarity index between input and output images of MRI reduces since SSIM is directly affected by the structural phase distortion of an image.

However, MSE increases because it has an inverse relation with the quality of the reconstructed output image, which indicates that the value of PSNR decreases for higher DL. At each higher value of DL, an increment in the error is introduced that can be noted by the value of MSE.

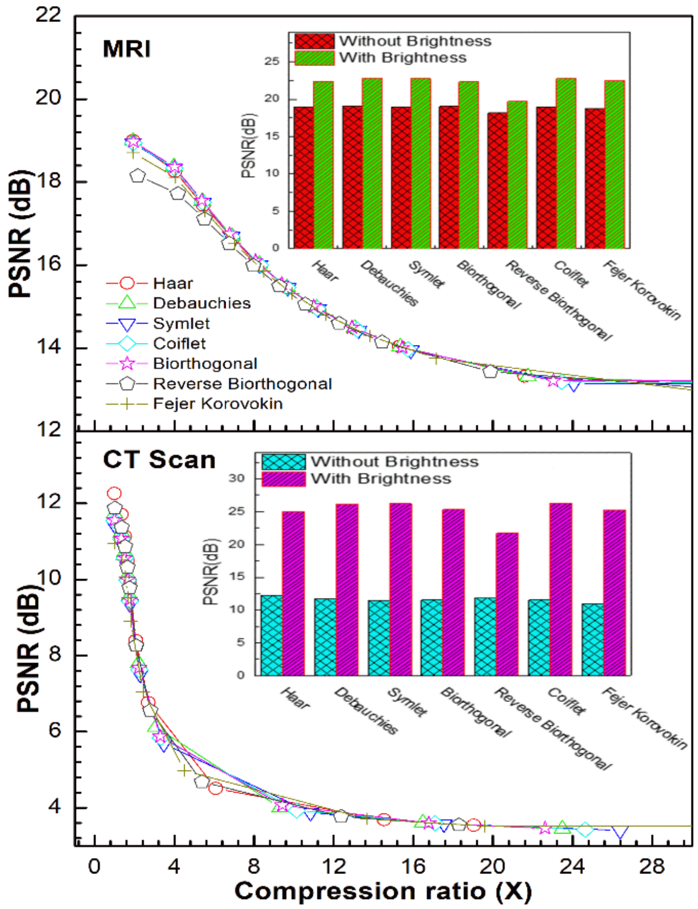


Figure 3.9: The variation of PSNR (dB) of reconstructed image with a change in compression ratios for seven different mother wavelets. The inset shows the effect of brightness on reconstructed output image for different wavelets.

The same concept is applicable for MRI reconstructed output images using biorthogonal mother wavelet for different DL, as shown in Table 3.5. By comparing Table 3.4 and 3.5, it can be said that for the biorthogonal wavelet, MCA based model gives a better result as compared to the Haar wavelet. Moreover, the effect of brightness on PSNR and MSE at 1st DL using Haar gives rise to better results as compared to that for the biorthogonal wavelet on the reconstructed output MRI images.

TABLE 3.3

PERFORMANCE OF DIFFERENT MOTHER WAVELETS REPRESENTED BY INCREASED PERCENTAGE OF PSNR WITH BRIGHTNESS EFFECT

| Wavelets | Increment in PSNR (%) | |
|---|---|---|
| | CT scan | MRI |
| Haar | 103.72 | 18.59 |
| Daubechies | 123.57 | 19.94 |
| Symlet | 147.31 | 20.09 |
| Biorthogonal | 119.28 | 17.62 |
| Reverse biorthogonal | 83.23 | 8.29 |
| Coiflets | 128.15 | 19.89 |
| Fejer Korovkin | 130.46 | 20.71 |

TABLE 3.4

ASSESSMENT PARAMETERS OF MRI IMAGE USING HAAR WAVELET FOR DIFFERENT DL

| DL | Without brightness | | | With brightness | | |
|---|---|---|---|---|---|---|
| | PSNR (dB) | SSIM | MSE | PSNR (dB) | SSIM | MSE |
| 1st | 18.9938 | 0.6718 | 835.1 | 22.4299 | 0.7441 | 371.6 |
| 2nd | 18.0155 | 0.6442 | 1026.9 | 20.6528 | 0.7004 | 559.4 |
| 3rd | 16.7806 | 0.6121 | 1364.6 | 18.5505 | 0.6441 | 907.8 |
| 4th | 15.6231 | 0.5941 | 1781.4 | 16.7549 | 0.6129 | 1372.8 |
| 5th | 14.5734 | 0.5943 | 2268.5 | 15.4806 | 0.6018 | 1840.9 |

TABLE 3.5

ASSESSMENT PARAMETERS OF MRI IMAGE USING BIORTHOGONAL WAVELET FOR DIFFERENT DL

| DL | Without brightness | | | With brightness | | |
|---|---|---|---|---|---|---|
| | PSNR (dB) | SSIM | MSE | PSNR (dB) | SSIM | MSE |
| 1st | 19.0168 | 0.6743 | 815.4614 | 22.3683 | 0.7454 | 376.9225 |
| 2nd | 17.9389 | 0.6456 | 1045.2 | 18.5247 | 0.6379 | 913.3008 |
| 3rd | 16.7622 | 0.6099 | 1370.4 | 16.4737 | 0.5992 | 1464.6 |
| 4th | 15.3239 | 0.5887 | 1908.5 | 15.2639 | 0.5925 | 1935 |
| 5th | 14.5134 | 0.5887 | 2300.1 | 13.7571 | 0.5631 | 2343.16 |

TABLE 3.6

ASSESSMENT PARAMETERS OF CT SCAN IMAGE USING HAAR WAVELET FOR DIFFERENT DL

| DL | Without brightness | | | With brightness | | |
|---|---|---|---|---|---|---|
| | PSNR (dB) | SSIM | MSE | PSNR (dB) | SSIM | MSE |
| 1st | 12.2567 | 0.6386 | 3867.3 | 24.97 | 0.8542 | 209.1409 |
| 2nd | 11.6067 | 0.5321 | 4036.7 | 24.61 | 0.7052 | 319.9715 |
| 3rd | 11.4527 | 0.4141 | 4391 | 22.1594 | 0.5422 | 542.3594 |
| 4th | 10.9049 | 0.3564 | 4977.4 | 19.6888 | 0.4617 | 906.6293 |
| 5th | 10.7378 | 0.3378 | 6057.5 | 17.3748 | 0.4237 | 1573.9 |

TABLE 3.7

ASSESSMENT PARAMETERS OF CT SCAN USING BIORTHOGONAL WAVELET FOR DIFFERENT DL

| DL | Without brightness | | | With brightness | | |
|---|---|---|---|---|---|---|
| | PSNR (dB) | SSIM | MSE | PSNR (dB) | SSIM | MSE |
| 1st | 11.5654 | 0.593 | 4534.6 | 25.3617 | 0.8088 | 189.196 |
| 2nd | 11.1296 | 0.4636 | 5013.3 | 23.1343 | 0.6418 | 315.9768 |
| 3rd | 10.6866 | 0.3496 | 5551.7 | 20.6036 | 0.4797 | 565.8812 |

| | | | | | | |
|---|---|---|---|---|---|---|
| $4^{th}$ | 10.6784 | 0.3124 | 5562.2 | 18.4412 | 0.4115 | 931.02 |
| $5^{th}$ | 9.9405 | 0.3033 | 6592.2 | 15.9163 | 0.3874 | 1673.12 |

From Table 3.6 and 3.7, it can be said that Haar mother wavelet-based CT scan output images produce better results as compared to those for biorthogonal-based output images. In the case of CT scan images, the effect of brightness on the quality of the reconstructed output image is more by using biorthogonal mother wavelet as compared to the Haar mother wavelet. From the first level to the fifth level of decomposition, using the Haar wavelet without any brightness effect, the percentage degradation in PSNR, SSIM, and percentage increase in MSE is calculated to be 23.27%, 11.53%, and 171.64%, respectively for MRI image and the similar values are 12.39%, 47.10%, and 56.63%, respectively, for CT scan image. Upon the addition of brightness parameter, the percentage degradation in PSNR, SSIM and percentage increase in MSE are improved and the values are 30.98%, 19.12%, and 395.39%, respectively, for MRI images and the similar improved values are 30.41%, 50.39%, and 652.55%, respectively for CT scan image, on an increase of DL from first to the fifth level. On the other hand, using biorthogonal wavelet without any brightness effect, the percentage degradation in PSNR, SSIM, and percentage increase in MSE values are 23.68%, 12.66% and 182.06%, respectively, for MRI images and the similar values are 14.04%, 48.01%, and 45.37%, respectively, for CT scan image, while shifting from first to fifth DL. Upon addition of brightness with increment in DL, the percentage degradation in PSNR, SSIM and the percentage increase in MSE have also exhibited an improvement and these values are 31.76%, 20.51%, and 413.36%, respectively, for MRI images and similar improved values are 37.24%, 52.10%, and 784.33%, respectively, for CT scan image. Here, high data compression of reconstructed output image has been received for different DL by using MCA based model.

### 3.3.4. Impact of compression percentage on varied DL

For the compression of the reconstructed output image, threshold values at different percentages of compression have been utilized. The degradation in the quality of the output images with an increase in DL is shown in Table 3.8. Input image having 512×512 resolution is compressed at the first DL to obtain a 256×256 resolution approximation image. Similarly, for the second DL, the resolution is further compressed to 128×128. This value of compression in quality might be tolerable and can be used for diagnostic purposes. However, for the third, fourth, and fifth DL, the corresponding resolution is 64×64, 32×32, and 16×16, respectively.

TABLE 3.8
BIOMEDICAL IMAGES (MRI AND CT SCAN) WITH DIFFERENT DL

| Images | MRI | | CT scan | |
|---|---|---|---|---|
| Decomposition Levels | Haar Wavelet | Biorthogonal Wavelet | Haar Wavelet | Biorthogonal Wavelet |
| Original input image |  |  |  | 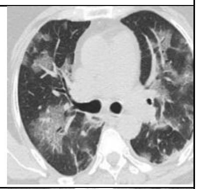 |
| DL1 |  |  | 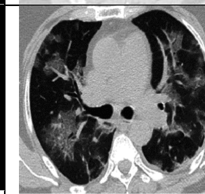 | 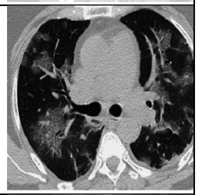 |
| DL2 | 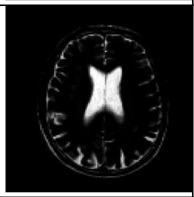 | 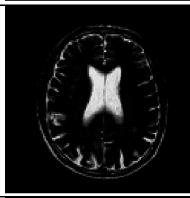 | 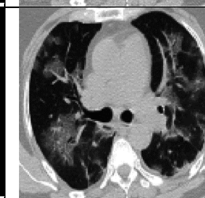 | 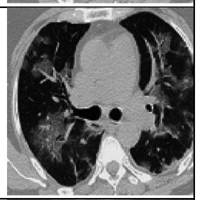 |
| DL3 | 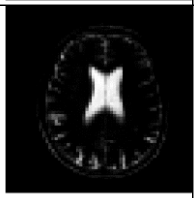 | 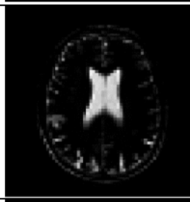 | 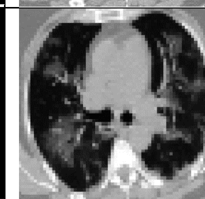 | 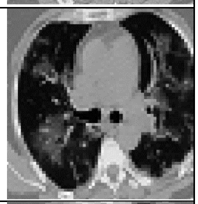 |
| DL4 | 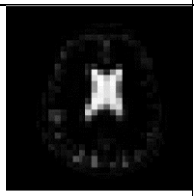 | 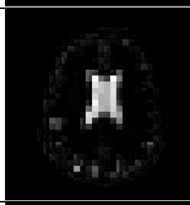 | 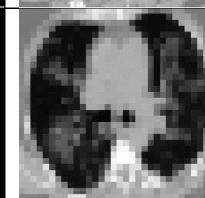 | 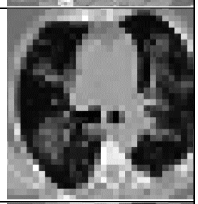 |
| DL5 | 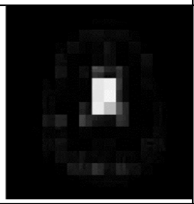 | 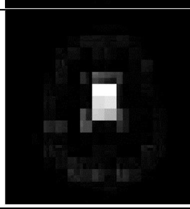 | 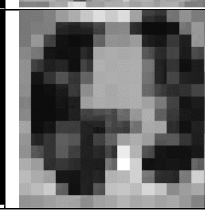 | 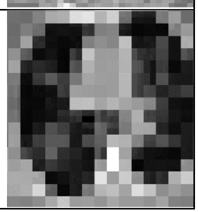 |

The exact number of 16×16 can easily be seen in Table 3.8 for the fifth DL. As evident in Table 3.8, the reconstructed quality of the image is not tolerable as it enhances the noise. The insets of Fig. 3.10 and 3.11 show the variation of PSNR with SSIM for different DL by using Haar and biorthogonal wavelets. The first, second, third, fourth, and fifth DL, are represented by DL1, DL2, DL3, DL4, and DL5, respectively. As one moves to higher DL, the values of PSNR, as well as SSIM, reduce because of degradation in the quality of the image after compression.

The quality of the reconstructed image is reduced substantially during the initial stages of compression, afterwards, the change in the PSNR value is not significant with respect to an increase in CR. For Haar wavelet, the reduction in PSNR for 1% of CR on switching from DL1 to DL2 is 4.73% and 1.51% for the MRI image and CT scan image, respectively. Similarly, from DL2 to DL3 transition using Haar wavelet, the PSNR decreases by 6.82% and 3.02% compression for MRI image and CT scan image, respectively, at 1% CR. For biorthogonal wavelet, the reduction in PSNR values is 5.65% and 3.76% for MRI image and CT scan image, respectively, on switching from DL1 to DL2 at 1% CR. At the same value of CR for biorthogonal wavelet, the PSNR is decreases by 6.47% and 3.98% while moving from DL2 to DL3 for MRI images and CT scan images, respectively. The DL2 is an optimum level of image decomposition for the MCA based algorithm for reconstructed output image as shown in Table 3.8. The above discussion also signifies that the reconstructed image by using MCA based with the help of the Haar mother wavelet compresses the input image by a larger amount as compared to that by the biorthogonal wavelet. Table 3.9 represents the values of data compression with varied DL for both the images. For MRI with first DL, the data compression ratio is 21.01% by using Haar wavelet and 18.82% with biorthogonal wavelet, respectively. For CT scan with first DL, data compression ratio is obtained to be 47.81% by using Haar wavelet and 46.05% with biorthogonal wavelet. As discussed earlier, from Fig. 3.10 and Fig. 3.11, it can be noted that the rate of degradation in the quality of reconstructed output image is higher for CT scan than MRI because of its higher memory size. The larger size of the CT scan image results in the presence of a greater number of samples for computation for the CT scan than for the MRI image and this is responsible for less degradation with enhancement in DL. The quality improvement upon the application of brightness is more prominent in CT scans as compared to MRI images because of wavelet compatibility. In comparison to CMOS-based model for image processing the MCA-based model is observed to significantly improve the values of PSNR and SSIM by 4 and 100 times, respectively, for CT scan image and 1.8 and 1.2 times, respectively, for MRI images. The motivation behind using the MCA-based model is reducing the number of operations, area, and power consumption with faster processing speed [5, 65]. The MCA has several nanometre level downscaling, and CMOS compatible fabrication process and are more favourable for storage and processing of data primarily for applications with limited storage resources. As given in Table 3.9, lesser number of devices and operations is used in MCA-based model as compared to the conventional CMOS-based counterparts as reported by Halawani *et al* [46] and Khalid *et al* [65] also by demonstrating image compression and digital logic operations. Image matrix multiplication using CMOS involves a substantial number of multiplications and additions, including [$m \times n \times c$] multiplications and [$m \times c \times (n$-1)] additions, where m denotes the number of rows in the first matrix, n represents the number of columns in the first matrix or rows in the second matrix, and $c$ signifies the number of columns in the second matrix [46]. On the other hand, when employing a memristor-based approach, the outstanding properties such as pinched hysteresis switching behaviour in its *I-V* characteristics, non-volatile nature, same multiplications and additions can be accomplished through $m \times m$ multiplication and addition.

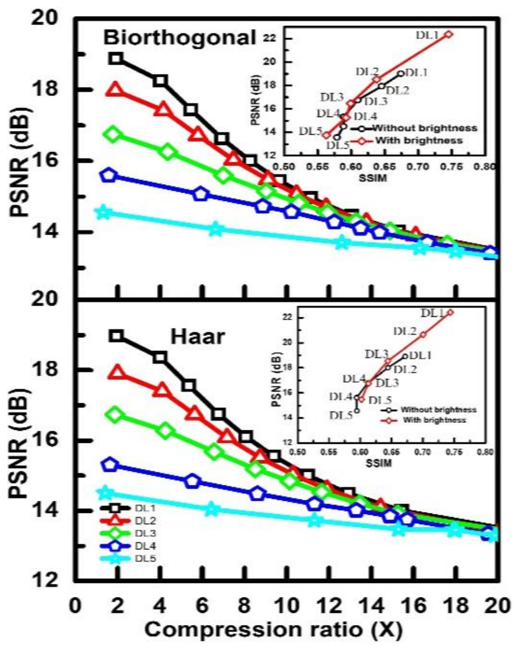


Figure 3.10: Variation in PSNR (dB) of the reconstructed image with a change in CR for the Haar and biorthogonal wavelets with different DL for MRI image. The insets show the effect of brightness on reconstructed output image for varied DL.

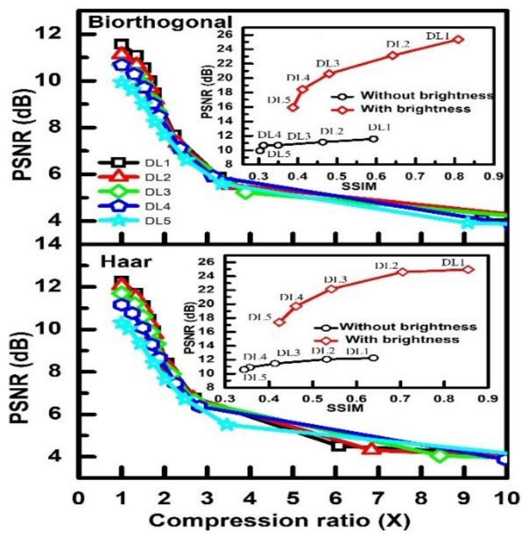


Figure 3.11: Variation in PSNR (dB) of the reconstructed image with a change in CR for the Haar and biorthogonal wavelets with different DL for CT scan image. The insets show the effect of brightness on reconstructed output image for varied DL.

TABLE 3.9
PERCENTAGE OF DATA COMPRESSION WITH DIFFERENT LEVEL OF DECOMPOSITION

| DL using Haar wavelet | Size of decomposed images (KB) | | Data Compression (%) | |
|---|---|---|---|---|
| | MRI | CT scan | MRI | CT scan |
| Input image size | 73.3 | 228 | 73.3 | 228 |
| 1st | 57.9 | 119 | 21.01 | 47.81 |
| 2nd | 37.8 | 69.9 | 48.43 | 69.34 |
| 3rd | 26.7 | 41.4 | 63.57 | 81.84 |
| 4th | 19.6 | 27 | 73.26 | 88.16 |
| 5th | 15.1 | 18.7 | 79.39 | 91.79 |
| DL using biorthogonal wavelet | Size of decomposed image (KB) | | Data compression (%) | |
| | MRI | CT scan | MRI | CT scan |
| Input image size | 73.3 | 228 | 73.3 | 228 |
| 1st | 59.5 | 123 | 18.82 | 46.05 |
| 2nd | 39.1 | 67 | 46.65 | 70.61 |
| 3rd | 28 | 40.3 | 61.81 | 82.32 |
| 4th | 20.6 | 27.1 | 71.89 | 88.11 |
| 5th | 16.2 | 15.8 | 77.89 | 93.07 |

This is because the memristor-based approach can perform multiplication and addition in a single step within the memristor. As a result, utilizing the memristor crossbar architecture for real-time matrix multiplication for image transforms is much more efficient, in computation [46]. Factors such as device properties [14], size and complexity of the processed image [13], proposed image compression and enhancement algorithm, as well as the voltage and current levels used, have an influence on the parameters listed in Table IX.

TABLE 3.10
COMPARISON OF CONVENTIONAL CMOS BASED COMPUTING WITH MCA BASED IN-MEMORY COMPUTATION FOR IMAGE COMPRESSION

| Parameters | CMOS | MCA | Prominent Improvement |
|---|---|---|---|
| Number of Operations [4, 45] | $512^3 + (512^2 \times 511)$ | $512^2$ | 1023 times |
| Area ($\mu m^2$) [4] | 1585446.912 | 41943.04 | 37.8 times |

| | | | |
|---|---|---|---|
| Energy Consumption (pJ) [45] | 1115.4 | 1.484 | 752 times |
| Processing Speed (µs) [4, 45] | 0.15 | 0.06 | 2.5 times |
| Power Consumption (mW) [4] | 7436 | 24.733 | 300 times |

A comparative analysis of compression for (512×512) image is performed using our MCA-based DWT model and conventional CMOS-based models in which values of various parameters in the calculation are taken from [46]. Table 3.10 displays MCA achieving of better performances as compared to the conventional CMOS-based models. Hence, our proposed approach makes the memristor-based solution very attractive for image processing applications. These components-based study is useful for circuitry design to the application of image classification via MCA model-based architecture [46]. As compression has been achieved with minimal losses using MCA based model between input and output images, the processed biomedical images are useful for diagnostic purposes. Moreover, the MCA not only provides a more convenient and cost-effective storage structure for biomedical images, but also presents a novel storage solution for compressed images which is performed by the MCA based system. Our work has shown promising results and can be further implemented on hardware to realize the compatible MCA based system for image processing applications. Furthermore, analysis of image recognition can be done using MCA based models, which would be very much helpful in understanding how a biological brain stores a captured visually.

## 3.4. Conclusion

In this paper, the MCA based model is used for compressing biomedical grayscale images (MRI and CT scan) with 512×512 resolution at different DL. The experimental results prove the stability of MCA in terms of minimized fluctuations in operating voltages. The statistical analysis for D2D and C2C variability is extremely stable and more beneficial in the image computation process. The Gaussian fitting parameters such as goodness-of-fit ($\chi^2$) and the error coefficient ($R^2$) for $V_{SET}$ and $V_{RESET}$ for D2D and C2C variability are also depicted the better correlation with experimental data. The fabricated devices are stable and promising to replace or merge with the CMOS technology.

Among all seven mother wavelets, Haar and biorthogonal wavelets are shown comparatively better results in terms of several assessment parameters such as SSIM, PSNR, and MSE. As we go for the higher DL, the quality and structural similarity index of an image are decreased while MSE is increased which leads to the decrement in image pixel quality. The images imposed on the crossbar array have shown compression while maintaining a very high similarity with the input image. The brightness effect shows an increment in the quality of the output image by 103.72% and 18.59% in CT scan and MRI images, respectively, by using the Haar wavelet. The highest data compression value achieved is 47.81% in the reconstructed output image of CT scan by using Haar wavelet due to its higher memory size compared to MRI image. In the CT scan image, the degradation in quality from first to fifth DL is calculated as 12.39% and 14.06% for the same value of compression ratio using Haar and biorthogonal wavelets, respectively. In the MRI image, the degradation in quality from first DL to fifth DL is calculated as 23.27% and 23.68% for the same value of compression ratio using Haar and biorthogonal wavelets, respectively. The MCA based image processing not only provides a more convenient and cost-effective storage structure for biomedical images but also presents a novel storage solution for compressed images.

# Chapter 4

# Automated Lung Disease Detection and MNIST Digit Classification Using the MCA Framework

## 4.1. Introduction

Coronavirus disease 2019 (COVID-19), an accurate method of diagnosis with less diagnosis time and cost can effectively help in controlling the disease spread with the new variants taking birth from time to time [20]. In order to achieve this, a 2D-TQWT based on a MCA is introduced in this work for the decomposition of chest X-ray images of two different datasets. TQWT has resulted in promising values of PSNR and SSIM at the optimum values of its parameters namely quality factor ($Q$) of 4, and oversampling rate ($r$) of 3 and at a decomposition level ($J$) of 2 [13]. The MCA-based model is used to process decomposed images for further classification with efficient storage. These images have been further used for the classification of COVID-19 and non-COVID-19 images using ResNet50 and AlexNet CNN models. The average accuracy values achieved for the processed chest X-ray images classification in the small and large datasets are 98.82% and 94.64%, respectively which are higher than the reported conventional methods based on different models of deep learning techniques. The average accuracy of detection of COVID-19 via the proposed method of image classification has also been achieved with less complexity, energy, power, and area consumption along with lower cost estimation as compared to CMOS-based technology [46, 66-74].

The current ongoing deep learning technologies are based on CMOS circuits which have more operations in computation [74], area consumption, energy consumption [75], processing time, and power consumption [46]. These technological limitations can be overcome using the MCA as these significantly reduce the power consumption as compared to the CMOS-based conventional systems [65]. MCA is gaining popularity in various domains of image processing, such as pattern recognition and edge detection [76].

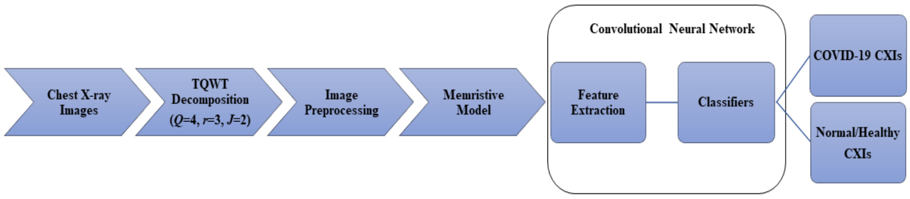


Figure 4.1: Schematic shows the image decomposition and classification of the small and large datasets using the MCA-based model.

MCA is more efficient in terms of energy as well as processing time as compared to the traditional Von Neumann circuits in some applications such as pattern processing [77]. The energy consumption of a memristor-based RRAM is less which attracts a lot of attention to in-memory computation for various applications [74]. Various studies on memristor-based accelerator architectures [77] and memristor-based architectures for neuromorphic applications [29] have been previously published [30]. In conventional CMOS-based neural networks [31], the neurons are represented by capacitors that are bulky and occupy a large area [78], thus making the integration of many neurons in a chip extremely challenging [79]. On the other hand, by representing the neural parameters with the resistance state of memristor cells [31], an MCA can work as a dot-production engine and can eliminate the data transfer overhead of numerous neural weights [80].

## 4.2. Proposed Methodology for Diagnosis of COVID-19

COVID-19 caused by the novel SARS-CoV-2 virus can be understood as a type of pneumonia [13]. Patients diagnosed with COVID-19 suffer from dry cough, sore throat, and fever which may lead to organ failure [20]. The most prevalent method to diagnose COVID-19, the real-time RT-PCR test takes around 10 to 15 hours to produce the result, making the diagnosis process very slow [19]. Another way to diagnose COVID-19 is the rapid diagnostic test (RDT) which takes 30 minutes to give the result. Even though the RDT method is faster, it is less reliable [21]. There is a need to explore other methods for COVID-19 diagnosis, especially in a populous country like India and many countries in the Asian subcontinent. Various studies have shown that COVID-19 affects the lungs of the patient. Hence chest X-ray images of suspected patients are the most feasible method to detect COVID-19 at an early stage [22]. Clinical imaging data are one of the most crucial diagnostic bases in all COVID-19 diagnostic data. Unfortunately, drawing the target area of medical images manually is a time-consuming and laborious task. It increases the burden on the clinicians given the complexity. Therefore, computer technology can be used to diagnose the disease using medical imaging techniques [66]. Deep learning techniques, which are a subset of machine learning techniques, have been explored to diagnose COVID-19 automatically using chest X-ray images [23]. CNNs designed for images that are a class of deep neural networks in deep learning [67]. Residual neural network (ResNet) is a deep CNN, which is used for feature extraction and classification [68]. ResNet50 has been applied in various image recognition and classification applications such as metastatic cancer recognition [69], hyperspectral image classification [27], and chromosome classification [70]. On the other hand, AlexNet is an 8-layer model with 5 convolutional layers and 3 fully connected layers [71], which has various applications in image processing like identification of maize leaf disease [28], COVID-19 virus detection, and power equipment classification [72], scene image classification [73]. ResNet50 and AlexNet are two CNN models explored in this work for the classification of chest X-ray images that are pre-processed by a wavelet decomposition technique called TQWT [18]. The images are decomposed by setting TQWT parameters, namely *Q*, *r*, and *J*, to their optimized values. TQWT is described in detail in the later sections. The usage of TQWT to decompose the input chest X-ray images for classification application using an MCA-based model is novel and has not been reported elsewhere to the best of the author's knowledge. Performance of proposed model computed for two-class classification of chest X-ray image databases such as COVID-19 and normal class.

### 4.2.1. TQWT Image Decomposition with MCA

In this proposed work, chest X-ray images are used to diagnose COVID-19 using the MCA model based on the TQWT image decomposition technique and pre-trained CNN models [71]. Chest X-ray images from two different datasets have been considered: a small dataset [81,82] having a total of 2193 chest X-ray images (COVID-19 chest X-ray images - 852 and normal chest X-ray images - 1341) and a large dataset [30] having a total of 5275 chest X-ray images (COVID-19 chest X-ray images - 2409 and normal chest X-ray images - 2866) have been used [13]. In addition to the RT-PCR test [83], chest X-ray images can also be utilized as an assistive tool to diagnose COVID-19 with the help of image processing techniques with a machine learning algorithm. Many models have been proposed from all around the world for the diagnosis of COVID-19 using chest X-ray images. The best performance has been achieved by the ResNet50 model so far [22]. An accuracy of 98.82% has been achieved using the proposed methodology. A new model named COVID-Net has been proposed by Wang and Wong [84] which utilizes chest X-ray images for COVID-19 diagnosis. This model has achieved an accuracy of 83.5%. Li *et al* [85] have proposed COVNet to detect COVID-19 using chest X-ray images. This model uses ResNet50 as the backbone network [21]. The sensitivity and specificity obtained from the COVNet model are 90% and 96%, respectively [85].

The schematic of the proposed methodology is shown in Fig. 4.1. Firstly, chest X-ray images are decomposed by using TQWT technique; the optimum values for TQWT parameters are determined so that the chest X-ray images can be pre-processed with the parameters of the decomposition set to their optimized values. The sub-bands obtained after each level of decomposition of the image contain both low and higher frequency components. For the higher levels of decomposition, further decomposition is performed iteratively on the approximation component only. As one goes for higher levels of decomposition the classification performance is observed to degrade since these components contain noise present in the image. The chest X-ray images of large and small datasets are decomposed using TQWT technique at an optimized value of $Q$, $r$, and $J$ [18]. The decomposed image coefficients are then stored in an MCA, as shown in Fig. 4.1 [86], where each cross point in the MCA is holding a coefficient value. The input image coefficient values are converted into voltages and fed to the MCA system-based model along the rows [13].

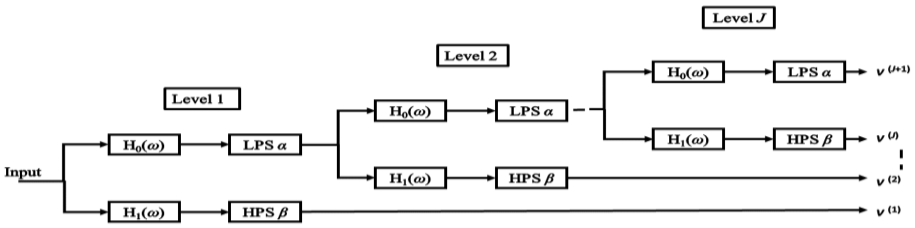


Figure 4.2: Block diagram for TQWT for J level of TQWT decomposition.

The current along the columns is collected and image retrieval is performed using these current values, as can be observed in Fig. 4.1 level decomposition is given in Fig. 4.2. represented by ‘$\omega$’ and further, it is considered as input in the memristive device-based model represented by ‘$v$’. The retrieved chest X-ray images are used for automatic image classification of COVID-19 via pre-trained CNN models using MATLAB version R2021a. Here, ResNet50 and AlexNet CNN models are used to classify chest X-ray images based on COVID-19 cases. A pre-trained adaptation of ResNet50 and AlexNet CNN models is separately processed in our utilized model, and all the chest X-ray images from the datasets are resized based on the input size requirement of the CNN models.

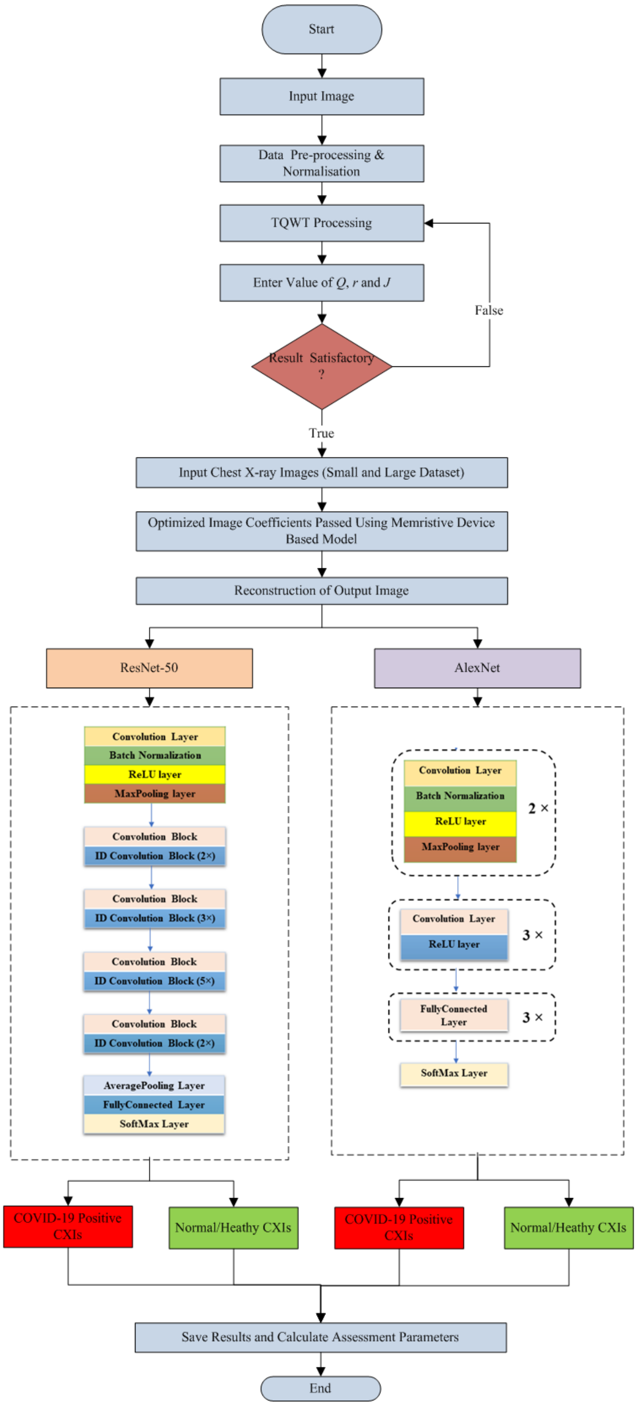


Figure 4.3: The simulation flow of work defines the algorithm for the proposed methodology.

The proposed method has produced remarkable accuracy and has successfully identified COVID-19 positive chest X-ray images as COVID-19 and COVID-19 negative chest X-ray images as Healthy/Normal as shown in Fig. 4.1. There are various wavelets available that could be used for image processing, however, many of the wavelet transforms have limitations due to their constant quality factor [18]. After determining the basis function and decomposition level number, the $Q$ is fixed [44].

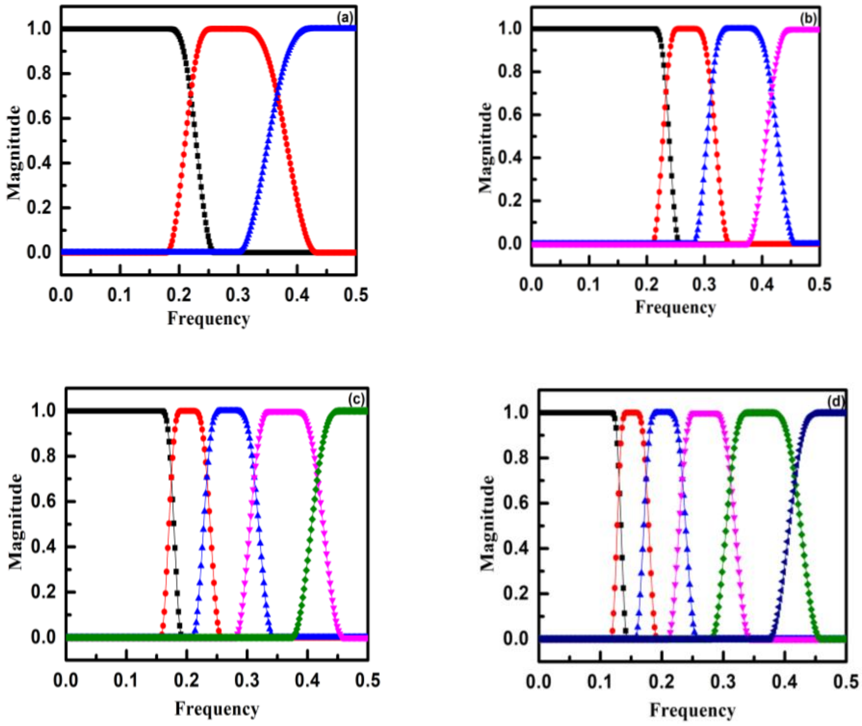


Figure 4.4: Filter-bank for TQWT decomposition at (a) $J = 2$, (b) $J = 3$, (c) $J = 4$, and (d) $J = 5$.

The $Q$ of a wavelet transform has to be in accordance with the oscillatory behaviour of the image to which it is being applied [18]. In most wavelet transforms such as DWT, it is not possible to tune the $Q$, which affects the quality of reconstructed output images, of the wavelet [44]. To overcome the drawback of constant $Q$ in traditional wavelet transforms, Selesnick *et al* [18] has proposed TQWT technique, which is a nonlinear signal decomposition technique that facilitates a suitable $Q$ of the wavelet basis function based on the signal to be decomposed [44]. TQWT technique is efficient in processing one-dimensional signals like speech, cardiac sound [44], and electroencephalogram (EEG) signals [87, 88]. Similarly, TQWT could also be suitable for 2D signals like images with texture variations. $Q$, $r$, and $J$ are TQWT parameters [44]. It can be observed that for $J$ level decomposition, $J$+1 number of sub-bands are obtained which are represented by $v$. The transfer functions of the low-pass and high-pass filter banks are represented by $H_0(\omega)$ and $H_1(\omega)$, respectively. The low-pass coefficient obtained after one stage of decomposition is used as the input for the succeeding stage [13]. At each stage, the low-pass and the high-pass filter are followed by scaling. The parameters '$Q$', and '$r$' are related to the low-pass scaling factor (LPS $\alpha$) and high-pass scaling factor (HPS $\beta$), as shown in Equations (1) and (2).

$$Q = \frac{2-\beta}{\beta} \tag{1}$$

$$r = \frac{\beta}{1-\alpha} \tag{2}$$

The optimum values of $Q$, $r$, and J are determined so that all the chest X-ray images can be pre-processed through TQWT [13]. The decomposed chest X-ray images are stored in a memristive system developed from an analytical model as described in the following subsection.

In Fig. 4. 4, the simulation flow of work represents the algorithm used in the proposed methodology, where the program starts with an input image for optimization of $Q$, $r$, and $J$ in TQWT processing. For optimized conditions, both datasets are being processed which have sub-band image coefficients that pass through the memristive model for further processing using the CNN model. In the proposed methodology, 30% of the dataset is used for training and 70% of the dataset is used for testing the classification model. In the current technology, less number of images are needed for training of the model during the transfer learning approach, as shown by Hu *et al* by using 30% of the input data [87]. The transfer learning technique comes as a rescue provided the input images are resized according to the pre-trained network that is being used [87]. To achieve better performance and reduce the computational complexity with a reduced number of operations, 30% training data is used in the submitted manuscript instead of 70% training data. Two different pre-trained networks, namely ResNet50, and AlexNet, as shown in Fig. 4.3, have been applied for the classification. ResNet50 comprises five stages, namely convolution layer, batch normalization layer, rectified linear unit (ReLU) activation layer, and maximum pooling layer. The next stage comprises of convolution block and an identity convolution block where each block has three convolutional layers in each. The output layer comprises the average pooling layer, fully connected layer, and softmax layer. Similarly, AlexNet consists of five convolutional and three fully connected layers as shown in Fig. 4.3. The outcome of both the networks gives two classes of identification that is COVID-19 positive and normal or healthy chest X-ray images.

## 4.3. Results and Discussion

### 4.3.1. Image classification using CNN with MCA based model

An MCA can be comprehended by a 3-dimensional (3D) structure like a human brain [88, 89]. The MCA offers remarkable downscaling at a nanoscale level which leads to high-density storage, ultrahigh switching speed, and longer operation cyclability which help to design an efficient system for image processing applications [89]. The ability to change synaptic weight is a crucial mechanism used in the process of learning by the human brain [86]. To emulate the brain pattern for image and speech recognition, one can introduce a neuromorphic MCA. As memristor-based systems are non-volatile, low-power consuming, and nanoscale dimensioned they are highly apt for in-memory computing and also for implementing the computing systems [80] like CNNs. The proposed analytical model [86] to develop a neuromorphic MCA-based model is validated via experimental results of $Y_2O_3$-based memristive systems. The nonlinear model describes the synaptic learning of $Y_2O_3$-based devices along with the detailed analytical model. The analytical model used for the study in this paper is represented by Equations (3), (4), and (5). The nature of the MCA to be controlled by flux is expressed through the first term on the right-hand side of the *I-V* relationship shown in Equation (3).

$$I(t) = \begin{cases} b_1 w^{a_1}\left(e^{\alpha_1 v_i(t)} - 1\right) + \chi\left(e^{\gamma v_i(t)} - 1\right), v_i(t) \geq 0 \\ b_2 w^{a_2}\left(e^{\alpha_2 v_i(t)} - 1\right) + \chi\left(e^{\gamma v_i(t)} - 1\right), v_i(t) < 0 \end{cases} \tag{3}$$

The amount of impact of the state variable for positive and negative applied programming voltages on the device current is indicated by the parameters $a_1$ and $a_2$, respectively. The parameters, $b_1$, and $b_2$ sketch the slope of conductance in *I-V* characteristics. The hysteresis loop area controlling parameters are represented by $\alpha_1$ and $\alpha_2$, whereas the state variable is represented by $w$.

$$f(w) = \log \begin{cases} (1+w)^p, \ 0 \leq w \ \leq 0.1 \\ (1.1)^p, \ 0.1 < w \ \leq 0.9 \\ (2-w)^p, \ 0.9 < w \ \leq 1 \end{cases} \tag{4}$$

$$\frac{dw}{dt} = A \times v_i^m(t) \times f(w) \tag{5}$$

The net electronic barrier of the MCA is depicted by the parameters $\chi$ and $\gamma$. The $f(w)$ is the piecewise window function, as shown in Equation (4), making sure that the state variable is confined between 0 and 1. Equation (5) shows the derivative of the state variable in the time domain, where '$A$', and '$m$' determine the impact of the input voltage on the state variable. The analytical model proposed here can be applied to either unipolar or bipolar systems. The value of $p$ restricts the window function between 0 and 1. The developed MCA-based model shows various synaptic functionality such as learning and forgetting behaviour, and synaptic plasticity [90]. Furthermore, the design of the analytical model [86] is inspired by the experimentally fabricated crossbar architecture which has successfully captured various synaptic and RRAM characteristics.

#### 4.3.2. COVID-19 Image Analysis

In this work, the sub-bands that are formed using TQWT-based image decomposition are used for deep feature extraction. Three major experiments are carried out in the current study, the first one is done to identify the best level of image decomposition and to obtain the optimized values of *Q*, *r*, and *J*. Second experiment is performed to process the input images through MCA-based model with TQWT parameters at their optimized values of image decomposition for further diagnosis of COVID-19 with efficient image storage. In the third experiment, the proposed model is studied for image classification of two class chest X-ray image databases by considering the best CNN model, optimizer, and classifier as reported [21].

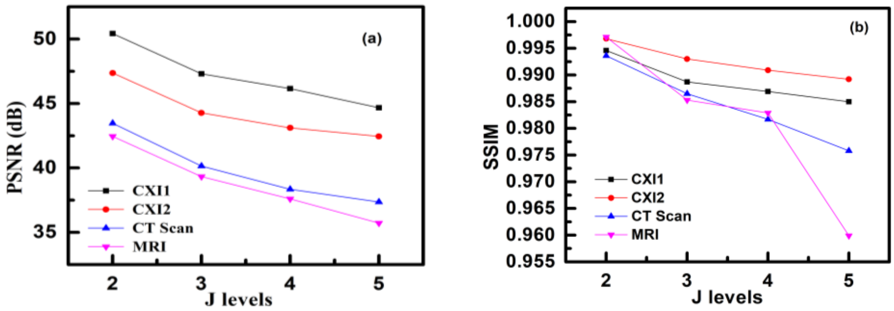


Figure 4.5: Variation in (a) PSNR and (b) SSIM of images for different *J* levels.

TABLE 4.1
INPUT AND OUTPUT IMAGES OBTAINED AFTER DECOMPOSITION USING OPTIMISED TQWT PARAMETERS

| **Images** | **Chest X-ray images 1** | **Chest X-ray images 2** | **CT scan** | **MRI** |
|---|---|---|---|---|
| **Input** | 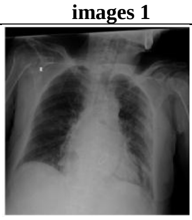 |  | 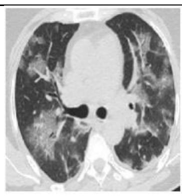 | 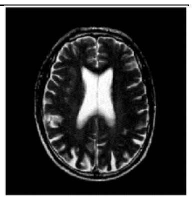 |
| **Reconstructed Output ($Q$ = 4, $r$ = 3, and $J$= 2)** |  |  |  | 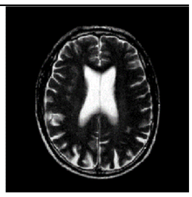 |
| **Quality Measures** | PSNR = 50.4271 dB SSIM= 0.9946 | PSNR = 47.3663 dB SSIM= 0.9968 | PSNR =43.4716 dB SSIM=0.9936 | PSNR = 42.4547 dB SSIM= 0.9971 |

Decomposition has been performed on images mentioned earlier at various values of TQWT parameters and is observed to obtain their optimum values. This method of decomposition is accomplished using a parallel operation of low-pass filtering and high-pass filtering, respectively [18]. The coefficient taken from sub-bands at their optimized parameters is used for further reconstruction of output images. The filter banks applied for various levels of decompositions applied in this work are shown in Fig. 4.4. In Fig. 4.4 (a), (b), (c), and (d) show the magnitude vs frequency plots of TQWT filters for second, third, fourth, and fifth decomposition levels, respectively. For the *J*-level decomposition, we require *J*+1 filters and each of those filters is represented by different colours in Fig. 4.4 for easy differentiation. The PSNR and SSIM values of the input and the decomposed image are observed at different values of *Q*, *r*, and *J*, and these values are tabulated in Table 4.2. The variation in the values of PSNR and SSIM can be observed pictorially in Fig. 4.5(a) and (b), respectively. It can be observed that as the decomposition level is increased, the PSNR and SSIM values decline since the degradation in the image quality increases with the increase in the decomposition level. The same is observed in the cases where *Q* is larger than 4, as seen in Table 4.2, which could be reasoned as the *Q* of wavelet changes that is used for image decomposition the compatibility of the wavelet with the corresponding image changes.

TABLE 4.2
OUTPUT IMAGES AFTER CLASSIFICATION USING MCA-BASED MODEL WITH CONFUSION MATRIX BASED PARAMETERS

| **Chest X-ray Images** | **Small Dataset** | | | | **Large Dataset** | | | |
|---|---|---|---|---|---|---|---|---|
| | **ResNet50** | | **AlexNet** | | **ResNet50** | | **AlexNet** | |
| **COVID-19 Positive** |  | |  | |  | |  | |
| **Normal / Healthy** |  | |  | |  | |  | |
| | **NTP** | 588 | **NTP** | 591 | **NTP** | 1608 | **NTP** | 1584 |
| **Confusio** | **NFP** | 8 | **NFP** | 5 | **NFP** | 78 | **NFP** | 102 |

| | | | | | | | | |
|---|---|---|---|---|---|---|---|---|
| **n Matrix-based parameters** | **NFN** | 6 | **NFN** | 9 | **NFN** | 68 | **NFN** | 113 |
| | **NTN** | 590 | **NTN** | 587 | **NTN** | 1618 | **NTN** | 1573 |

TABLE 4.3
IMAGE CLASSIFICATION QUALITY MEASUREMENT PARAMETERS

| **Chest X-ray Images** | **Small Dataset** | | **Large Dataset** | |
|---|---|---|---|---|
| | **ResNet50** | **AlexNet** | **ResNet50** | **AlexNet** |
| **Confusion Matrix** | 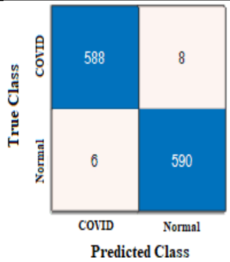 | 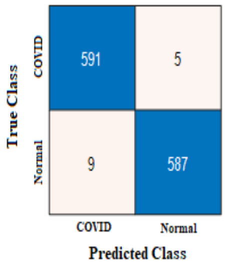 | 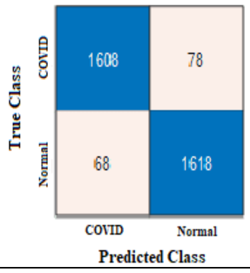 | 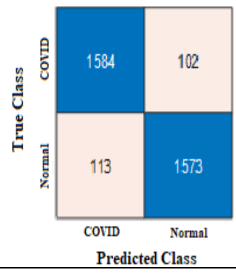 |
| **Accuracy (%)** | 98.82 | 98.82 | 95.67 | 93.62 |
| **Precision (%)** | 98.65 | 99.16 | 95.37 | 93.95 |
| **Sensitivity (%)** | 98.98 | 98.50 | 95.94 | 93.34 |
| **Specificity (%)** | 98.66 | 99.15 | 95.40 | 93.91 |

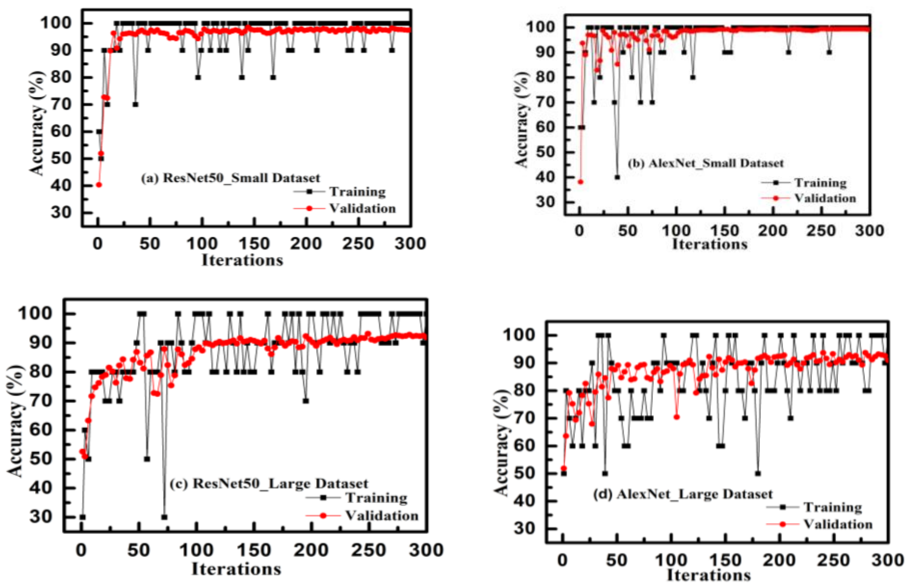


Figure 4.6: Training and validation plots for CNN models deploying (a) ResNet50 for a small dataset, (b) AlexNet for a small dataset, (c) ResNet50 for a large dataset, and (d) AlexNet for a large dataset.

It can be observed that the parameter values $Q$ = 4, $r$ = 3, and $J$ = 2 produce the best results in terms of PSNR and SSIM. It might be because of the compatibility of the wavelet with a $Q$ of 4 and $r$ of 3 with the corresponding image and the fact that lower decomposition level results in better-reconstructed image quality. Implementation of TQWT can also be understood easily by representing it in terms of low pass and high pass filters, Fig. 4.4 shows the filter bank to implement TQWT. In this study best level of decomposition is opted out of level-2, -3, -4, and -5 based decomposition as shown in Table 4.1. The classification performance of COVID-19 from the chest X-ray images database is studied. It has been shown in earlier studies that ResNet50 gives a better performance out of maxima, minima, average, and fusion operations [21]. There are two output classes in the classification: COVID-19 and normal. The input images are designated as chest X-ray image 1, chest X-ray image 2, computed tomography (CT) scan, and magnetic resonance imaging (MRI), where chest X-ray image 1 is a COVID-19 image taken from the large dataset while chest X-ray image 2 is a normal image taken from the small dataset [13]. The CT scan and MRI images are taken from [53] and [54], respectively. These images are considered to observe if the optimum parameters of TQWT decomposition are different for different images. In Table 4.2 the input and output images which are decomposed using the optimized parameters of $Q$, $r$, and $J$ are tabulated along with the corresponding quality measures. The range of the quality measures is different for different images due to the differences in the size and resolution of the images. These specific values of TQWT parameters have been utilized to decompose all the chest X-ray images from the datasets in the next stage of image classification. In this phase, each filter bank has a frequency coefficient represented by '$\omega$' in Fig. 4.3, and the optimized level of decomposed chest X-ray images sub-band ($v$) coefficients are fed as input voltages ($v$) to the MCA-based model as described earlier. The images retrieved from the MCA are then used to train the earlier mentioned CNN models. The parameters used for performance evaluation in this application are accuracy, sensitivity, specificity, and precision [21], which are defined by equations (6), (7), (8), and (9), respectively.

$$Accuracy = \frac{NTP + NTN}{NTP + NFP + NTN + NFN} \quad (6)$$

$$Precision = \frac{NTP}{NFP + NTP} \quad (7)$$

$$Sensitivity = \frac{NTP}{NFN + NTP} \quad (8)$$

$$Specificity = \frac{NTN}{NFP + NTN} \quad (9)$$

In the above equations, NTP, NTN, NFP, and NFN represent the number of true positives, the number of true negatives, the number of false positives, and the number of false negatives, respectively [13]. Fig. 4.6 shows the variation in accuracy with the number of iterations while training, to build the two CNN models. The training accuracies for both datasets have been plotted for small and large chest X-ray image datasets. The training accuracy, though low in the beginning has reached nearly 90% in very few iterations as the CNN model learns the features better with each iteration and improves its ability to classify the chest X-ray images. After a few more iterations the accuracy is always observed to be above 80%.

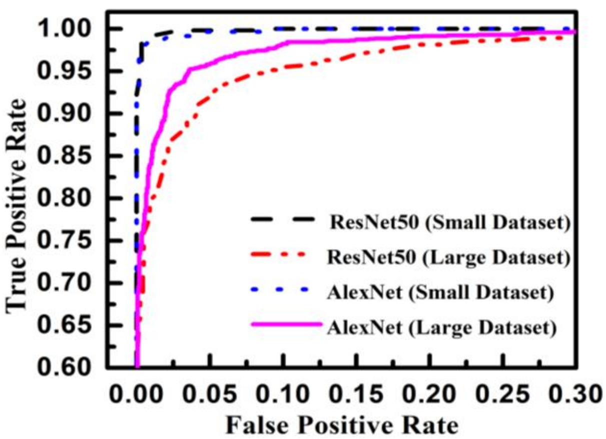


Figure 4.7: ROC plot for small and large datasets for AlexNet and ResNet50 models.

While training the CNN model new data are added for validating the model. The accuracy versus iterations plot during the validation of the models is also shown in Fig. 4.6 (a) and (b) represent training and validation accuracy while building the CNN using the small dataset for ResNet50 and AlexNet models, respectively. Fig. 4.6 (c) and (d) show training and validation accuracy while building the CNN using the large dataset for ResNet50 and AlexNet models, respectively. The training and validation accuracy is better for a small dataset than the large dataset since the small dataset has fewer chest X-ray images to validate and test as compared to those for the large dataset. In the classification of COVID-19 chest X-ray images for small and large datasets, we have achieved a higher value of assessment parameters as compared to the reported results [53] by using TQWT-based decomposed chest X-ray images through the MCA-based model. The confusion matrices obtained after classifying the chest X-ray images from the two datasets using ResNet50 and AlexNet as COVID-19 or normal chest X-ray images. The size of the deep feature vector of the last fully connected layer depends on the type of pre-trained network. A support vector machine is used in the proposed work, as this classifier gives better performance than other reported classifiers for the application of image classification [21].

The true class is represented along the rows and the predicted class is represented along the columns. The first and fourth elements in the matrix give the NTP, NTN and the other elements, i.e., the second and third elements give the NFP, and NFN, respectively, as shown in Table 4.3. The confusion matrix obtained after classifying the CXIs from the two datasets using ResNet50 and AlexNet as COVID or normal CXIs. The different parameters of evaluation have been calculated from the confusion matrix values that are accuracy, sensitivity, specificity, and precision can be observed in Table 4.4. The receiver operating characteristic (ROC) curve, indicating the performance of the classification models which shows the diagnostic capability of the proposed classifier, and the relation between clinical sensitivity and specificity for every possible cut-off, is plotted for both datasets in Fig. 4.7. To obtain the ROC curve, only the true positive rate (TPR) and false positive rate (FPR) are needed as a function of some classifier parameter. Classifiers that give curves closer to the top-left corner indicate better performance. It shows how many correct positive results occur among all positive samples available during the test. FPR, which is calculated by using the formula 'FPR = 1-specificity', is taken on the x-axis. The ROC curve is another appreciable way to visualize the performance of a classifier apart from the quality measurement parameters [91]. From Fig. 4.7, one can conveniently analyse that the small dataset has better ROC which indicates the capability of the classifier to distinguish clearly between two classes. It can be simply understood as a probability curve that informs how good the model is at differentiating the chest X-ray images with COVID-19 and without COVID-19. A good classification model is expected to have covered a large area under its ROC. This way, while comparing multiple models one can select a model by observing the corresponding ROC. In Table 4.5 the performance of the proposed method with the methods available in the literature for diagnosis of COVID-19 from chest X-ray images databases is compared. It has been observed that accuracy, precision, specificity, and sensitivity values of 98.82%, 98.65%, 98.66%, and 98.98%, respectively have been achieved for the classification of images in the small dataset using our proposed ResNet50. For AlexNet models, the corresponding values are 98.82%, 99.16%, 99.15%, and 98.50% for the classification of images in the small dataset as shown in Table 4.5. For the small and large datasets, lower values of assessment parameters have been reported using other reported CNN models, as shown in Table 4.5 [43-47]. For the classification of images in the large dataset by using our utilized model, the values of accuracy, precision, specificity, and sensitivity are 95.67%, 95.37%, 95.40%, and 95.94%, respectively by ResNet50, and 93.62%, 93.95%, 93.91%, and 93.34%, respectively, by AlexNet, these are given in Table 4.5 [ 43, 44, 48-54].

TABLE 4.4
PERFORMANCE COMPARISON OF THE PROPOSED METHOD WITH OTHERS FOR IDENTIFICATION OF COVID-19 USING CHEST X-RAY IMAGE DATABASE

Small Dataset

| Ref. | Models | Accuracy (%) | Precision (%) | Specificity % ) | Sensitivity (%) |
|---|---|---|---|---|---|
| [46] | AlexNet | 99.00 | 98.00 | 99.00 | 99.00 |
| [43] | Covid-Net | 93.30 | 98.90 | - | 91.00 |
| [47] | Modified MobileNet | 95.00 | 99.00 | - | 96.00 |
| Our | ResNet50 | 98.82 | 98.65 | 98.66 | 98.98 |
| | AlexNet | 98.82 | 99.16 | 99.15 | 98.50 |

Large Dataset

| Ref | Models | Accuracy (%) | Precision (%) | Specificity % ) | Sensitivity (%) |
|---|---|---|---|---|---|
| [44] | COVID-Net | 90.10 | 84.00 | - | 98.20 |
| | DenseNet-201 | 91.75 | 94.24 | 78.00 | - |
| [48] | ResNet50+SVM | 95.38 | - | 93.47 | 97.29 |
| [49] | ResNet-101 | 71.90 | - | 71.80 | 77.30 |
| [50] | XCOVNet | 98.44 | 99.29 | - | 99.48 |
| [51] | Xception | 91.00 | 92.00 | - | 87.00 |
| [52] | ResNet-50 | 98.00 | 94.81 | 98.44 | 87.29 |
| [53] | DenseNet-121 | 88.00 | - | 90.00 | 87.00 |
| [43] | Modified ResNet | 99.30 | - | - | 99.10 |
| [54] | XCOVNet | 88.90 | 83.40 | 96.40 | 85.90 |
| Our | ResNet50 | 95.67 | 95.37 | 95.40 | 95.94 |
| | AlexNet | 93.62 | 93.95 | 93.91 | 93.34 |

It has been observed that the level of accuracy of the proposed methodology is 5.92% and 4.02% higher as achieved by others such as Covid-Net [92-95] and Modified MobileNet [96], respectively, for the classification of images in the small dataset by using both the CNN models. For large datasets, the proposed model using ResNet50 has achieved 33.06%, 8.71%, 7.61%, 6.18%, 5.13%, and 4.27% higher accuracy as compared to those obtained by using ResNet-101 [97, 98], DenseNet-121 [99-102], XCOVNet [103], COVID-Net [93], Xception [100], and DenseNet-201 [93], respectively. From the comparative analysis of our proposed work with reported literature for both the small and large datasets, it is evident that most of the performance matrices via conventional technology provide less values of accuracy, precision, specificity, and sensitivity. Although a CNN model [95] from the small dataset, and [92, 99, 101] from the large dataset give better accuracy and sensitivity as compared to those in the proposed work, however, commercially viable technologies for image classification consume more operations in computation, area consumption, energy consumption and processing time which have a direct impact on the cost of the overall system since these are based on CMOS systems [46, 65]. These technological limitations can be overcome using the MCA as these reduce the total energy consumption, the number of operations in computation, area consumption, processing time, and power consumption compared to the conventional system [93] which will be helpful to circumvent Von Neumann bottleneck issues. As given in Table 4.6, Halawani *et al* and Khalid *et al* have demonstrated image processing and digital logic circuits with a reduced number of devices and operations in the MCA-based model as compared to the conventional CMOS-based counterparts [13, 46]. A comparative analysis of compression for (512×512) image is performed using our MCA-based TQWT model and conventional CMOS-based models in which the values of various parameters are taken as in [13, 46]. Table 4.6 displays the achievement of better performances compared to the conventional CMOS-based models. Hence, our proposed approach makes the memristor-based solution very attractive for image processing applications. This components-based study is useful for circuitry design to the application of image classification via MCA model-based architecture [94].

At the hardware level, an MCA will be specifically utilized to accelerate the construction of artificial neural networks. As compared with conventional computer processors [104], the data stored in an MCA are processed in a parallel manner, which increases the computational speed and fault tolerance simultaneously and significantly reduces the system power consumption [33]. In this work, the performance of the proposed method using an MCA-based model is compared with the reported deep learning model based on other conventional technology. Hence, it can be concluded that by using an MCA without compromising the performance in image processing and classification high processing speed with savings in energy, power, area, and cost can be achieved.

TABLE 4.5
COMPARISON OF THE CONVENTIONAL DIGITAL CMOS-BASED COMPUTING WITH THE MCA-BASED IN-MEMORY COMPUTATION [13]

| Compression for (128×128) image [19] | | | |
|---|---|---|---|
| Parameters | CMOS | Memristor | Prominent Improvement |
| Number of Operations | $128^2$×4×5 | $128^2$×2 | 10 times |
| Area ($\mu m^2$) | 327000 | 7864.2 | 5 orders of magnitude |
| Processing Speed (μs) | 19.2 | 15 | 1.28 times |
| Energy Consumption (nJ) | 70.9080 | 6.4398 | 11 times |
| **Full adder circuit by using 3-bit [20]** | | | |
| Parameters | CMOS | Memristor | Prominent Improvement |
| Number of Transistor | 34 | 24 | 10 lesser transistors |
| Processing Time (ps) | 75.3 | 62.4 | 14.84% |
| Power Consumption (μW) | 117.3 | 53.08 | 54.74% |
| **Our work on compression for (512×512) image** | | | |
| Parameters | CMOS | MCA | Prominent Improvement |
| Number of Operations [19, 20] | $512^3$ + ($512^2$×511) | $512^2$ | 1023 times |
| Area ($\mu m^2$) [19] | 1585446.912 | 41943.04 | 37.8 times |
| Energy Consumption (pJ) [19] | 1115.4 | 1.484 | 752 times |
| Processing Time (μs) [19, 20] | 0.15 | 0.06 | 2.5 times |
| Power Consumption (mW) [19] | 7436 | 24.733 | 300 times |

This work explores the merits of employing TQWT and MCA based techniques for effective detection of the COVID-19 virus through chest X-ray images. Further, the highest values of peak signal to noise ratio and structural similarity index for chest X-ray image is 50.4271 dB and 0.9946, respectively, for the optimized TQWT parameters, namely $Q$ = 4, $r$ = 3, and $J$ = 2. The utilized method can overcome the limitations of the CMOS-based technology and is feasible with less complexity, processing speed, energy, power, and area consumption along with lower cost estimation as compared to current technology. This study is carried out to find the optimum values of parameters for the decomposition of chest X-ray images using a TQWT. By using the obtained optimum parameters, remarkable values of PSNR and SSIM are achieved. From the decomposed images, which are stored in the MCA, features are extracted using two different convolutional neural network models: ResNet50, and AlexNet. High average accuracy values of 98.82% and 94.64% are achieved by using the MCA-based model for small and large datasets containing 2193 and 5275 chest X-ray images, respectively [13]. The image processing capability of the MCA-based model improves the operational efficiency of the neural network and reduces the energy consumption of the system as compared to other reported convolutional neural network models. In addition, the MCA model-based image processing technology can enhance the processing speed and accuracy along with the reduction in the number of operations, area, and energy consumption. This work can be further extended to identify different stages of coronavirus disease 2019 and to build an on-chip architecture based on an MCA. It can also be modified to diagnose other diseases like influenza and tuberculosis, from chest X-ray images, CT scans, and other imaging techniques.

### 4.3.3. Pneumonia Detection using Chest X-ray Image Analysis

The application of two CNN models, EfficientNet and NASNet in the classification of chest X-ray images that have been pre-processed using the TQWT. [70]. Wavelet transforms, which possess the ability to localize offer multiresolution features, have found extensive usage in several image processing applications, such as edge detection and image compression [13]. The TQWT parameters were optimized to obtain the decomposed images, which were then classified into the two classes of pneumonia and healthy chest x-ray images. This research marks the establishment of the application of TQWT in decomposing chest X-ray images for classification through the memristive model.

Traditional deep learning technologies are dependent on CMOS circuits, which are restricted by significant computational operations, area demands, energy consumption, processing time constraints, and power consumption requirements [66].

The performance of the biological brain in terms of brain-inspired computing is modelled using memristive devices. In biological systems, neurons and synapses include dendrites positioned between pre-neurons and post-neurons via synapses [46]. Information is transferred to the synaptic terminal through the axon, which functions similarly to artificial memristive neurons [13]. This study uses an analytical model of a memristive device, featuring a structure with gallium zinc oxide (GZO) as the bottom electrode, aluminium (Al) as the top electrode, and $Y_2O_3$ as the resistive switching layer [66]. The memristive device-based model is activated by voltage ($v$) corresponding to pixel values $V_{R1}$, $V_{R2}$, ..., $V_{RM}$, with a normalizing voltage $V_{Avg}$. It generates spike events via the membrane, analogous to the soma of a neuron [66]. The concept of memristive biological neurons is inspired by the intricate structure and complex functioning of biological neurons found in the human brain. These artificial neurons mimic the way biological neurons process and transmit information, utilizing memristive devices to emulate synaptic behaviours such as learning and memory retention. Memristive biological neurons hold significant potential in the realm of artificial intelligence, particularly for tasks that require efficient and accurate image classification. By leveraging the unique properties of memristors, these neurons can process vast amounts of data swiftly and with high precision, thereby enhancing the performance of AI systems in recognizing and categorizing images [66]. A MCA-based model framework, characterized by lower power consumption compared to CMOS based systems, has the potential to scale these technological constraints [13]. When it comes to tasks like pattern processing, the memristive model shows better processing speed and energy efficiency than Von Neumann circuits especially when applied to neural networks

[66]. Extensive research has been conducted on utilizing memristive model for various applications, including neuromorphic computing particularly in neural network applications [46]. The MCA based model [86] can function as a vector matrix multiplication, that eliminates the necessity for transferring large amounts of neural weights data, making them highly compatible substitutes for CMOS based neural networks. To address the limitations of previous studies, this research aims to optimize the TQWT parameters for image decomposition and utilize the memristive model to conduct mathematical research on the 2D TQWT for further applications in image decomposition and classification [13]. The processed images are utilized for computational diagnosis and early disease detection of pneumonia and other infectious lung diseases via CNN models, which analyse chest X-ray images. Memristive model-based devices present an advantage in image processing due to their simultaneous storage and processing capabilities, non-volatile memory, and adaptability [46]. This offers the potential for the development of more efficient and intelligent systems in image processing applications with cost effectiveness. The key benefits of using memristive model in computational tasks include high density, low power consumption, and the ability to perform parallel computations, making them ideal for implementing neural networks [13] as shown in Fig. 4.8 (a) and (b).

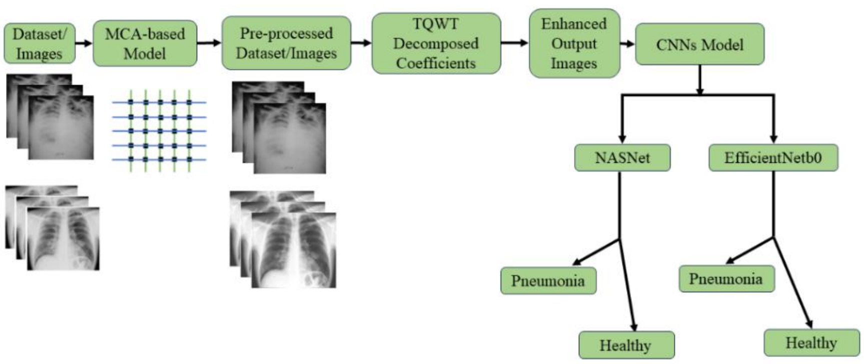


(a)

(b)

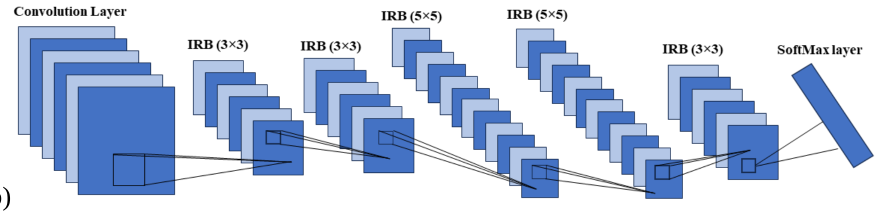


Figure 4.8. (a) Overview frame of the proposed work (b) automated image classification for the diagnosis of pneumonia diseases, where inception residual block (IRB) is used in CNN Model.

In this proposed study, pre-trained CNN models from MATLAB version R2021a are employed to automatically classify chest X-ray images for early detection of pneumonia as shown in Fig. 4.9. Classification experiments were conducted to demonstrate the performance improvement across various neural network input sets. For image decomposition simulation results indicate that the parameter values $Q = 4$, $r = 3$, and $J = 2$ produce the best output image quality due to the compatibility of the wavelet as shown in Fig. 4.4. The study utilizes the TQWT technique, where each filter bank is assigned a frequency coefficient represented by '$\omega$'. The memristive model is fed with optimized levels of decomposed sub-band ($v$) coefficients from chest X-ray images as input voltages ($v$). The output images obtained from the memristive model are employed to train the CNN models. To evaluate the quality of both the input and decomposed reconstructed output images, authors assess them using the PSNR and SSIM at varying values of $Q$, $r$, and $J$, the results are summarized in Table 4.2. The TQWT technique is used each filter bank within the system has a frequency coefficient denoted as '$\omega$', and the optimized level of decomposed chest X-ray image sub-band ($v$) coefficients serves as input voltages ($v$) for the memristive model [46]. The resulting images from the memristive model are utilized for training the CNN models. The suggested approach utilizes a 30% training and 70% testing division of the dataset to assess the classification model, as outlined in Table 4.4.

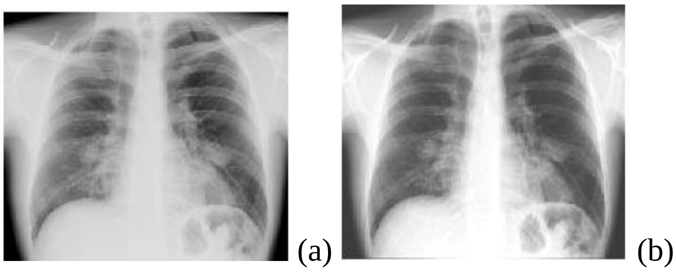


Figure 4.9: Pneumonia Infected Chest X-ray Image (a) Image from Raw Dataset (b) Processed Image using Proposed Methodology

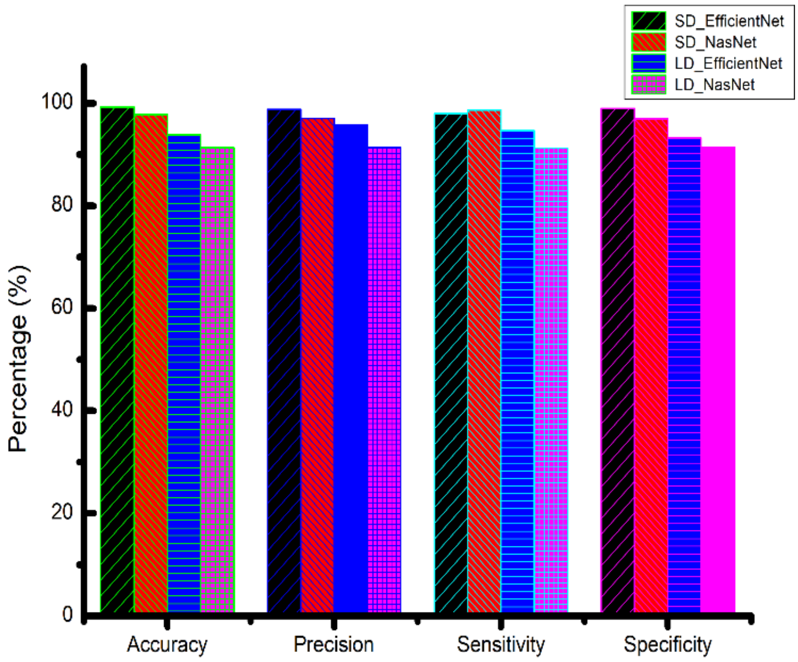


Figure 4.10: Assessment parameter of classified results using CNN models for small dataset (SD) and large dataset (LD).

Earlier studies conducted by Halawani *et al.* and Khalid *et al.* have showcased the efficiency of memristive model in image processing and digital logic circuits [13]. These models exhibit a decrease in device count and operations when compared to traditional CMOS-based models [29, 30]. To evaluate the compression effectiveness of the memristive model integrated with the TQWT model relative to traditional CMOS based models, the authors conducted an extensive analysis using a (512×512) image. The comparison involved employing parameter values derived from sources [66, 29, 30], as detailed in Table 4.4. The proposed EfficientNet exhibits remarkable performance in classifying images within the small dataset, achieving Acc, Pre, Spe, and Sen values of 99.24%, 98.77%, 97.98%, and 98.96%, respectively, as detailed in Table 4.4.

Similarly, the NASNet models demonstrate commendable results in the small dataset, with corresponding values of 97.82%, 97.03%, 98.66%, and 96.98% as shown in Fig. 4.10. In contrast, other reported CNN models, as shown in Table 4.4 [31, 78, 79], present lower assessment parameter values for both small and large datasets. For image classification in the large dataset, one employed EfficientNet model yields Acc, Pre, Spe, and Sen values of 93.84%, 95.72%, 94.68%, and 93.24%, respectively.

TABLE 4.6
IMAGES RESULTING FROM INPUT AND OUTPUT DECOMPOSITION USING OPTIMIZED TQWT PARAMETERS

| Images | Infected CXIs | Normal CXIs |
|---|---|---|
| Input |  |  |
| Output ($Q = 4$, $r = 3$, and $J = 2$) |  |  |
| Quality Assessment Parameters | PSNR = 51.5671 dB<br>SSIM= 0.9978 | PSNR = 48.6334 dB<br>SSIM= 0.9846 |

The NASNet model achieves corresponding values of 91.31%, 91.34%, 91.28%, and 91.34%, as outlined in Table 4.4 [78, 80, 81-83]. A comprehensive comparative analysis with existing literature highlights that conventional technologies consistently exhibit lower values in terms of Acc, Pre, Spe, and Sen for both small and large datasets. While some CNN models may demonstrate superior performance compared to our proposed method in terms of Acc and Sen, it is crucial to acknowledge that commercially viable image classification technologies typically meet issues such as higher computational demands, increased area and energy consumption, and longer processing times due to their dependence on CMOS systems [29, 30].

However, these challenges can be effectively addressed by integrating memristive devices [66, 29-30]. By using memristive devices, one can reduce the problems linked with traditional CMOS based methods, leading to better and more efficient ways of classifying images, this is reflected in the comparative results presented in Table 4.8 in terms of PSNR and SSIM. Memristive model addresses these technological limitations by significantly reducing total energy consumption, computational operations, area consumption, processing time, and power consumption compared to conventional systems as shown in Table 4.5 [29, 30]. This not only helps overcome Von Neumann bottleneck issues but also presents a more cost-effective solution for image classification systems. It is noteworthy that EfficientNet demonstrated a particularly high Acc, especially for smaller datasets, as illustrated in Fig. 4.6 because of internal architecture compatibility with proposed classification. This superiority is attributed to the internal architecture compatibility of EfficientNet with proposed memristive model framework, facilitating effective image decomposition and classification [84, 85]. The Internet of Things (IoT) is rapidly expanding, with billions of interconnected devices generating and processing data [13]. However, limitations in communication bandwidth and device storage pose significant challenges. This is where memristive model framework step in, offering a revolutionary approach that not only gives higher processing speed but also significantly reduces the compression ratio needed for data transmission and image processing within IoT networks. The use of memristive model significantly speeds up the processing time compared to traditional digital systems, enabling rapid diagnosis. An MCA model is highly scalable, allowing for larger and more complex CNN models to be implemented [46]. The analogue nature of MCA based model computations reduces energy consumption, making the technology suitable for deployment in resource constrained environments like portable diagnostic devices [13]. Future research could focus on improving the precision and robustness of memristive device-based model, developing more sophisticated CNN architectures tailored to pneumonia detection, and exploring the integration of this technology into clinical practice for broader use in medical diagnostics.

### 4.3.4. MCA based Window Function as an Activation Function

The development of Artificial Neural Networks (ANNs) has significantly advanced Machine Learning (ML). ANNs consist of layers of artificial neurons, inspired by biological neurons, connected by weights ($w_1$, $w_2$, and $w_3$) and biases ($b$) as shown in Fig. 4.11. An essential component is the activation function, which introduces non-linearity, allowing the network to learn complex patterns [23]. Input sequences $X_1$, $X_2$, and $X_3$, and corresponding outputs $Y$ illustrates weight initialization, output computation, error determination, and weight adjustment in an iterative process aiming to minimize error as shown in Table 4.7.

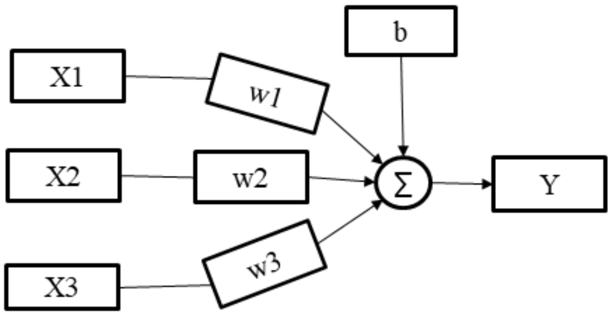


Figure 4.11: Memristive device-based window function as activation function for artificial neural network.

TABLE 4.7
COMPARATIVE ANALYSIS OF THE SIGMOID ACTIVATION FUNCTION AND THE MEMRISTIVE MODEL-BASED WINDOW FUNCTION AS ACTIVATION FUNCTIONS

| Input | Correct output | Sigmoid correct output | Memristive device-based activation function_correct output |
|---|---|---|---|

| | | | |
|---|---|---|---|
| {001} | {0} | 0.0102 | 0.00067592 |
| {011} | {0} | 0.0083 | 0.00062701 |
| {101} | {1} | 0.9932 | 0.9994 |
| {111} | {1} | 0.9917 | 0.9994 |

Without it, the network's output would be a linear combination of inputs, regardless of the number of layers. This work proposes a new activation function inspired by the $Y_2O_3$-memristive model as shown in equations (4), and (5). The piecewise window function *f*(*w*) shown in equation (4), ensures the state variable stays between 0 and 1. Equation (5) describes the time-domain derivative of the state variable, with '*A*' and '*m*' representing the influence of input voltage. This analytical model is applicable to both unipolar and bipolar systems, with '*p*' limiting the window function to the 0 to 1 range. Training and testing were performed using both the sigmoid activation function as shown in equations (6) and the proposed function.

The proposed activation function achieves an efficiency of 99.94% with a parameter value of '*p*' set to 3, compared to 99.32% with the sigmoid function as shown in Table 4.7. MCA based window function [86] shown in equation (4) and (5) and sigmoid activation function [17] shown below in equation (10):

$$\text{Sigmoid function: } \varphi(x) = \frac{1}{1+e^{-x}} \tag{10}$$

As an activation function used for pattern detection with higher accuracy, it demonstrates that the identification accuracy for pneumonia should be improved using a memristive device-based model. Due to the issue of vanishing gradients with the sigmoid activation function which can weaken training and cause gradients to vanish [6], the proposed memristive model-based window function aims to deliver more effective performance in deep networks.

#### 4.3.5. Handwritten Digit Recognition using MCA based Model

The MNIST dataset consists of handwritten digits from 0 to 9 as shown in Fig. 4.12. They act as the output classes during classification using

CNN. The handwritten digit recognition using memristive system is performed in MATLAB environment. Initially the training and testing data is read in the script, the training data has around 60000 images and the test data has around 10000 images in the form of 784 (28 × 28) row vectors of pixel values along with their labels. Next step is to separate the labels and pixel values from both train and test data, then the pixel values are normalized so that all of them are in the range of 0-1. This is followed by reshaping all the row vectors into 28 × 28 images that can used as inputs for the CNN. Before classifying them all the images are fed to the memristive crossbar array developed using the above discussed analytical model. The image pixel values are given as voltages, that storing the images in memristive devices reduces lot of area requirement and power consumption. For retrieving the pixel values the output current from the MCA based model is utilized.

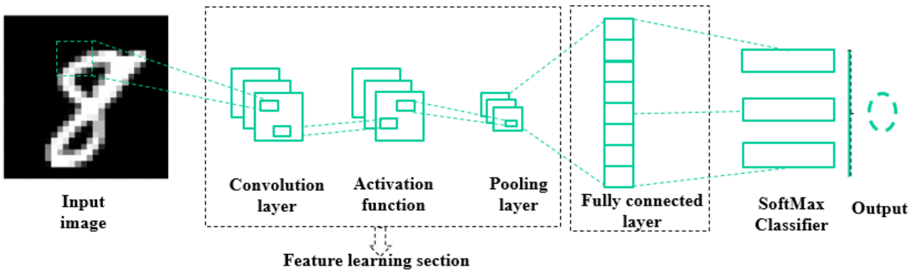


Figure 4.12: Integration of MCA and CNN for handwritten digit recognition based on dimensionality reduction in each stage

In this work the recognition task is achieved by a 7-layer CNN comprising of 1 convolutional layer, 1 maxpooling layer, 2 fully connected layers, 1 dropout layer, 1 softmax layer and 1 classification layer. The block diagram of the model can be observed in Fig. 4.12. Convolution operation is used in the convolutional layer to extract information by dividing the numerical images into overlapping blocks. It can be interpreted as filtering the images using many parallel filters. In the first layer i.e., the convolutional layer the 28 × 28 image is filtered using 32 filters of size 3 × 3. The result of this filtering of each block by all the filters is a weighted sum of the pixel values for 32 channels. This weighted sum is fed as input to the nonlinear rectified linear unit (ReLU) activation function. Activation functions are necessary to prevent the network neurons from exploding or dying. The convolutional layer is succeeded by a maxpooling layer of pool size 3 × 3. Pooling layer is required to remove the redundant information and the size of the image [13]. The maxpooling layer considers all pixels from one channel generated by the convolutional layer and divides them into number of non-overlapping blocks. The output of this layer is reduced in size by combining the neighbouring pixels into a single pixel. It is followed by two fully connected layers of output size 64 and 10 respectively with a dropout layer of probability 10 between them. Dropout layer is needed to avert overfitting of the model. The last two layers of the CNN are the softmax layer and the classification layer which give the result of handwritten digit recognition.

| | **CONFUSION MATRIX** | | | | | | | | | | **LOSS** | **ACCURACY** |
|---|---|---|---|---|---|---|---|---|---|---|---|---|
| **TRUE CLASS** | 972 | 1 | 4 | 1 | 0 | 0 | 2 | 0 | 0 | 0 | 0.8% | 99.2% |
| | 0 | 1131 | 1 | 2 | 0 | 1 | 0 | 0 | 0 | 0 | 0.4% | 99.6% |
| | 1 | 4 | 1017 | 0 | 3 | 0 | 1 | 5 | 1 | 0 | 1.5% | 98.5% |
| | 0 | 0 | 2 | 1001 | 0 | 4 | 0 | 1 | 1 | 1 | 0.9% | 99.1% |
| | 1 | 1 | 0 | 0 | 970 | 0 | 4 | 0 | 0 | 6 | 1.2% | 98.8% |
| | 2 | 0 | 0 | 3 | 0 | 885 | 2 | 0 | 0 | 0 | 0.8% | 99.2% |
| | 6 | 2 | 0 | 0 | 1 | 1 | 948 | 0 | 0 | 0 | 1.1% | 98.9% |
| | 0 | 6 | 9 | 2 | 0 | 1 | 0 | 1003 | 1 | 6 | 2.4% | 97.6% |
| | 2 | 1 | 2 | 2 | 2 | 2 | 3 | 1 | 956 | 3 | 1.9% | 98.1% |
| | 3 | 0 | 0 | 1 | 5 | 3 | 0 | 4 | 1 | 992 | 1.7% | 98.3% |
| | **PREDICTED CLASS** | | | | | | | | | | | |
| **LOSS** | 1.6% | 1.3% | 1.8% | 1.1% | 1.2% | 1.4% | 1.2% | 1.1% | 0.5% | 1.6% | | |
| **ACCURACY** | 98.4% | 98.7% | 98.2% | 98.9% | 98.8% | 98.6% | 98.8% | 98.9% | 99.5% | 98.4% | | |

Figure 4.13: Confusion matrix-based output data for image classification of MNIST dataset

As the number of iterations increased the loss went significantly low. An accuracy of 98.86% has been achieved for the handwritten digit recognition using memristive system. The confusion matrix for this classification can be observed in Fig 4.11. Using the MCA based model has improved the efficiency of the classification. While preforming the same task without the MCA based model, on a CMOS device has resulted in an accuracy of 98.75%.

## 4.4. Conclusion

In this study, the authors explore the advantages of utilizing TQWT and memristive model-based approaches for the early detection of viral lung infections of pneumonia through the analysis of chest X-ray images. The proposed activation function outperforms the sigmoid, achieving an efficiency of 99.94% with a parameter value of ‘$p$’ set to 3, compared to 99.32% for the sigmoid function. The researchers have identified optimized TQWT parameters, $Q = 4$, $r = 3$, and $J = 2$, which have produced the highest PSNR and SSIM index of 51.5671 dB and 99.78%, respectively. The proposed approach demonstrates practicality through decreased complexity, processing speed, energy and area consumption, as well as reduced cost compared to existing technology, thereby overcoming the limitations associated with CMOS based technology. The study has determined the ideal parameter values for the TQWT-based decomposition of chest X-ray images, which are integrated with a MCA based model employed to store the coefficients of the decomposed images. Two different models of CNNs, EfficientNet and NASNet, have been utilized to extract features from the images and train the models, respectively, resulting in high Acc values of 99.24% for both small and large datasets comprising several chest X-ray images. The MCA based model can enhance the neural network efficiency, reduces energy consumption, increases processing speed, and improves accuracy of the system. This research can be further enhanced by designing an on-chip architecture based on MCA based model and identifying the various stages of lungs infection. The TQWT technique excels at identifying subtle early-stage texture variations in decomposed images, while the memristive model enhances feature extraction and classification accuracy. This combined approach reduces false negatives by improving contrast resolution in challenging regions and enables efficient automated screening - a capability particularly valuable in resource-limited settings. Most importantly, by facilitating earlier and more reliable detection of conditions like pneumonia, our method supports timely clinical intervention and improved patient outcomes. The versatility of the method extends beyond its current application, as it can be designed to diagnose additional diseases such as tuberculosis and influenza through the analysis of chest X-ray images, CT scans, and other imaging modalities.

# Chapter 5

# MCA-Inspired Automated Glaucoma Detection from Fundus Images using 2D FBSE-EWT

## 5.1. Introduction

The evolution Ocular disorders affect over 2.2 billion people worldwide, with glaucoma emerging as a leading cause of blindness in India. Early detection of glaucoma is vital because it progressively damages the optic nerve due to high fluid pressure, resulting in vision impairment. This study presents an innovative approach to glaucoma detection and diagnosis known as the 2D FBSE-EWT, integrating a model based on a MCA [86]. The proposed method relies on deep learning and an ensemble EfficientNetb0-based technique to identify whether a fundus image is normal or shows signs of glaucoma. Compared to other CNNs models like ResNet50, AlexNet, and GoogleNet, EfficientNetb0 performs better, making it the best option for classifying glaucoma. Initially, researchers processed the dataset using an integrated model of MCA with 2D FBSE-EWT, and reconstructed images used for further classification. The assessment parameters of reconstructed output images revealed their high quality, as indicated by elevated values of PSNR = 26.2346 dB and SSIM = 95.38%. The proposed method exhibits outstanding performance, achieving an accuracy of 94.15% using EfficientNetb0. Furthermore, the proposed methodology enhances accuracy and sensitivity by 32.14% and 40.93%, respectively, compared to the unprocessed dataset.

## 5.2. Proposed Methodology for Early Detection of Glaucoma

### 5.2.1. 2D FBSE-EWT Integration with MCA-based Model

Glaucoma, primarily occurs due to an imbalance between fluid production and drainage, resulting in increased pressure on the optic nerve head (ONH) and subsequent damage. As a leading cause of blindness, glaucoma often manifests without early-stage symptoms. The condition is characterized by elevated fluid pressure within the optic nerve, resulting from a blockage in the eye's drainage system, ultimately causing damage to the ONH [24]. Deterioration of the optic nerve can be detected through fundus images, leading to structural alterations in the optic nerve head and impacting vision.

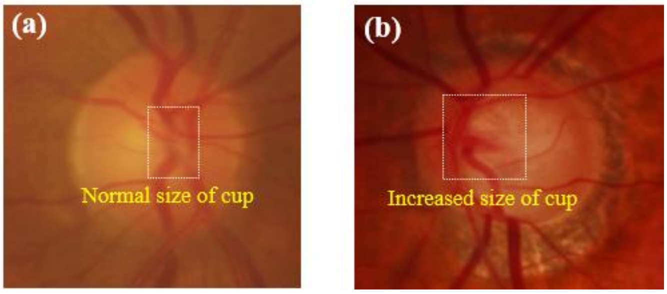


Figure 5.1: Fundus images of different class (a) Healthy (b) Glaucoma.

It is crucial to prioritize early detection and diagnosis of glaucoma owing to its cause blindness in the absence of prompt intervention. Recently, biomedical imaging technique has emerged as a formidable tool for the non-invasive detection and diagnosis of a wide variety of human diseases [105]. The biomedical imaging field, stemming from the discovery of X-ray [23] has seen the development of diverse imaging models, including electromagnetic spectrum, radio, ultrasound, microscope, and others imaging techniques [106]. Moreover, eye diseases can be similarly detected early by employing biomedical imaging techniques, particularly fundus imaging [107]. Among the diseases that can be detected and diagnosed from fundus images, glaucoma detection and diagnosis is an active area of research due to the potential severity of the condition. Glaucoma can take different forms, the most common is primary open angle glaucoma, which gradually affects vision. There is also angle closure glaucoma, where eye pressure suddenly spikes, requiring urgent attention [23]. Some individuals experience normal tension glaucoma, where eye pressure remains normal, but vision is still in danger. Secondary glaucoma and different types can result from various eye or body conditions, making it vital to pinpoint the specific type for the right treatment and the protection of your eyesight [23]. The proposed research aims to precisely categorize fundus images, as illustrated in Fig. 5.1, to detect signs of glaucoma or normal conditions, particularly in cases where the cup size varies. Early detection of glaucoma is paramount in preventing long-term vision loss [105].

In recent years, several automated machine-learning algorithms have been developed for glaucoma diagnosis using fundus images. Encompassing those different approaches have been explored, such as ANN [108], SVM [25], Gabor transform [109], Radon transform [26], wavelet-based decompositions [110], and DL techniques [5]. However, these methods employ various image preprocessing techniques, and classification algorithms using CNNs to detect glaucoma. Henceforth, DL ensemble EfficientNetb0 model using 2D FBSE-EWT with MCA based model has shown promising performance in glaucoma detection and diagnosis compared to traditional machine learning and DL algorithms [5]. Furthermore, the traditional methods have encountered several challenges in decomposing 2D signals, due to limitations such as interference, incompatibility with non-stationary signals, lack of adaptability, and limited scale coverage [23]. While the 2D FBSE-EWT is adaptive in nature, it suffers from interference and redundancy issues in image spectrum segmentation. This section provided an overview of the related work in fundus image classification, emphasizing the predominant use of conventional methods that involve traditional machine learning algorithms.

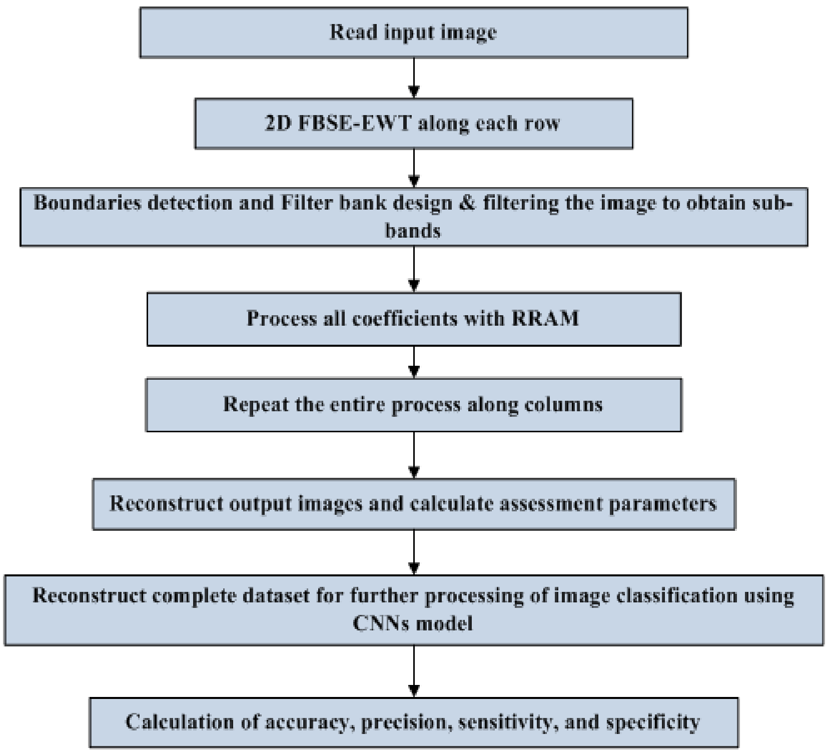


Figure 5.2: Flow chart of proposed methodology for image classification.

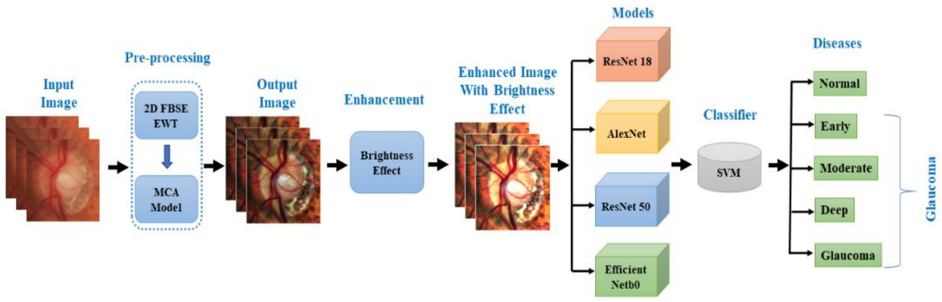


Figure 5.3: The overall structural outline of the proposed ensemble method for the classification of glaucoma and normal using fundus image dataset via CNNs.

Effectively harnessing recent advancements in deep learning, particularly CNNs, has proven successful for early disease detection and diagnosis, though challenges such as limited datasets and model interpretability persist. In the following sections, authors present their proposed methodology as shown in Fig. 5.2 and Fig. 5.3 to address these challenges and further advance the field of fundus image classification. The field of fundus image classification, particularly in the context of accurate diagnosis and classification of ocular diseases, has collected significant attention in recent years [25, 26, 108-110]. Researchers have explored various approaches and methodologies to tackle these challenges. CNNs have emerged as the preferred architecture for learning discriminative features directly from raw images [13, 111-115]. In this work, authors have introduced an integrated MCA-based model with 2D FBSE-EWT techniques via CNNs for the classification of fundus images, as depicted in Fig. 5.4. This provides an overview of ensemble method in the structural framework for classifying glaucoma and normal images using a fundus image dataset and CNNs for early detection and diagnosis of disease.

This section provided an overview of the related work in fundus image classification, emphasizing the predominant use of conventional methods that involve traditional machine learning algorithms. Effectively harnessing recent advancements in deep learning, particularly CNNs, has proven successful for early disease detection and diagnosis, though challenges such as limited datasets and model interpretability persist. In the following sections, authors present their proposed methodology as shown in Fig. 5.2 and Fig. 5.3 to address these challenges and further advance the field of fundus image classification. The field of fundus image classification, particularly in the context of accurate diagnosis and classification of ocular diseases, has collected significant attention in recent years [25, 26, 108-110]. Researchers have explored various approaches and methodologies to tackle these challenges. CNNs have emerged as the preferred architecture for learning discriminative features directly from raw images [13, 114, 115]. In this work, authors have introduced an integrated MCA-based model with 2D FBSE-EWT techniques via CNNs for the classification of fundus images, as depicted in Fig. 5.4. This provides an overview of ensemble method in the structural framework for classifying glaucoma and normal images using a fundus image dataset and CNNs for early detection and diagnosis of disease.

The proposed methodology, as depicted in Fig. 5.4, involves a sequence of steps. Initially, datasets are processed through a 2D FBSE-EWT and MCA-based model. The utility of 2D FBSE-EWT extends beyond physics and engineering into fields like signal and image processing. In medical imaging, and signal processing applications, where non-stationary data is common, 2D FBSE-EWT allows for effective analysis and reconstruction. The only shortcoming of using 2D-FBSE-EWT is computational time due to implementation FBSE spectrum instead of Fourier transform. But due to ongoing advancements in numerical methods and computing technology, 2D FBSE-EWT remains a crucial tool for solving problems, ensuring its enduring relevance in both research and practical applications. The output image is subsequently processed to improve the quality of the reconstructed output image through the optimization of its brightness effects. Subsequently, the reconstructed output images are used for further biomedical image classification using CNN models for the detection and diagnosis of glaucoma at the early stage, as illustrated in Fig. 5.4.

TABLE 5.1: PHYSICAL SIGNIFICANCE AND VALUES OF PARAMETERS FOR MCA-BASED MODEL [19]

| **Parameters** | **Values for $Y_2O_3$** | **Physical Representation** |
|---|---|---|
| $b_1$ | $1.59 \times 10^{-3}$ | Fitting parameters of experimental data |
| $b_2$ | $-6.2 \times 10^{-4}$ | Fitting parameters of experimental data |
| $a_1$ | 1.2 | State variable degrees influence under positive bias |
| $a_2$ | 0.3 | State variable degrees influence under negative bias |
| $\alpha_1$ | 0.60 | Area controlling parameters of Hysteresis loop under positive bias |
| $\alpha_2$ | -0.68 | Area controlling parameters of Hysteresis loop under negative bias |
| $\varkappa$ | $1 \times 10^{-11}$ | Magnitude of ideal diode behavior |
| $\gamma$ | 1 | Diode characteristics like the ideality factor and thermal voltage |
| $A$ | $5 \times 10^{-4}$ | Control the window function’s impact |
| $m$ | 5 | Control the input’s impact on the state variable. |
| $p$ | $0 < p \leqslant 10$; $p = 2$ | Window function bounding parameter between 0 and 1 |

The MCA-based model is analogous to the human brain, providing excellent downscaling capabilities at the nanoscale level. This allows for efficient image processing [116] with ultrahigh switching speed, high-density storage, and longer operation cyclability [117]. A key mechanism for learning in the human brain is the ability to change synaptic weight, and a neuromorphic MCA-based model can be used to replicate this capability for image and speech recognition patterns [118]. MCA-based model are particularly well-suited for in-memory computing and implementation of computing systems like CNNs due to their non-volatile, power-efficient, and nanoscale-sized nature [119]. Experimental findings from $Y_2O_3$-based MCA model are used to validate the analytical model that has been proposed [120] to create a neuromorphic MCA-based model. In addition to the complex analytical model [86], the synaptic learning of $Y_2O_3$-based devices [120] is also described in the nonlinear model. Equations (1), (2), and (3) represent the analytical framework for the research presented in this paper. The first term on the right side of the *I-V* relationship in Equation (1) represents the flux-controlled nature, and the second term shows ideal diode behaviour, respectively.

$$I(t) = \begin{cases} b_1 w^{a_1}\left(e^{\alpha_1 v_i(t)} - 1\right) + \chi\left(e^{\gamma v_i(t)} - 1\right), v_i(t) \geq 0 \\ b_2 w^{a_2}\left(e^{\alpha_2 v_i(t)} - 1\right) + \chi\left(e^{\gamma v_i(t)} - 1\right), v_i(t) < 0 \end{cases} \quad (1)$$

The physical significance of parameters used in MCA-based model are described as $b_1$ and $b_2$ are experimental fitting parameters. $a_1$ and $a_2$ represent degrees of influence of the state variable under positive and negative bias, respectively. $\alpha_1$ and $\alpha_2$ denoted the hysteresis loop area controlling parameters under positive and negative bias, respectively. $\chi$ is the magnitude of ideal diode behaviour and $\gamma$ is the diode parameter like thermal voltage and ideality factor, as explained in Table 5.1.

$$f(w) = \log \begin{cases} (1+w)^p, \ 0 \leq w \ \leq 0.1 \\ (1.1)^p, \ 0.1 < w \ \leq 0.9 \\ (2-w)^p, \ 0.9 < w \ \leq 1 \end{cases} \quad (2)$$

$$\frac{dw}{dt} = A \times v_i^m(t) \times f(w) \quad (3)$$

The MCA-based model that was developed demonstrates a range of synaptic functions such as learning, forgetting, and synaptic plasticity. The design of the analytical model [114] is based on the memristive device that was experimentally developed and has been successful in emulating various RRAM and synaptic characteristics.

## 5.3. Results and Discussions

### 5.3.1. 2D FBSE-EWT Image Decomposition Techniques

In this work, an advanced approach is proposed using FBSE-based spectrum instead of FT based spectrum for improved segmentation and boundary identification [112, 113]. The method introduces a 2D FBSE-EWT with MCA-based model, incorporating multi-frequency scales for boundary detection. The proposed methods are then applied to fundus image decomposition and classification for glaucoma disease detection and diagnosis. As illustrated in Fig. 5.4 (a) and (b), 2D FBSE-EWT is particularly well-suited for non-stationary signals as it employs non-stationary Bessel functions as a basis set represented as Bessel 0 and Bessel 1 of order 0 and order 1, respectively. Unlike the FT, FBSE exclusively represents real signals with positive frequencies as shown in Fig. 5.4 (a) and (b), simplifying the application of filter-based decomposition techniques and reducing distortion. Furthermore, 2D FBSE-EWT generates unique coefficients of the same length as the original signal, providing twice the frequency resolution compared to FT. These unique characteristics make 2D FBSE-EWT a compact representation option for wide-band signals, capitalizing on the non-stationary characteristics and amplitude modulation of Bessel functions, which can be advantageous for various applications [23, 24, 105].

Deep learning technologies currently rely on CMOS circuits, which suffer from drawbacks such as high computation operations, area consumption, energy consumption, processing time, and power consumption [46] compared to the MCA-based model. To overcome these limitations, MCA-based model offers a promising solution by significantly reducing power consumption compared to conventional CMOS-based systems [13]. The adoption of MCA-based model has gained power in image processing domains, including pattern recognition and edge detection, due to its advantages as mentioned above.

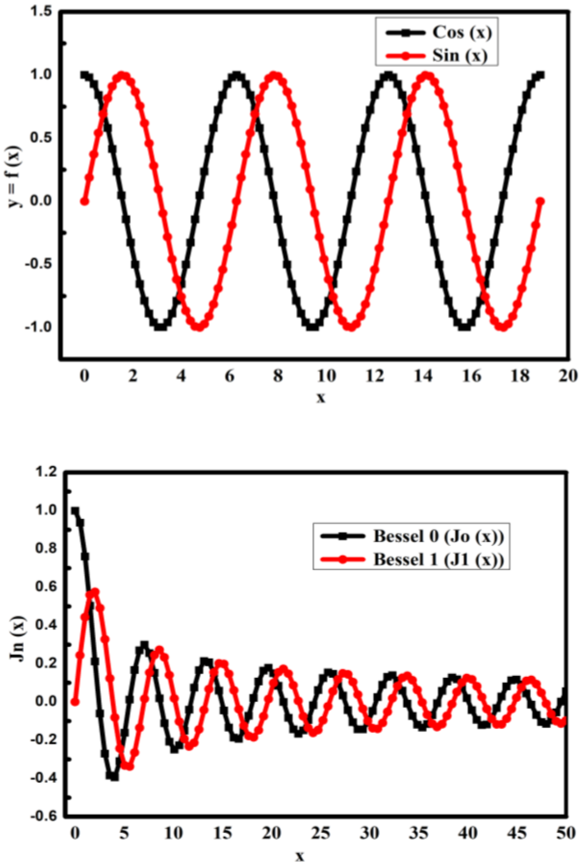


Figure 5.4: Plot of basis functions using (a) sin and cosine for the Fourier transform representation (b) Bessel functions of order-zero and order-one for FBSE.

The datasets (rim-one r1, rim-one r2, and rim-one r3) employed in this work for glaucoma detection comprise 325 fundus images in the glaucoma class and 458 fundus images in the normal class [23]. In addition, augmentation techniques are also employed to further improve the accuracy. The 2D FBSE-EWT method enhances the analysis of non-stationary signals by using non-stationary Bessel functions as its foundation.

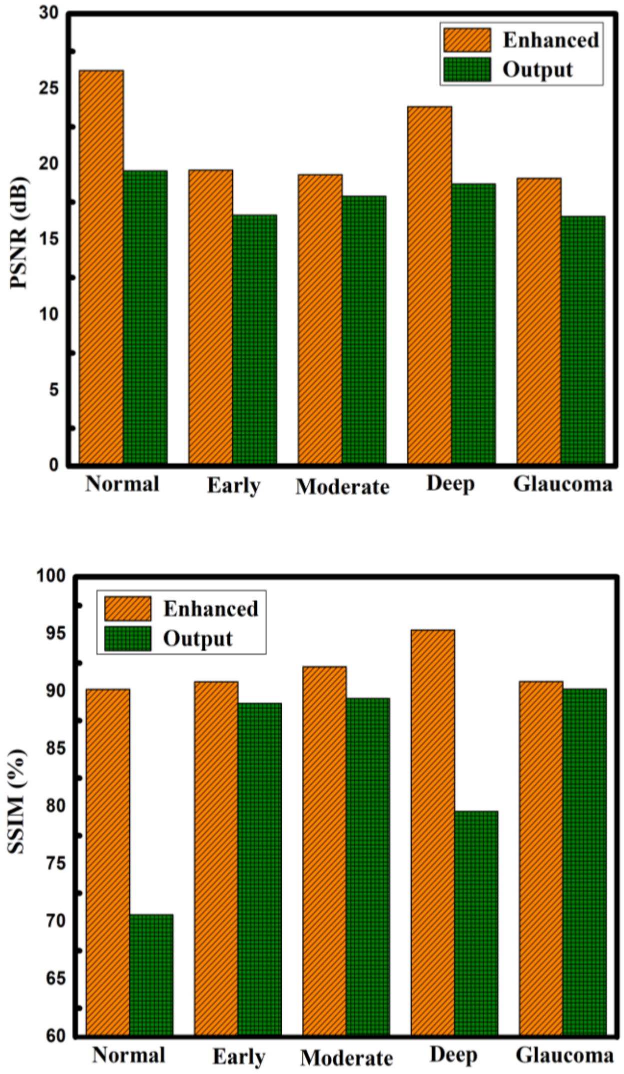


Figure 5.5: Image assessment quality parameter in terms of (a) PSNR for output images and enhances output images, and (b) SSIM for output images and enhances images

2D FBSE-EWT stands out because it customizes its coefficients based on the signal's length, giving it double the frequency detail compared to FT. This is useful for handling wide-band signals effectively. In image processing, FT has drawbacks like wider bandwidth, slower processing, and lower resolution. On the other hand, 2D FBSE-EWT, with its unique coefficients, offers a narrower bandwidth, faster processing, and higher resolution. MCA-based model has emerged as a promising technology for image classification tasks due to their unique properties and benefits. A memristor is a two-terminal passive electronic device that exhibits a resistance change in response to the applied voltage. When integrated into crossbar arrays, MCA can store and process large amounts of data in a highly parallel and energy-efficient manner. Here is a comprehensive explanation of the utilization of MCA-based models in image classification, covering all the benefits associated with memristors, parallel processing. MCA-based model enables massive parallelism in image classification tasks as shown in Fig. 5.5.

In this study, authors have concentrated on an integrated approach combining 2D FBSE-EWT and MCA-based models to enhance the quality of reconstructed output images (O). During the reconstruction phase, one optimized each pixel by boosting its quality by a factor of 1.65 times its original value, resulting in an improved quality of enhanced image (E). To assess the quality of both images, ‘O’ and ‘E,’ one can employed PSNR in decibels (dB) and the SSIM in percentage (%). In Table 4.2, authors analysed images at various stages, ranging from normal to glaucoma, to evaluate the impact of the proposed model, this analysis included early moderate, and deep stages of fundus images. These findings confirm that the enhancement at each disease stage results in higher-quality images, facilitating the early detection of the disease. The measured values of PSNR were 26.2346 dB, and SSIM was 95.38%, representing the highest performance within the normal and deep classes of fundus images, as detailed in Table 5.2.

In Table 5.3, highlights the contrast between proposed approach and various previously reported technologies for fundus image enhancement, which tend to yield lower PSNR and SSIM values, indicative of image quality. In contrast to these earlier approaches, one has opted not to employ filters, GAN and generators, as seen in other reported technologies [117, 118, 119, 120-125]. The proposed integrated model, combining 2D FBSE-EWT and MCA-based model, provides an efficient means for early disease detection and diagnosis. Significantly, this proposed technology surpasses the performance of other reported methods, as evidenced in Table 5.3.

### 5.3.2. Image Classification using CNN with MCA based Model

Physical significance of each memristor within the crossbar array can represent a connection weight or synaptic strength between two neurons. The parallel architecture allows for simultaneous computations on the multiple data points, resulting in significantly faster processing times compared to traditional sequential computing architectures. Integration of MCA-based model provides high device density, allowing for the integration of many memristors in a small physical footprint. High density is crucial in image classification, where huge datasets and CNN models require a significant number of connections [114, 126-130]. The compactness of the crossbar array leads to reduced interconnect lengths and minimized signal propagation delays, enabling efficient and rapid data processing. Low power consumption in memristors is inherent non-volatile properties, meaning they retain their resistance state even after the power is removed. This characteristic eliminates the need for constant power supply to maintain data integrity, resulting in lower power consumption compared to volatile memory technologies. By leveraging this feature, MCA-based model can achieve energy-efficient image classification, making them suitable for resource constrained applications.

TABLE 5.2: COMPARATIVE ANALYSIS OF RECONSTRUCTED FUNDUS IMAGE QUALITY

| Technology | SNR (dB) | SSIM (%) | Ref. |
|---|---|---|---|
| Wiener Filter + CLAHE | 20.50 | 0.3164 | [128] |
| Average Filter + CLAHE | 20.96 | 0.4890 | |
| Gaussian Filter + CLAHE | 20.61 | 0.2095 | |
| GAN | 20.94 | 0.7990 | [124] |
| WGAN | 20.83 | 0.7874 | |
| WIN5-RB | 22.70 | 0.5600 | [118] |
| Cycle-GAN | 21.94 | 0.8774 | [117] |
| U-net generator | 23.37 | 0.8941 | [119] |

| | | | |
|---|---|---|---|
| 4×4 U-Net | 18.80 | 0.4400 | [125] |
| **2D FBSE-EWT + MCA Model** | **26.23** | **0.9021** | **Our Work** |

TABLE 5.3: IMPROVED ASSESSMENT PERSENTAGE WITH BRIGHTNESS EFFECT

| **Image** | **PSNR Improved (in %)** | **SSIM Improved (in %)** |
|---|---|---|
| Normal | 34.00 | 27.72 |
| Early | 17.94 | 2.11 |
| Moderate | 8.00 | 3.08 |
| Deep | 15.17 | 19.79 |
| Glaucoma | 27.36 | 0.71 |

High speed MCA-based model offers fast read and write operations due to the inherent properties of memristors. Table 5.3 illustrates the enhanced quality of the reconstructed output image in terms of a percentage. The most substantial enhancement is evident in the normal class when compared to the other classes, namely early, moderate, deep, and glaucoma. This can be attributed to the fact that the images texture aligns well with the proposed methodology for decomposition and enhancement techniques. However, it is worth noting that enhancements are also noticeable in each class of images, underscoring the effectiveness of the proposed techniques in improving all categories of fundus images for the early detection of disease. Fig. 5.5 (a) and (b) depict a graphical representation of the measurement of image assessment parameters. This graphical presentation aids in comprehending the impact of varying brightness levels on the reconstructed images across five distinct image classes: normal, early, moderate, deep, and glaucoma.

The resistance states of the memristors can be rapidly read to retrieve stored weights, and the resistive changes can be efficiently programmed to update synaptic strengths during the training process. The combination of parallel processing and high-speed operations contributes to accelerated image classification tasks, enabling real-time performance. MCA-based model is highly scalable, allowing for the construction of large-scale neural network models. As the demand for more complex and accurate image classification systems increases, the ability to scale up the computational capacity becomes crucial. The images retrieved from the MCA-based model are then used to train the CNN models. The parameters used for performance evaluation in this application are accuracy, sensitivity, specificity, and precision [23], which are defined by equations (4), (5), (6), and (7), respectively.

In the equations (4), (5), (6), and (7), NTP, NTN, NFP, and NFN represent the number of true positives, the number of true negatives, the number of false positives, and the number of false negatives, respectively. Fault tolerance of MCA-based model exhibit fault-tolerant behaviour due to their distributed computing nature. The parallel processing and distributed storage of information across the MCA-based model make it strong to individual memristor failures. Even if a few memristors within the array become faulty, the overall performance of the system remains relatively unaffected, ensuring robust and reliable image classification.

The utilization of MCA-based model in image classification offers numerous benefits, including parallel processing, dense integration, low power consumption, high speed, scalability, adaptability, and fault tolerance. These advantages make proposed MCA-based model, a promising technology for efficient and high-performance image classification systems, opening new possibilities for advancements in the field of artificial intelligence and machine learning. The conducted comparative analysis of glaucoma detection image classification results using EfficientNetb0 against other reported findings, as detailed in Table 5.3.

These results outperformed the reported ones, primarily due to the utilization of a complete dataset processed through the proposed integrated model combining 2D FBSE-EWT and MCA-based model. The evaluation involved additional classifiers, including ResNet 18, ResNet 50, and AlexNet, as illustrated in Fig. 5.6, with EfficientNetb0 emerging as the top-performing model due to its compatibility with the internal architecture of processed images in proposed methodology. The attempted image classification on the unprocessed dataset, one observed significantly lower accuracy compared to the processed data, with an improvement of 32.14% in accuracy and 40.93% in sensitivity, as demonstrated in Table 5.4.

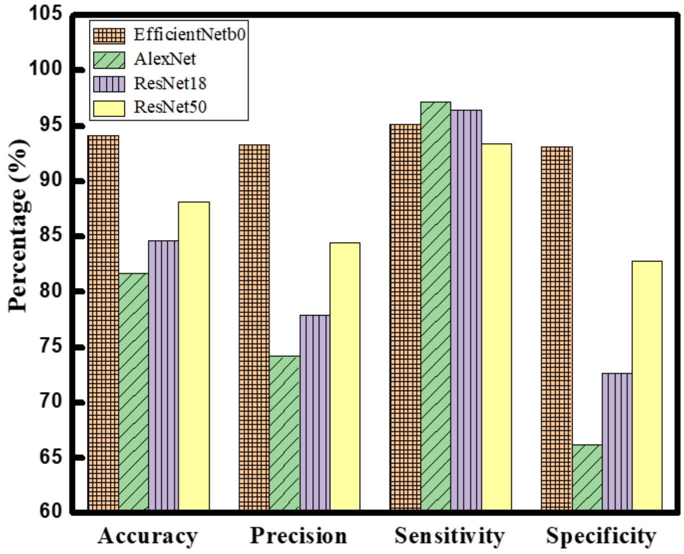


Figure 5.6: Image classification using CNN and memristor model.

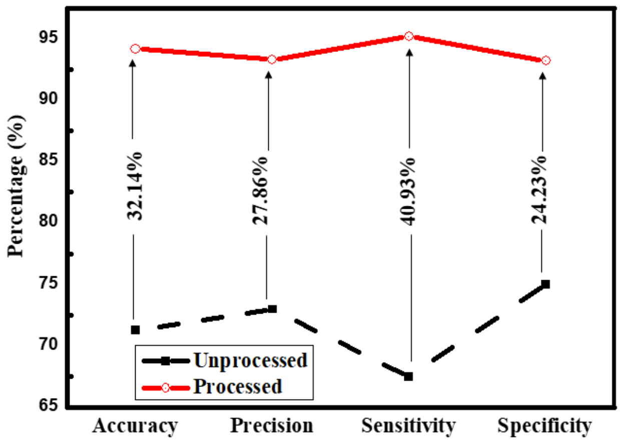


Figure 5.7: Image classification comparison of processed and unprocessed image.

TABLE 5.4: COMPARATIVE ANALYSIS OF CLASSIFICATION PERFORMANCE WITH PROCESSED IMAGES

| **Methodology** | **Accuracy (%)** | **Precision (%)** | **Sensitivity (%)** | **Specificity (%)** | **Ref.** |
|---|---|---|---|---|---|
| ResNet50 | 82.77 | - | 86.6 | 77.91 | |
| MLP Classifier | 75.73 | - | 83.73 | 54.34 | [23] |
| Higher order Spectra (HOS) | 91.00 | - | - | - | [126] |
| PCA-FFT | 80.00 | - | 73.00 | 85.00 | [127] |

| | | | | | |
|---|---|---|---|---|---|
| HOS Cumulant Features | 92.60 | - | 100 | 92.00 | [105] |
| **EfficientNetb0** | **94.15** | **93.30** | **95.13** | **93.17** | **Our Work** |

TABLE 5.5: CALCULATION OF IMPROVED ASSESSMENT PARAMETERS BY USING 2D FBSE-EWT AND MCA-BASED MODEL

| Model | EfficientNetb0 | | |
|---|---|---|---|
| Parameters | With 2D FBSE-EWT + MCA Model | Without 2D FBSE-EWT + MCA Model | Improved Quality (%) |
| Accuracy (%) | **94.15** | **71.25** | **32.14** |
| Precision (%) | **93.30** | **72.97** | **27.86** |
| Sensitivity (%) | **95.13** | **67.50** | **40.93** |
| Specificity (%) | **93.17** | **75.00** | **24.23** |

This enhancement resulting from the application of 2D FBSE-EWT and MCA-based model to the processed dataset, can be visually understood through the graphical representation in Fig. 5.7 and 5.8. As depicted in Table 5.5, the MCA-based model showcases its effectiveness by demonstrating reduced power and energy consumption, minimal area prerequisites, decreased computational complexity, and elevated processing speed. This enhancement resulting from the application of 2D FBSE-EWT and MCA-based model to the processed dataset, can be visually understood through the graphical representation in Fig. 5.7 and 5.8. As depicted in Table 5.6, the MCA-based model showcases its effectiveness by demonstrating reduced power and energy consumption, minimal area prerequisites, decreased computational complexity, and elevated processing speed. These factors collectively play a pivotal role in driving down the overall cost of the devices. Adaptability and learning of the MCA-based model offer inherent adaptability and learning capabilities. The resistance changes in memristors can be dynamically adjusted to adapt new patterns or update synaptic strengths during the learning process as compared to conventional methodology [128, 129]. This adaptability allows the MCA-based model to continuously improve its classification accuracy over time by leveraging the principles of synaptic plasticity and efficient learning algorithms in the healthcare domain.

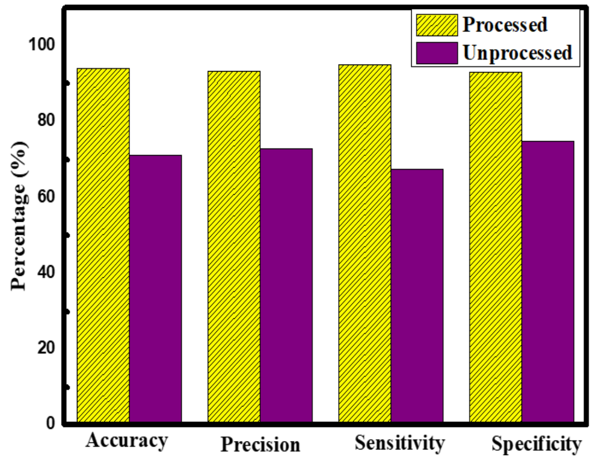


Figure 5.8: Image classification comparison of processed and unprocessed dataset.

TABLE 5.6: COMPARISON OF DIGITAL CMOS WITH MCA-BASED MODEL FOR COMPUTATION OF (256×256) IMAGE BASED DATASET

| **Parameters** | **CMOS** | **MCA Model** | **Prominent Improvement** |
|---|---|---|---|
| **Number of Operations [11, 32]** | $256^3$ + ($256^2$×255) | $256^2$ | **3 × 511 times** |
| **Area(μm$^2$) [32]** | 495452.16 | 10485.76 | **3 × 47.2 times** |
| **Energy Consumption (pJ) [32]** | 1115.4 | 12.88 | **3 × 752 times** |
| **Processing Speed (μs) [11, 32]** | 0.15 | 0.06 | **3 × 2.5 times** |
| **Power Consumption (mW) [11]** | 7436 | 24.733 | **3 × 300 times** |

## 5.4. Conclusion

This study introduces an innovative approach to glaucoma detection and diagnosis by harnessing the power of 2D FBSE-EWT and integrating the MCA-based model. The proposed method combines deep learning with an ensemble technique based on EfficientNetb0, distinguishing between normal fundus images and those exhibiting glaucoma symptoms. In this context, EfficientNetb0 emerges as the optimal choice among CNN models, surpassing ResNet50, AlexNet, and GoogleNet. The evaluation of the reconstructed output images highlights their exceptional quality, evident by significant increase in PSNR and SSIM values, reaching 26.2346 dB and 95.38 %, respectively. The proposed methodology has demonstrated outstanding performance, achieving an impressive accuracy rate of 94.15% when employing EfficientNetb0. Furthermore, a comparative analysis between the dataset processed using the proposed methodology in this work with the unprocessed dataset for image classification, reveals substantial improvements, with accuracy and sensitivity increasing by 32.14% and 40.93%, respectively, in the processed dataset's image classification. Further, the results obtained through the proposed methodology outperforms other reported findings for glaucoma detection and diagnosis, employing the MCA-based model in conjunction with 2D FBSE-EWT. The MCA-based model demonstrates its efficacy through several key advantages, including reduced power and energy consumption, minimal area requirements, lower computational complexity, and enhanced processing speed. These benefits turn into cost savings for the overall devices. Consequently, the proposed methodology holds substantial promise for application in the healthcare domain, particularly in the early identification of diseases.

# Chapter 6

# MCA Model for Early Detection of Various Soybean Diseases Through Leaf Image Analysis

## 6.1. Introduction

Inorganic the early detection of diseases in soybean crops is a critical area of research due to its significant impact on agricultural productivity and economic stability [131-134]. Soybean is a vital crop globally, serving as a key source of protein and oil. However, it is susceptible to a range of diseases that can drastically reduce yield and quality, leading to substantial economic losses for farmers and the agricultural industry [135]. Traditional methods of disease detection often rely on manual inspection, which is time-consuming, labour-intensive, and prone to human error. Furthermore, these methods typically identify diseases only after visible symptoms appear, by which time the infection may have already spread extensively. Research in the domain of early detection of multiple classes of soybean diseases aims to develop advanced, automated systems that can identify diseases at their inception, enabling timely intervention and treatment. Such systems utilize cutting-edge technologies like machine learning, computer vision, and memristive models to analyse leaf images and detect subtle signs of disease that are not easily observable by the naked eye [13]. By accurately classifying various diseases at an early stage, these systems can help mitigate the spread of infections, enhance crop management practices, and improve complete production yield.

## 6.2. Database and Proposed Methodology

The importance of this research extends beyond individual farms, as it contributes to global food security and sustainable agricultural practices [136]. With the increasing global population and the demand for higher food production, innovative solutions for early disease detection are essential. This research not only provides immediate benefits to soybean farmers but also sets a precedent for the application of advanced technologies in agriculture, paving the way for smarter and more efficient farming practices [137]. Soybean ranks as the fifth most cultivated crop in India, playing a vital role in food security, animal feed, and edible oil production. It significantly contributes to farmers agricultural income and the national economy. With growing demand driven by population growth and shifting dietary preferences, timely interventions, cost reduction, and quality improvements are essential for sustaining and enhancing production.

A memristive model-based framework, characterized by lower power consumption compared to CMOS based systems, has the potential to scale these technological constraints. When it comes to tasks like pattern processing, the memristive model shows better processing speed and energy efficiency than Von Neumann circuits especially when applied to neural networks [134]. Extensive research has been conducted on utilizing memristor based architectures for various applications, including neuromorphic computing particularly in neural network applications. The memristive model can function as a vector matrix multiplication, that eliminates the necessity for transferring large amounts of neural weights data, making them highly compatible substitutes for CMOS based neural networks [46]. To address the limitations of previous studies, this research aims to utilized WPT for image decomposition and utilize the memristive model to conduct mathematical research for further applications in image decomposition and classification as shown in Fig. 6.1. The processed images are utilized for computational diagnosis and early disease detection of soybean crop for multiclass. MCA inspired system has an advantage in image processing due to their simultaneous storage and processing capabilities, non-volatile memory, and adaptability [86]. This offers the potential for the development of more efficient and intelligent systems in image processing applications with cost effectiveness. The key benefits of using MCA inspired system in computational tasks include high density, low power consumption, and the ability to perform parallel computations, making them ideal for implementing neural networks. The dataset was collected from soybean fields in Simrol, Indore, Madhya Pradesh, and subsequently verified by a pathologist at ICAR Bhopal. The gathered image dataset was processed for image decomposition using WPT, with the resulting coefficients handled by a graph theory-inspired system. The reconstructed images were then compiled as a processed dataset, considered as a synthetic dataset for further analysis in image classification using a CNN model [13, 138-147]. During the classification process, faulty images were identified, and image augmentation techniques were applied to enhance the device's accuracy.

## 6.3. Results and Discussions

In this proposed work, a graph theory-inspired system combined with the WPT for image decomposition and pre-trained CNN models has been utilized to diagnose multiclass soybean leaf diseases and other infectious conditions [141]. The study focuses on a multiclass dataset comprising 11 distinct categories of soybean leaf images, as detailed in Table 6.1.

These categories include downy mildew, sudden death syndrome, powdery mildew, target leaf spot, bacterial pustule, anthracnose, rhizoctonia aerial blight, frogeye leaf spot, yellow mosaic virus, soybean mosaic virus, and healthy leaves [135]. The images were collected from fields and verified by scientists from CSIR-ICAR Bhopal. Leveraging image processing techniques and machine learning algorithms, healthy soybean leaf images are used for diagnosing these diseases, as illustrated in Fig. 6.1. Numerous models have been proposed globally to utilize soybean leaf images for the early-stage detection of multiclass diseases [139].

TABLE 6.1: DATASET DETAILS OF MULTIPLE CLASS

| Different Class of Soybean Leaf | Suggested Dataset | Improved Dataset |
|---|---|---|
| Downy Mildew | 94 | 818 |
| Sudden Death Syndrome | 93 | 647 |
| Powdery Mildew | 103 | 1027 |
| Target Leaf Spot | 113 | 419 |
| Bacterial Pustule | 92 | 532 |
| Anthracnose | 111 | 418 |
| Rhizoctonia Aerial Blight | 92 | 1027 |
| Frogeye Leaf Spot | 213 | 61 |
| Yellow Mosaic Virus | 82 | 82 |
| Soybean Mosaic Virus | 86 | 86 |
| Healthy | 983 | 893 |

In image processing, our proposed work utilizes WPT for image pre-processing, which is a more generalized approach compared to the traditional wavelet transform.

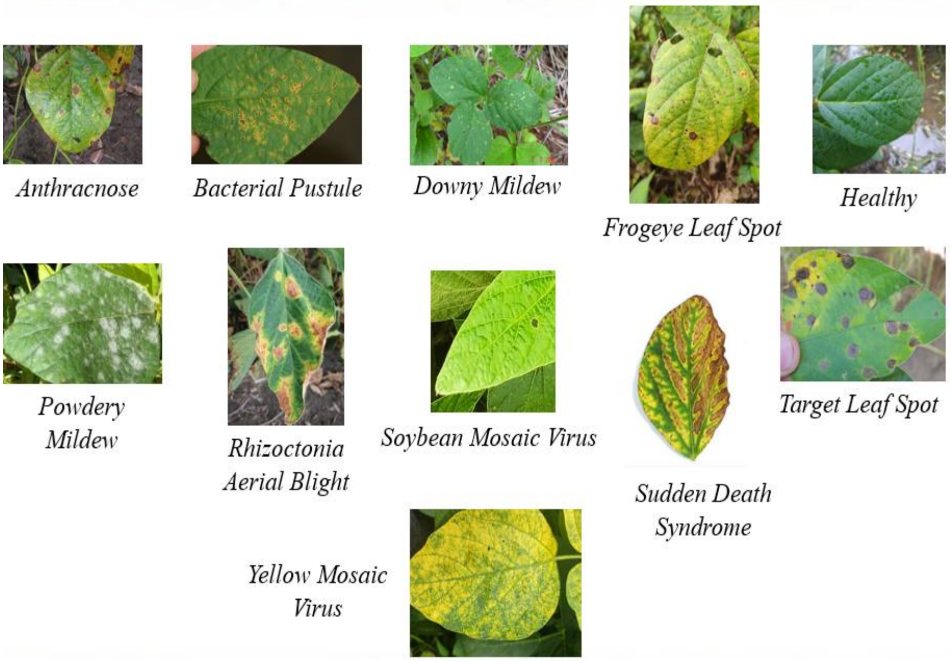


Figure 6.1 Automated classification of soybean leaf images for diagnosing multiple crop diseases.

While the wavelet transform provides flexible time-frequency resolution, it has limitations, particularly in the high-frequency domain, where it exhibits low-frequency resolution, making it difficult to distinguish between signals with closely spaced high-frequency components. Wavelet packets extend the traditional wavelet bases by forming linear combinations of standard wavelet functions. These extended bases inherit properties like orthonormality and time-frequency localization from their associated wavelet functions. The wave decomposition vectors generated through this image decomposition technique can be used as input signals in the graph theory-based model for image compression and encryption.

### 6.3.1. Techniques for image decomposition using WPT via MCA model

During acquisition, compression, and transmission processes, images often become contaminated by noise, leading to distortion and loss of information [59-61]. Wavelet analysis has become a preferred method for decomposition in various applications due to its use of different basis functions through distinct mother wavelets [42, 43, 148]. The analytical model discussed here offers advantages over conventional application-specific integrated circuit (ASIC) technologies, particularly in storing compressed images with lower power consumption and in a more compact area [5]. The proposed graph theory-based model is integrated with the WPT to develop an image compression algorithm. In this approach, the decomposed image coefficients obtained from the wavelet packet transform are stored in the graph theory model by mapping the coefficient values to appropriate voltage levels. As illustrated in Fig. 6.2, these mapped voltages are applied to the crossbar array along the rows, and the column currents are collected to reconstruct the images. The collected values are subsequently used to carry out the inverse wavelet transform operation. Following this, an analytical framework is employed to develop a computational strategy based on memristive systems, aimed at efficiently storing the decomposed images. The various images of multiclass soybean leaves targeted for early disease detection in the proposed work.

The memristive model is comparable to the human brain, featuring a 3D structure that offers exceptional downscaling capabilities at the nanoscale. This enables efficient image processing with ultra-fast switching speeds, high-density storage, and extended operational cycles [74, 75]. A key aspect of learning in the human brain is the ability to adjust synaptic weights, a capability that can be replicated in a neuromorphic memristive model for pattern recognition in both images and speech [74]. Memristor-based systems are particularly well-suited for in-memory computing and the development of computing architectures for applications using memristor-based neural networks. These systems offer benefits such as non-volatility, power efficiency, and nanoscale dimensions, all of which contribute to lower device costs [5, 134]. The model being utilized incorporates experimental findings from memristive systems, which are employed to validate the analytical model [74] to create a neuromorphic memristive model. In addition to the complex analytical model, the synaptic learning of $Y_2O_3$-based devices is also described in the nonlinear model. Equations (1), represent the analytical framework for the research presented in this proposed methodology. The memristive device have flux controlled nature is represented by the first term on the right side of the I-V relationship in equation (1).

$$I(t) = \begin{cases} b_1 w^{a_1}\left(e^{\alpha_1 v_i(t)} - 1\right) + \chi\left(e^{\gamma v_i(t)} - 1\right), v_i(t) \geq 0 \\ b_2 w^{a_2}\left(e^{\alpha_2 v_i(t)} - 1\right) + \chi\left(e^{\gamma v_i(t)} - 1\right), v_i(t) < 0 \end{cases} \quad (1)$$

The physical significance of parameters used in memristive model are described as, $b1$ and $b_2$ are experimental fitting parameters. $a_1$ and $a_2$ represent degrees of influence of the state variable under positive and negative bias, respectively. $\alpha_1$ and $\alpha_2$ denoted the hysteresis loop area controlling parameters under positive and negative bias, respectively. $\chi$ is the magnitude of ideal diode behaviour and $\gamma$ is the diode parameter like thermal voltage and ideality factor. The memristive model that was developed demonstrates a range of synaptic functions such as learning, forgetting, and synaptic plasticity. The analytical model is crafted upon the crossbar architecture, which has been experimentally devised and proven effective in mimicking diverse RRAM and synaptic characteristics [74, 134]. In this proposed study, pre-trained CNN models from MATLAB version R2021a are employed to automatically classify early detection of disease in soybean crops.

| TRUE CLASS \ PREDICTED CLASS | Anthracnose | Bacterial Pustule | Downy mildew | Frogeye Leaf Spot | Healthy | Powdery Mildew | Rhizoctonia Aerial Blight | Soyabean Mosaic Virus | Sudden Death Syndrome | Target Leaf Spot | Yellow Mosaic Virus |
|---|---|---|---|---|---|---|---|---|---|---|---|
| Anthracnose | 290 | 0 | 2 | 0 | 0 | 0 | 0 | 0 | 0 | 0 | 0 |
| Bacterial Pustule | 1 | 288 | 0 | 0 | 0 | 0 | 1 | 0 | 0 | 0 | 2 |
| Downy mildew | 8 | 11 | 263 | 0 | 0 | 4 | 0 | 2 | 2 | 0 | 2 |
| Frogeye Leaf Spot | 27 | 4 | 9 | 240 | 0 | 0 | 0 | 0 | 9 | 2 | 1 |
| Healthy | 0 | 0 | 4 | 0 | 287 | 0 | 0 | 1 | 0 | 0 | 0 |
| Powdery Mildew | 0 | 0 | 19 | 0 | 3 | 270 | 0 | 0 | 0 | 0 | 0 |
| Rhizoctonia Aerial Blight | 10 | 0 | 0 | 0 | 2 | 2 | 275 | 0 | 3 | 0 | 0 |
| Soyabean Mosaic Virus | 3 | 0 | 12 | 0 | 4 | 0 | 0 | 273 | 0 | 0 | 0 |
| Sudden Death Syndrome | 0 | 0 | 0 | 0 | 0 | 0 | 0 | 0 | 290 | 0 | 2 |
| Target Leaf Spot | 12 | 0 | 0 | 4 | 0 | 0 | 0 | 0 | 5 | 310 | 0 |
| Yellow Mosaic Virus | 1 | 0 | 4 | 0 | 1 | 0 | 0 | 0 | 1 | 2 | 282 |

Figure 6.2. Automated multiclass classification for the early detection of soybean diseases.

To assess the quality of both the input and decomposed reconstructed output images, image augmentation techniques are employed to enhance the accuracy of classifying 11 distinct classes of soybean leaf images, thereby improving the overall performance of the classification model, as illustrated in the confusion matrix in Fig. 6.2.

### 6.3.2. Multiclass Soybean Leaf disease detection using CNN

The resulting images from the memristive model are utilized for training the CNN models. Performance assessment in this context relies on accuracy (Acc), precision (Pre) [77], sensitivity (Sen), and specificity (Spe), defined by equations (2), (3), (4), and (5), respectively, as shown in Table 6.2. The equations utilize NTP, NTN, NFP, and NFN to represent the counts of true positives, true negatives, false positives, and false negatives, respectively, for two distinct classes.

$$Accuracy = \frac{NTP+NTN}{NTP+NFP+NTN+NFN} \quad (2)$$

$$Precision = \frac{NTP}{NFP+NTP} \quad (3)$$

$$Sensitivity = \frac{NTP}{NFN+NTP} \quad (4)$$

$$Specificity = \frac{NTN}{NFP+NTN} \quad (5)$$

The suggested approach utilizes a 30% training and 70% testing division of the dataset to assess the classification model. Earlier studies conducted by Halawani *et al.* and Khalid *et al.* have showcased the efficiency of memristive model in image processing and digital logic circuits. These models exhibit a decrease in device count and operations when compared to traditional CMOS-based models [29, 30]. To evaluate the compression effectiveness of the memristive model integrated with the WPT model relative to traditional CMOS based models, the authors conducted an extensive analysis using a (512×512) image. The comparison involved employing parameter values derived from sources [29, 30, 134], as detailed in Table 6.3. The proposed AlexNet exhibits remarkable performance in classifying images within the small dataset, achieving Acc, Pre, Spe, and Sen values of 94.30%, 99.66%, 100.00%, and 99.65%, respectively, as detailed in Table 6.2.

TABLE 6.2
IMAGE CLASSIFICATION USING EFFICIENTNET MODELS

| **CNN Model** | **EFFICIENTNET** | |
|---|---|---|
| **Assessment Percentage (%)** | **Unprocessed** | **Processed** |
| **Accuracy (Acc)** | 70.42 | 94.30 |
| **Precision (Pre)** | 65.93 | 99.66 |
| **Sensitivity (Sen)** | 41.96 | 100.00 |
| **Specificity (Spe)** | 89.24 | 99.65 |

TABLE 6.3
EVALUATING THE EFFECTIVENESS OF THE PROPOSED METHOD IN IDENTIFYING DISEASE THROUGH THE COMPARISON OF ITS PERFORMANCE WITH OTHER EXISTING METHODS USING MULTICLASS IMAGE

DATABASE

| Small Dataset | | | | |
|---|---|---|---|---|
| **Ref.** | **Acc (%)** | **Pre (%)** | **Recall (%)** | **F1-score** |
| Shrivastava Hooda *et al.* [136] | 60.24 | 58 | 60.35 | 59.7 |
| Dandawate *et al.* [137] | 93.79 | -- | -- | -- |
| Kaur *et al.* [138] | 68.9 | 70 | 71 | 70.53 |
| Simonyan and Zisserman [139] | 89 | 86 | 79 | 78 |
| Gharge *et al.* [140] | **70-100** | -- | -- | -- |
| Szegedy *et al.* [141] | 39 | 44 | 35 | 35 |
| Huang *et al.* [142] | **98.14** | 54 | 48 | 49 |
| Chollet *et al.* [143] | 59 | 74 | 54 | 52 |
| LeCun *et al.* [144] | 48 | 65 | 45 | 35 |
| He *et al.* [145] | 79 | 69 | 75 | 74 |
| Karlekar *et al.* [146] | **98.14** | **97** | **97** | **97** |
| Sukhvir *et al.* [147] | 77-79.9 | -- | -- | -- |
| **Proposed Work** | **94.30** | **99.69** | **100.00** | **99.84** |

TABLE 6.4
CMOS AND MEMRISTIVE COMPUTATIONAL COMPARISON

| **Parameters** | **CMOS** | **Memristive model** | **Prominent Improvement for '*N*' Number of Image** |
|---|---|---|---|
| Number of Operations [23, 24] | $512^3 + (512^2 \times 511)$ | $512^2$ | ($N$ ×1023) times |
| Area ($\mu m^2$) [24] | 1585446.912 | 41943.04 | ($N$ × 37.8) times |
| Energy Consumption (pJ) [24] | 1115.4 | 1.484 | ($N$ × 752) times |
| Processing Time (µs) [23, 24] | 0.15 | 0.06 | ($N$ × 2.5) times |

In contrast, other reported CNN models, as shown in Table 6.3 [13, 31, 78], present lower assessment parameter values for multiclass datasets. A comprehensive comparative analysis with existing literature highlights that conventional technologies consistently exhibit lower values in terms of Acc, Pre, Spe, and Sen for both small and large datasets [8, 34, 42, 59, 60, 61, 80, 86, 89, 146, 147-151]. While some CNN models may demonstrate superior performance compared to our proposed method in terms of Acc and Sen, it is crucial to acknowledge that commercially viable image classification technologies typically meet issues such as higher computational demands, increased area and energy consumption, and longer processing times due to their dependence on CMOS systems [29, 30].

### 6.3.3 Mobile Applications

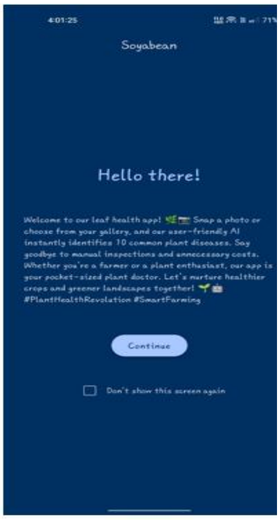

Welcome Screen

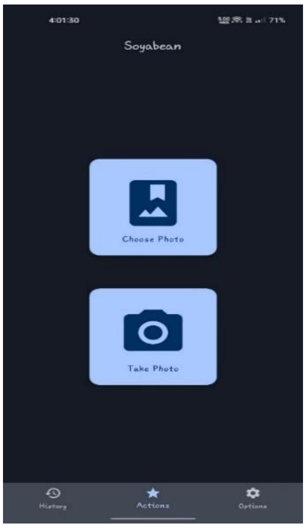

Actions Screen

Options Screen

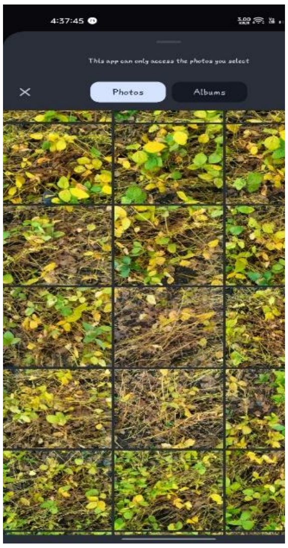

Gallery Screen

Capture Screen

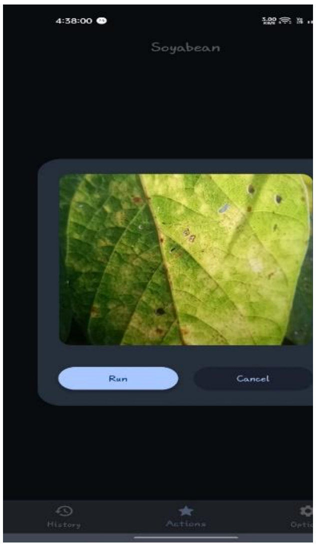

Run Screen

Result Screen

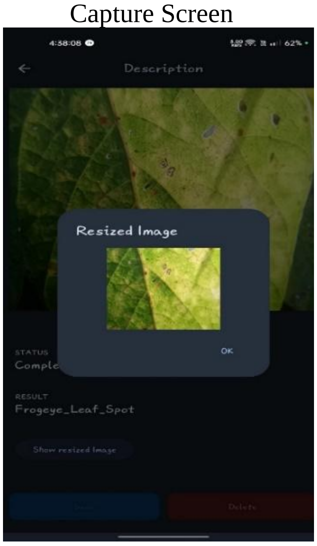

Resized Screen

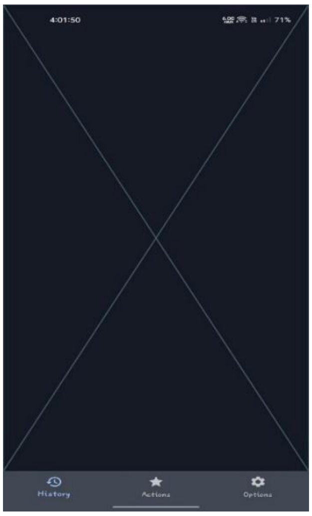

History Screen

Figure 6.3: IoT enabled Mobile application for early detection of disease.

However, these challenges can be effectively addressed by integrating memristive systems [29, 30, 134]. By using memristive systems, one can reduce the problems linked with traditional CMOS based methods, leading to better and more efficient ways of classifying images. This is reflected in the comparative results presented in Table 6.4. Memristive model addresses these technological limitations by significantly reducing total energy consumption, computational operations, area consumption, processing time, and power consumption compared to conventional systems as shown in Table 6.4 [29, 30]. This not only helps overcome Von Neumann bottleneck issues but also presents a more cost-effective solution for image classification systems. It is noteworthy that AlexNet demonstrated a particularly high Acc, especially for smaller datasets, as illustrated in Fig. 6.3 because of internal architecture compatibility with proposed classification. This superiority is attributed to the internal architecture compatibility of AlexNet with proposed memristive model framework, facilitating effective image decomposition and classification [146, 147].

The Internet of Things (IoT) is expanding rapidly, with billions of interconnected devices generating and processing vast amounts of data, as illustrated in Table 6.4 [43, 57, 58, 148, 149, 150, 151]. However, limitations in communication bandwidth and storage present significant challenges. The MCA based model framework addresses these issues by offering a revolutionary solution that not only increases processing speed but also significantly reduces the compression ratio required for data transmission and image processing within IoT networks [152-154]. MCA based models dramatically accelerate processing times compared to traditional digital systems, enabling faster diagnoses while also being highly scalable, allowing for the implementation of larger and more complex CNN models. Their analogy nature reduces energy consumption, making them ideal for resource-constrained environments like portable diagnostic devices. Future research could focus on improving the precision and robustness of MCA based model, developing more advanced CNN architectures for disease detection, and exploring the integration of this technology into clinical practice for broader use in medical diagnostics [21, 47].

## 6.4. Conclusion

Early detection of multiclass diseases in soybean crops is essential for enhancing yields and minimizing economic losses. This study introduces an innovative approach that combines a graph theory-based model with machine learning to analyse leaf images for early disease identification. By leveraging the unique capabilities of graph theory for efficient data processing, the system incorporates a piecewise window function to maintain stability and accuracy in state variables during training. High-resolution images of soybean leaves undergo preprocessing before being input into a CNN specifically designed to classify multiple diseases. The graph theory-based model improves CNN performance by optimizing the learning process and addressing challenges like vanishing gradients. Experimental results indicate that the system can accurately classify various soybean leaf diseases with a 94.3% accuracy rate. This approach highlights the potential of graph theory models in agricultural applications, providing a robust, scalable solution for real-time disease monitoring and supporting sustainable farming practices. Future research will focus on integrating this model with IoT devices for continuous field monitoring and refining classification algorithms further.

# Chapter 7

# Conclusion and Future Scope

## 7.1. Conclusions

This thesis has focused on the utilization of developed $Y_2O_3$-based MCA using a DIBS system-based model for image processing. Experimental results obtained from the fabricated MCA device were validated with an analytical MCA-based model, showing a strong agreement with the experimental data, and forming a robust foundation for applications in biomedical imaging. One of the primary applications of the validated MCA model was in biomedical image processing, specifically for computed tomography (CT) and magnetic resonance imaging (MRI) analysis. Using a two-dimensional image decomposition technique, we employed various levels of decomposition and thresholds to assess reconstructed image quality based on metrics like PSNR, SSIM, and MSE. Results demonstrated effective data compression, with MRI and CT scans achieving compression ratios of 21.01% and 47.81% using Haar wavelets and 18.82% and 46.05% with biorthogonal wavelets. Analyzing image brightness further enhanced image quality, showing a 103.72% improvement for CT scans and an 18.59% increase for MRI images using Haar wavelets. These findings support the MCA-based model as a valuable tool for biomedical image compression, enabling reduced computational time and storage requirements. In response to the COVID-19 pandemic, this work applied the MCA model to a two-dimensional TQWT for processing chest X-ray images from two datasets to enable rapid, cost-effective COVID-19 detection. TQWT achieved optimal PSNR and SSIM values with a $Q$ of 4, $r$ of 3, and $J$ of 2. The processed images were then classified using ResNet50 and AlexNet CNNs, achieving average accuracies of 98.82% and 94.64% on smaller and larger datasets, respectively, outperforming conventional deep learning approaches. This MCA model-based approach demonstrated substantial benefits over CMOS technology in accuracy, power efficiency, area savings, and cost-effectiveness for COVID-19 detection. The study further applied the MCA model to detect lung diseases like pneumonia using chest X-ray datasets. By employing the TQWT and MCA-based model, this work achieved an average classification accuracy of 99.24% with the EfficientNet CNN, marking an advancement in efficiency and accuracy over traditional methods. Additionally, a novel $Y_2O_3$-MCA-based activation function showed a classification efficiency of 99.94%, surpassing the conventional sigmoid function and optimizing deep learning applications. Other applications explored in this thesis include digit recognition and glaucoma detection. For digit recognition, a CNN with ReLU activation was used on the MNIST dataset, demonstrating efficient feature extraction and storage capabilities using the memristive system. In glaucoma detection, the MCA model, integrated with 2D FBSE-EWT and the EfficientNet CNN, achieved a PSNR of 26.23 dB and an SSIM of 95.38%, reaching a glaucoma classification accuracy of 94.15%. The model's capabilities were also extended to agriculture, classifying soybean leaf diseases with a 94.3% accuracy, supporting real-time, scalable, and sustainable solutions for agricultural disease monitoring.

The $Y_2O_3$-based MCA model offers a versatile and high-performance approach to applications in biomedical imaging, disease diagnosis, and agricultural analysis. Its capabilities in image compression, classification accuracy, and energy efficiency underscore the potential of memristive systems for addressing complex challenges in cost-sensitive and data-intensive fields. Future research directions will explore integrating the MCA model with IoT technologies for continuous monitoring in healthcare and agriculture, allowing real-time data acquisition and processing. Further enhancements will focus on refining classification algorithms for improved accuracy and robustness, making the system adaptable to broader applications in machine learning and deep learning.

## 7.2. Future Scope

Advancements in Face Recognition and Biometric Systems: The memristive model's inherent capabilities in parallel computing and energy efficiency present significant potential to enhance face recognition and other biometric systems. Integrating memristive technology in these applications could enable faster, more efficient data processing while reducing power consumption, thereby improving the accuracy and reliability of pattern recognition tasks.

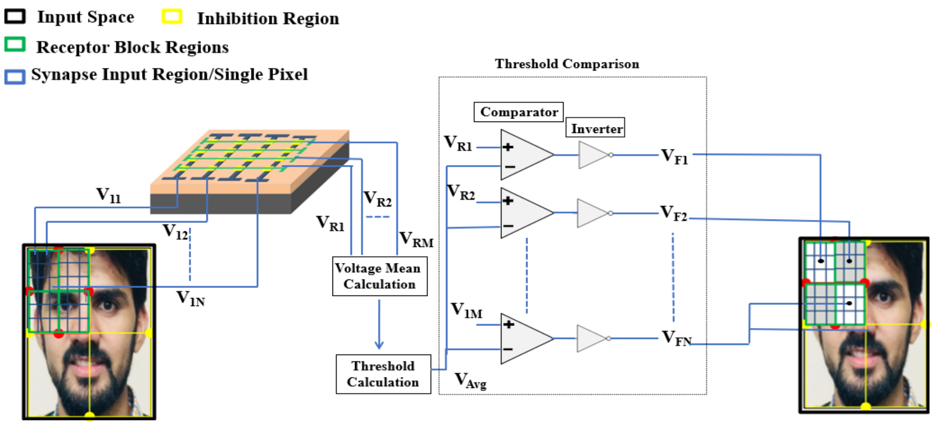


Figure 7.1: Illustrates the design of a memristor-based neural network, applicable across diverse areas such as biometrics, face detection, and human activity recognition.

Development of Edge Devices for Real-Time Processing: Future research could focus on embedding memristive models into edge devices designed for real-time image processing in biometric and healthcare systems. With the increasing demand for low-power and high-speed data processing in these domains, memristive edge devices could deliver high efficiency and responsiveness, making them valuable for on-site, immediate diagnostics and identification.

Enhanced Security in Biometric Systems: Leveraging the adaptable and non-volatile properties of memristive devices, future studies could explore enhanced security features within biometric systems. This approach could significantly strengthen data integrity, ensuring more reliable and faster authentication processes, which is increasingly crucial in security-focused applications.

Optimization for Broader Medical Imaging Applications: The memristive model's methodology can be extended to various medical imaging tasks, such as early cancer detection. Applying the model to cancer diagnostics could aid in early-stage detection, which is vital for improving treatment outcomes, thus broadening the scope and impact of memristive models in healthcare.

Agricultural Disease Monitoring with Mobile Applications: Further enhancement in real-time monitoring and classification of plant diseases can revolutionize precision farming. Future work could focus on deploying the memristive model in mobile applications for agricultural disease diagnosis, allowing for more accurate and timely disease detection. This advancement could directly contribute to sustainable farming practices by optimizing crop yields and reducing losses due to undetected plant diseases

# References


[1] L. Chua, “Memristor-The missing circuit element,” IEEE Transactions on Circuit Theory, vol. 18, no. 5, pp. 507-519, 1971.

[2] Strukov D.B., Snider, G.S., Stewart, D.R. and Williams, R.S., ‘The missing memristor found”, nature, 453(7191), pp.80-83, 2008.

[3] M. Maestro et al, “Experimental verification of memristor-based material implication NAND operation,” IEEE Trans. Emerg. Topics Comput., vol. 7, no. 4, pp. 545-552, Oct. 2017.

[4] M.A. Zidan, J.P. Strachan, and W.D Lu, “The future of electronics based on memristive systems,” Nature Electron., pp. 22–29, 2018.

[5] Y. Halawani, B. Mohammad, M. Al-Qutayri, and S. F. Al-Sarawi, ‘‘Memristor-based hardware accelerator for image compression,’’ IEEE Trans. Very Large Scale Integr. (VLSI) Syst., vol. 26, no. 12, pp. 2749-2758, 2018.

[6] M. Das, A. Kumar, B. Mandal, M. T. Htay, and S. Mukherjee, “Impact of Schottky junctions in the transformation of switching modes in amorphous Y2O3-based memristive system,” J. Phys. D: Appl. Phys., 51, p. 315102, 2018.

[7] C. Li et al, “Analogue signal and image processing with large memristor crossbars,” Nature Electron., pp. 52–59, 2018.

[8] S. Kumar, R. Agarwal, M. Das, P. Kumar, and S. Mukherjee, “Analytical modeling of Y2O3-based memristive system for synaptic applications,” J. Phys. D: Appl. Phys., 53, p. 305101 (6pp), 2020.

[9] D. J. Mannion, A. Mehonic, W.H. Ng, and A.J. Kenyon, “Memristor-based edge detection for spike encoded pixels,” Front. Neurosci, vol. 13, pp. 13, Jan. 2020.

[10] R. Zhu, Z. Tang, S. Ye, Q. Huang, L. Guo, and S. Chang, “Memristor-based image enhancement: high efficiency and robustness,” IEEE Trans. Elect. Devices, vol. 68, no. 2, pp. 602-609, 2021.

[11] F. Cai and W. D. Lu, “Feature extraction and analysis using memristor networks,” in Proc. IEEE Int. Symp. Circuits and Syst. (ISCAS), 2018, pp. 1-4.

[12] P. pouyan, E. Amat, and A. Rubio, “Memristive crossbar memory lifetime evaluation and reconfiguration strategies,” IEEE Trans. Emerg. Topics Comput., vol. 6, no. 2, pp. 207-218, 2018.

[13] K. Jyoti, S. Sushma, S. Yadav, P. Kumar, R. B. Pachori, and S. Mukherjee, “Automatic diagnosis of COVID-19 with MCA-inspired TQWT-based classification of chest X-ray images,” Comput. Biol. Med., vol.152, no.106331, 2023.

[14] S. Kumar, M. Das, M. T. Htay, S. Sriram, and S. Mukherjee, “Electroforming-free Y2O3 memristive crossbar array with low variability,” ACS Applied Electronic Materials, 4(6), pp.3080-3087, 2022.

[15] G. Akkad, M. El. Hassan, and R. Ayoubi, “Hardware and software implementation of a stereoscopic image compression

technique for internet connected devices," in Proc. 2017 Int. Sym. Net., Comput. Commun. (ISNCC), Oct. 2017, pp. 1-6.

[16] B. K. Mohanty, A. Mahajan, and P. K. Meher, "Area and power-efficient architecture for high-throughput implementation of lifting 2-D DWT," IEEE Trans. Circuits Syst. II, Exp Briefs, vol. 59, no. 7 pp. 434-438, 2012.

[17] V. Bulsara, S. Bothra, P. Sharma, and K. M. M. Rao, "Low-cost medical image processing system for rural/semi urban healthcare," in Proc. IEEE Rec. Adv. Intelligen Comput. Sys. (RAICS), 2011, pp. 724-728.

[18] I. W. Selesnick, "Wavelet transform with tunable Q-factor," IEEE Trans. Signal Process., vol. 59, no. 8, pp. 3560-3575, Aug. 2011.

[19] X. Ouyang et al., "Dual-Sampling Attention Network for Diagnosis of COVID-19 From Community Acquired Pneumonia," IEEE Trans. Med. Imag., vol. 39, no. 8, pp. 2595-2605, Aug. 2020.

[20] J. Laguarta, F. Hueto, and B. Subirana, "COVID-19 Artificial Intelligence Diagnosis Using Only Cough Recordings," IEEE Open J. Eng. Med. Biol., vol. 1, pp. 275-281, Sep. 2020.

[21] P. K. Chaudhary and R. B. Pachori, "FBSED based automatic diagnosis of COVID-19 using X-ray and CT images," Comput. Biol. Med., Jul. 2021.

[22] A. Qi et al., "Directional mutation and crossover boosted ant colony optimization with application to COVID-19 X-ray image segmentation," Comput Biol Med., vol. 148, Sep. 2022.

[23] P. K. Chaudhary and R. B. Pachori, "Automatic diagnosis of glaucoma using two-dimensional Fourier-Bessel series expansion based empirical wavelet transform," Biomed. Signal Process. Control, vol. 64, Feb. 2021, Art. no. 102237.

[24] L. A. Whitmore, "Understanding and living with glaucoma," Glaucoma Research Foundation, 1999.

[25] T. Kausu, V. P. Gopi, K. A. Wahid, W. Doma, and S. I. Niwas, "Combination of clinical and multiresolution features for glaucoma detection and its classification using fundus images," Biocybern. Biomed. Eng., vol. 38, no. 2, pp. 329-341, 2018.

[26] U. Raghavendra, S. V. Bhandary, A. Gudigar, and U. R. Acharya, "Novel expert system for glaucoma identification using non-parametric spatial envelope energy spectrum with fundus images," Biocybern. Biomed. Eng., vol. 38, no. 1, pp. 170-180, 2018.

[27] Y. Jiang, Y. Li, and H. Zhang, "Hyperspectral Image Classification Based on 3-D Separable ResNet and Transfer Learning," IEEE Geosci. Remote Sens. Lett., vol. 16, no. 12, pp. 1949-1953, Dec. 2019.

[28] M. Lv, G. Zhou, M. He, A. Chen, W. Zhang, and Y. Hu, "Maize Leaf Disease Identification Based on Feature Enhancement and DMS-Robust Alexnet," IEEE Access, vol. 8, pp. 57952-57966, Mar. 2020.

[29] L. Xia et al., “MNSIM: Simulation Platform for Memristor-Based Neuromorphic Computing System,” IEEE Trans. Comput.-Aided Des. Integr. Circuits Syst., vol. 37, no. 5, pp. 1009-1022, May 2018.
[30] Y. Cai, T. Tang, L. Xia, B. Li, Y. Wang, and H. Yang, “Low Bit-Width Convolutional Neural Network on RRAM,” IEEE Trans. Comput.-Aided Des. Integr. Circuits Syst., vol. 39, no. 7, pp. 1414-1427, July 2020.
[31] S. Ambrogio et al., “Neuromorphic learning and recognition with one-transistor-one-resistor synapses and bistable metal oxide RRAM,” IEEE Trans. Electron Devices, vol. 63, no. 4, pp. 1508-1515, Apr. 2016.
[32] B. K. Mohanty and P. K. Meher, “Memory efficient modular VLSI architecture for high throughput and low-latency implementation of multilevel lifting 2-D DWT,” IEEE Trans. Signal Process., vol. 59, no. 5, pp. 2072–2084, 2011.
[33] X. Ji, Z. Dong, G. Zhou, C. S. Lai, Y. Yan, and D. Qi, “Memristive system based image processing technology: a review and perspective,” Electronics, vol. 10, no. 24, pp. 3176, Dec. 2021.
[34] Z. Dong, C. S. Lai, D. Qi, Z. Xu, C. Li, and S. Duan, “A general memristor-based pulse coupled neural network with variable linking coefficient for multi-focus image fusion,” Neurocomputing, vol 308, pp. 172-183, Sep. 2018.
[35] R. Zhu, S. Chang, H. Wang, Q. Huang, J. He, and F. Yi, “A versatile and accurate compact model of memristor with equivalent resistor topology,” IEEE Electron Device Lett., vol. 38, no. 10, Oct. 2017.
[36] M. Bettayeb, F. Zayer, H. Abunahla, G. Gianini, and B. Mohammad, “An efficient in-memory computing architecture for image enhancement in AI applications,” IEEE Access, vol. 10, pp. 48229-48241, May 2022.
[37] Y. Ma et al, “Structure and illumination constrained GAN for medical image enhancement,” IEEE Trans. on Med. Imag., vol. 40, no. 12, pp. 3955-3967, 2021.
[38] T. Shijimaya et al, “Usefulness of texture and color enhancement imaging (TXI) in early gastric cancer found after helicobacter pylori eradication,” Sci. Rep. 13, Article No. 6899, 2023.
[39] C. Yakopcic, T. M. Taha, G. Subramanyam, R. E. Pino, and S. Rogers, “A memristor device model,” IEEE Electron Device Lett., vol. 32, no. 10, pp. 1436–1438, Oct. 2011.
[40] M. Prezioso, F. Merrikh-Bayat, B. D. Hoskins, G. C. Adam, K. K. Likharev, and D. B. Strukov, “Training and operation of an integrated neuromorphic network based on metal-oxide memristors,” Nature, vol. 521, pp. 61-64, 2015.
[41] K. A. Navas, M. C. Ajay, M. Lekshmi, T. S. Archana, and M. Sasikumar, “DWT-DCT-SVD based watermarking,” in Proc. 2008 3rd International Conference on Communication Systems Software

and Middleware and Workshops (COMSWARE '08), 2008, pp. 271-274.
[42] N. Remenyi, O. Nicolis, G. Nason, and B. Vidakovic, “Image denoising with 2d scale-mixing complex wavelet transforms,” IEEE Trans. Image Process, vol. 23, no. 12, pp. 5165-5174, 2014.
[43] V. Duris, S. G. Chumarov, G. M. Mikheev, K. G. Mikheev, and V. I. Semenov, “The orthogonal wavelets in the frequency domain used for the images filtering,” IEEE Access, vol. 8, pp. 211125-211134, Nov. 2020.
[44] T. S. Kumar and V. Kanhangad, “Face recognition using two-dimensional tunable-Q wavelet transform,” in Proc. Int. Conf. Digit. Image Comput., Techn. Appl. (DICTA), 2015, pp. 1-7.
[45] J. Gilles, G. Tran, and S. Osher, “2D Empirical Transforms. Wavelets, Ridgelets, and Curvelets Revisited” SIAM Journal on Imaging Sciences, vol. 7, no. 1, pp.157-186, 2014.
[46] K. Jyoti, M. K. Gautam, S. Kumar, S. Sushma, R. B. Pachori, and S. Mukherjee, “Memristive crossbar array-based computing framework Via DWT for biomedical image enhancement,” IEEE Tran. Emerg. Topics Comp., doi: 10.1109/TETC.2023.3318303.
[47] A. Karlekar and A. Seal, “SoyNet: Soybean leaf diseases classification,” Computers and Electronics in Agriculture, vol. 172., p. 105342, May 2020. doi: 10.1016/j.compag.2020.105342.
[48] T. E. Posch, “The wave packet transform (WPT) as applied to signal processing.” Proceedings of the IEEE-SP International Symposium on Time-Frequency and Time-Scale Analysis. IEEE, 1992.
[49] K. Gnawali and S. Tragoudas, “High-speed memristive ternary content addressable memory,” IEEE Trans. Emerg. Topics Comput., pp. 1-1, May 2021.
[50] I. Vourkas, D. Stathis, and G. Ch. Sirakoulis, “Massively parallel analog computing: ariadne’s thread was made of memristors,” IEEE Trans. Emerg. Topics Comput., vol. 6, no. 1, pp. 145-155, Apr. 2015.
[51] R.B. Pachori, “Time-frequency analysis techniques and their applications,” CRC Press, 2023.
[52] E. Hostalkova, O. Vysata, and A. Prochazka, “Multi-dimensional biomedical image de-noising using Haar transform,” in Proc. Int. Conf. Digital Signal Processing, 2007, pp. 175-178.
[53] K. A. Johnson and J.A. Becker. (1999), The whole brain atlas.
[54] E. Soares, P. Angelov, S. Biaso, M. H. Froes, and D. K. Abe, SARS-CoV-2 Identification.
[55] K. H. Talukder and K. Harada, “Haar wavelet-based approach for image compression and quality assessment of compressed image,” Int. J. Appl. Mathematics, vol. 36, no. 1, Oct. 2010.
[56] L. Chua “Resistance switching memories are memristors,” Appl. Phys. A, vol. 102, pp. 765-783, Jan. 2011.
[57] I. Avcibas, B. Sankur, and K. Savood, “Statistical evaluation of image quality measures,” J. Electron. Imag., vol. 11, no. 2, pp. 206-223, Apr. 2002.

[58] U. Sara, M. Akter, and M. S. Uddin, “Image quality assessment through fsim, ssim, mse and psnr-a comparative study,” J. Comp. Commun., vol. 7, pp. 8-18, 2019.
[59] L. Fan, F. Zhang, H. Fan, and C. Zhang, “Brief review of image denoising techniques,” Vis. Comput. Ind., Biomed., vol. 2, no. 1, pp. 1–12, Dec. 2019.
[60] R. Ramos, B. V. Salas, R. Zlatev, M. S. Wiener, and J. M. B. Rull, “The discrete wavelet transform and its application for noise removal in localized corrosion measurements,” Int. J. Corros., vol. 2017, pp. 1-7, Jun. 2017.
[61] L. Brechet, M. Lucas, C. Doncarli, and D. Farina, “Compression of biomedical signals with mother wavelet optimization and best-basis wavelet packet selection,” IEEE Trans. Bio. Eng., vol. 54, no. 12, pp. 2186-2192, Dec. 2007.
[62] R. Patel, V. Kumar, V. Tyagi, and V. Asthana, “A fast and improved compression technique using huffman coding,” in Proc. IEEE Int. Conf. WiSPNET, 2016, pp. 2283-2286.
[63] N. Singla and S. Sharma, “A review on wavelet based compression using medical images,” International Journal of Innovative Resercher in computer and communication Engineering, vol. 1, no. 8, Oct. 2013.
[64] V. K. Mishra, A. Kumar, and A. k. Jaiswal, “Performance comaprison of daubechies, biorthogonal and haar transform for grayscale image compression,” Int. J. Comput. Appl., vol.- 126, no. 9, Sep. 2015.
[65] M. Khalid, S. Mukhtar, M. J. Siddique, and S.F. Ahmed, “Memristor based full adder circuit for better performance,” Trans. Electr. Electron. Mater. vol. 20, pp. 403-410, Aug. 2019.
[66] H. . Su et al., “Multilevel threshold image segmentation for COVID-19 chest radiography: A framework using horizontal and vertical multiverse optimization,” Comput Biol Med., vol. 146, Jul. 2022.
[67] H. C. Shin et al., “Deep Convolutional Neural Networks for Computer-Aided Detection: CNN Architectures, Dataset Characteristics and Transfer Learning,” IEEE Trans. Med. Imag., vol. 35, no. 5, pp. 1285-1298, May 2016.
[68] X. Tian and C. Chen, “Modulation Pattern Recognition Based on Resnet50 Neural Network,” in 2nd IEEE Inter. Conf. on Infor. Commu. Signal Process. (ICICSP), pp 34-38, 2019.
[69] M. Wang and X. Gong, “Metastatic Cancer Image Binary Classification Based on Resnet Model,” 2020 IEEE 20th Inter. Conf. on Commu. Techn. (ICCT), Dec. 2020, pp. 1356-1359.
[70] C. Wang, L. Yu, X. Zhu, J. Su, and F. Ma, “Extended ResNet and Label Feature Vector Based Chromosome Classification,” IEEE Access, vol. 8, pp. 201098-201108, Oct. 2020.
[71] A. Krizhevsky, I. Sutskever, and G. E. Hinton, “Imagenet classification with deep convolutional neural networks,” Association for Computing Machinery, vol. 60, no. 6, pp. 84-90, Jun. 2017.

[72] N. Davari, G. Akbarizadeh, and E. Mashhour, “Corona Detection and Power Equipment Classification based on GoogleNet-AlexNet: An Accurate and Intelligent Defect Detection Model based on Deep Learning for Power Distribution Lines,” IEEE Trans. Power Delivery, pp. 1-1, Sep. 2021.
[73] Jing Sun, Xibiao Cai, Fuming Sun, and J. Zhang, “Scene image classification method based on Alex-Net model,” 2016 3rd Inter. Conf. Inform. and Cybern. for Comput.l Social Syst. (ICCSS), Jan. 2016, pp. 363-367.
[74] Z. Dong et al., “Convolutional neural networks based on RRAM devices for image recognition and online learning tasks,” IEEE Trans. Electron Devices, vol. 66, no. 1, pp. 793-801, Jan. 2019.
[75] S. N. Truong, S. H. Shin, S. D. Byeon, J. S. Song, and K. S. Min, “New twin crossbar architecture of binary memristors for low-power image recognition with discrete cosine transform,” IEEE Trans. Nanotechnol., vol. 14, no. 6, pp. 1104-1111, Nov. 2015.
[76] J. S. Pannu et al., “Design and Fabrication of Flow-Based Edge Detection Memristor Crossbar Circuits1,” IEEE Trans. on Circuits and Systems II, vol. 67, no. 5, pp. 961-965, May 2020.
[77] S. Yin, X. Sun, S. Yu, and J. -S. Seo, “High-Throughput In-Memory Computing for Binary Deep Neural Networks With Monolithically Integrated RRAM and 90-nm CMOS,” IEEE Trans. Electron Devices, vol. 67, no. 10, pp. 4185-4192, Oct. 2020.
[78] D. Garbin et al., “HfO2-based OxRAM devices as synapses for convolutional neural networks,” IEEE Trans. Electron Devices, vol. 62, no. 8, pp. 2494-2501, Aug. 2015.
[79] J. J. Wang et al., “Handwritten-Digit Recognition by Hybrid Convolutional Neural Network based on HfO2 Memristive Spiking-Neuron,” Sci. Rep., vol. 8, Aug. 2018, Art. no. 12546.
[80] S. Duan et al., “Memristor-based cellular nonlinear/neural network: design, analysis, and applications,” IEEE Trans. Neural Netw. Learn. Syst., vol. 26, no. 6, pp. 1202-1213, Jun. 2015.
[81] L. Wang, Z. Q. Lin, and A. Wong, “COVID-net: A tailored deep
convolutional neural network design for detection of COVID-19 cases from chest X-ray images,” Sci. Rep., vol. 10, no. 1, Dec. 2020, Art. no. 19549.
[82] A. Haghanifar, M. M. Majdabadi, and S. Ko, “COVID-CXNet: Detecting COVID-19 in Frontal Chest X-ray Images using Deep Learning,” ArXiv, abs/2006.13807, 2020.
[83] S. H. Wang et al., “COVID-19 classification by CCSHNet with deep fusion using transfer learning and discriminant correlation analysis,” Inf Fusion. Vol. 68, pp. 131-148, Apr. 2021.
[84] L. Wang, Z. Q. Lin, A. Wong, “Covid-net: A tailored deep convolutional neural network design for detection of covid-19 cases from chest X-ray images,” Scientific Reports, vol. 10, pp. 1-12, May 2020.

[85] L. Li et al., “Using artificial intelligence to detect COVID-19 and community-acquired pneumonia based on pulmonary CT: evaluation of the diagnostic accuracy,” Radiology vol. 296, no. 2, Mar. 2020.

[86] S. Kumar, R. Agrawal, M. Das, K. Jyoti, P. Kumar, and S. Mukherjee, “Analytical model for memristive systems for neuromorphic computation,” J. Phys. D: Appl. Phys., vol. 54, no. 35, Jun. 2021.

[87] G. Hu, L. Liu, D. Tao, J. Song, K.T. Tse, and K.C.S. Kwok, “Deep learning-based investigation of wind pressures on tall building under interference effects,” J. Wind Eng. Indust. Aerodyna., vol. 201, pp. 104138, Jun. 2020.

[88] A. Bhattacharyya et al., “A multi-channel approach for cortical stimulation artefact suppression in depth EEG signals using time-frequency and spatial filtering,” IEEE Trans. Biomed. Eng., vol. 66, no .7, pp. 1915-1926, Jul. 2018.

[89] H. Li et al., “3-D resistive memory arrays: From intrinsic switching behaviors to optimization guidelines,” IEEE Trans. Electron Devices, vol. 62, no. 10, pp. 3160-3167, Oct. 2015.

[90] M. Das, A. Kumar, R. Singh, M. T. Htay, and S. Mukherjee, “Realization of synaptic learning and memory functions in Y2O3 based memristive device fabricated by dual ion beam sputtering Nanotechnology,” Nanotechnology, vol. 29, pp. 1–9, 2018.

[91] L. A. Dalton, “Optimal ROC-Based classification and performance
analysis under Bayesian uncertainty models,” IEEE/ACM Trans. Comput. Biol. Bioinfo., vol. 13, no. 4, pp. 719-729, Jul. 2016.

[92] G. Jia, H.-K. Lam, and Y. Xu, “Classification of COVID-19 chest X-Ray and CT images using a type of dynamic CNN modification method,” Comput. Biol. Med. vol. 134, Jul. 2021.

[93] A. Badawi and K. Elgazzar, “Detecting Coronavirus from Chest X-rays Using Transfer Learning,” COVID 2021, vol. 1, no. 1, pp. 403-415, Sep. 2021.

[94] Y. Oh, S. Park, and J. C. Ye, “Deep learning COVID-19 features on CXR using limited training data sets,” IEEE Trans. Med. Imag., vol. 39, no. 8, pp. 2688-2700, Aug. 2020.

[95] A. Haghanifar et al., “COVID-CXNet: Detecting COVID-19 in frontal chest X-ray images using deep learning,”Multimed Tools Appl, 2022.

[96] D. T. Pham, “ Classification of COVID-19 chest X-rays with deep learning: new model or fine tuning? ,” Health information science and systems, vol. 9, no. 12. 22 Nov. 2020, doi:10.1007/s13755-020-00135-3.

[97] P.K.Sethy, S.K.Behera, P.K.Ratha, P. Biswas, “Detection of Coronavirus Disease (COVID-19) based on Deep Feature and support vector Machine,” International journal of mathematical engineering and management sciences, vol. 5(4), pp. 643-651, Article ID: 725526, 2002.

[98] M.Z.C. Azemin, R. Hassan, M.I.M. Tamrin, and M.A.M.Ali, “COVID-19 Deep Learning Prediction Model Using Publicily Avaible Radiologist- Adjdicated Chest X-ray Images as Training Data: Preliminary Findings,” International Journal of biomedical imaging,” Article id 8828855, 7 pages, 2020.
[99] V. Madaan et al., “ XCOVNet: Chest X-ray Image Classification for COVID-19 Early Detection Using Convolutional Neural Networks,” New Gener. Comput. Vol. 39, pp. 583–597, 2021.
[100] J. E. Lujan-García, M. A. Moreno-Ibarra, Y. Villuendas-Rey, C. Yáñez-Márquez, “ Fast COVID-19 and Pneumonia Classification Using Chest X-ray Images,”Mathematics, vol. 8, no. 1423, 2020.
[101] M.Imani, “ Automatic diagnosis of coronavirus (COVID-19) using shape and texture characteristics extracted from X-Ray and CT-Scan images,” Biomed Signal Process Control, vol. 68, p. 102602, Jul. 2021.
[102] G.Y.Kim, J.Y.Kim, C.H.Kim, and S.M.Kim, “ Evaluation of deep learning for COVID-19 diagnosis: Impact of image dataset organization,” Journal of Applied Clinical Medical Physics, vol. 22, issue 7, page 297-305, Jul. 2021.
[103] Y. Oh, S. Park, J. C. Ye, “Deep learning COVID-19 features on CXR using limited training data sets,” IEEE Trans. Med. Imaging, vol. 39, no. 8, pp. 2688–2700, May 2020.
[104] K. Hu et al, “Colorectal polyp region extraction using saliency detection network with neutrosophic enhancement,” Comput Biol Med., vol. 147, Aug. 2022.
[105] K. P. Noronha, U. R. Acharya, K. P. Nayak, R. J. Martis, and S. V. Bhandary, “Automated classification of glaucoma stages using higher order cumulant features,” Biomed. Signal Process. Control, vol. 10, no. 1, pp. 174-183, Mar. 2014.
[106] R. C. Gonzalez, R. E. Woods, “Digital image processing,” Publ. House Electron. Ind., 141 (7), 2002.
[107] S. Maheshwari, V. Kanhangad, R.B. Pachori, S.V. Bhandary, and U.R. Acharya, “Automated glaucoma diagnosis using bit-plane slicing and local binary pattern techniques,” Comput. Biol. Med., vol. 105, pp. 72–80, Feb. 2019.
[108] S. Phasuk et al., “Automated glaucoma screening from retinal fundus image using deep learning,” 2019 41st Annual Inter. Conf. IEEE Eng. Med. Bio. Society (EMBC), Berlin, Germany, Jul. 2019, pp. 904-907.
[109] U. R. Acharya et al., “Decision support system for the glaucoma using Gabor transformation,” Biomed. Signal Process. Control, vol. 15, pp. 18-26, Jan. 2015.
[110] L. Abdel-Hamid, “Glaucoma Detection from Retinal Images Using Statistical and Textural Wavelet Features,” J Digit Imaging, vol. 33, no. 1, pp. 151–158, Feb. 2020.
[111] K. Gopalan, T. R. Anderson, and E. J. Cupples, “A comparison of speaker identification results using features based on cepstrum

and Fourier- Bessel expansion," IEEE Trans. Speech Audio Proc., vol. 7, no. 3, pp. 289–294, May 1999.

[112] P. Suresh, T. Thayaparan, T. Obulesu, and K. Venkataramaniah, "Extracting micro-doppler radar signatures from rotating targets using Fourier–Bessel transformand time–frequency analysis," IEEE Trans. Geo. Remote Sen., vol. 52, no. 6, pp. 3204-3210, Jun. 2014.

[113] P. L. Nunez, "Representation of evoked potentials by Fourier-Bessel expansions," IEEE Tran. Biomed. Eng. BME, vol. 20, no. 5, pp. 372-374, Sep. 1973.

[114] Y. Zhou, J. Xu, Q. Liu, C. Li, Z. Liu, M. Wang, H. Zheng, and S. Wang, "A radiomics approach with CNN for shear-wave elastography breast tumor classification," IEEE Trans. Biomed. Eng., 65, 9, pp. 1935–1942, Sep. 2018.

[115] H. Fu et al., "Disc-aware ensemble network for glaucoma screening from fundus image," IEEE Trans. Med. Imaging, vol. 37, no. 11, pp. 2493/2501, Nov. 2018.

[116] C. Merkel et al., "Neuromemristive systems: Boosting efficiency through brain-inspired computing," Computer, vol. 49, no. 10, pp. 56-64, Oct. 2016.

[117] T. Kohler, A. Budai, M. F. Kraus, J. Odstrčilik, G. Michelson, and J. Hornegger, "Automatic no-reference quality assessment for retinal fundus images using vessel segmentation," Proc. 26th IEEE Int. Symp. Computer-Based Med. Systems, Porto, Portugal, Jun. 2013, pp. 95-100.

[118] N. Akter, S. Perry, J. Fletcher, M. Simunovic, and M. Roy, "Automated artifacts and noise removal from optical coherence tomography images using deep learning technique," 2020 IEEE Symp. Series Comp. Intell. (SSCI), Canberra, ACT, Australia, Dec. 2020, pp. 2536-2542.

[119] Z. Yu et al. "Retinal image synthesis from multiple-landmarks input with generative adversarial networks," Biomed. Eng. online, vol. 18, no.1, pp. 1-15, May 2019.

[120] M. Das, A. Kumar, S. Kumar, B. Mandal, M. A. Khan, and S. Mukherjee, "Effect of surface variations on the performance of yttria based memristive system," IEEE Electron Device Letters, vol. 39, no. 12, pp. 1852-1855, 2018.

[121] S. Qian and D. Chen, "Decomposition of the Wigner-Ville distribution and time-frequency distribution series," IEEE Trans. Signal Process., vol. 42, no. 10, pp. 2836-2842, Oct. 1994.

[122] F. Sattar and G. Salomonsson, "The use of a filter bank and the Wigner- Ville distribution for time-frequency representation," IEEE Trans. Signal Process., vol. 47, no. 6, pp. 1776-1783, Jun. 1999.

[123] Sonali, S. Sahu, A. K. Singh, S.P. Ghrera, and M. Elhoseny, "An approach for de-noising and contrast enhancement of retinal fundus image using CLAHE," Optics & Laser Tech., vol. 110, pp. 87-98, Feb. 2019.

[124] G. Lazaridis, M. Lorenzi, S. Ourselin, and D. G. Heath, “Improving statistical power of glaucoma clinical trials using an ensemble of cyclical generative adversarial networks,” Med. Image Analysis, vol. 68, pp. 101906, Feb. 2021.
[125] H. S. L. Chen et al., “Early glaucoma detection by using style transfer to predict retinal nerve fiber layer thickness distribution on the fundus photograph,” Ophthalmology Sci., vol. 2, no. 3, pp. 100180, Sep. 2022.
[126] U. R. Acharya, S. Dua, X. Du, S. V. Sree, and C. K. Chua, “Automated diagnosis of glaucoma using texture and higher order spectra features,” IEEE Trans. Inf. Technol. Biomed., vol. 15, no. 3, pp.449–455, May. 2011.
[127] R. Bock, J. Meier, L.G. Nyúl, J. Hornegger, and G. Michelson, “Glaucoma risk index: automated glaucoma detection from color fundus images,” Med. Image Anal., vol. 14, no. 3, pp. 471–481, Jun. 2010.
[128] X. Luo, J. Li, M. Chen, X. Yang, and X. Li, “Ophthalmic disease detection via deep learning with a novel mixture loss function,” IEEE Jour. Biomed. Health Infor., vol. 25, no. 9, pp. 3332-3339, Sep. 2021.
[129] Y. George, B. J. Antony, H. Ishikawa, G. Wollstein, J. S. Schuman, and R. Garnavi, “Attention-Guided 3D-CNN framework for glaucoma detection and structural-functional association using volumetric images,” IEEE Jour. Biomed. Health Infor., vol. 24, no. 12, pp. 3421-3430, Dec. 2020.
[130] The United Nations World Water Development Report. Wastewater: The Untapped Resource, UNESCO.2017. Available from: https://unesdoc.unesco.org/ark:/48223/pf0000247153
[131] Li, Ruhui, and John S Hartung. “Reverse transcription-polymerase chain reaction-based detection of plant viruses.” Current protocols in microbiology, Chapter-16, 2007. doi:10.1002/9780471729259.mc160 1s6.
[132] Edwards, M. L., and J. I. Cooper. 1985. Plant virus detection using a new form of indirect ELISA, J. Virol. Methods, vol. 11, pp. 309–319, 1985. https://doi.org/10.1016/0166-0934(85)90024-2
[133] Meyer, R., Chardonnens, F., Hübner, P., & Lüthy, J. (1996). Polymerase chain reaction (PCR) in the quality and safety assurance of food: detection of soya in processed meat products. Zeitschrift fur Lebensmittel-Untersuchung und -Forschung, vol. 203(4), pp. 339–344. https://doi.org/10.1007/BF01231072
[134] Priya P. and Dony A. D souza, “Study of feature extraction techniques for the detection of diseases of agricultural products,” International Journal of Innovative Research in Electrical, Electronics, Instrumentation and Control Engineering, Vol.3, Issue.1, pp-4-8, 2015.
[135] Kanjalkar, P. H. & Lokhande, S. S. “Detection and Classification of Plant Leaf Diseases using ANN.” International Journal of Scientific & Engineering Research, Vol. 4, No. 8,2013.

[136] Shrivastava, S., & Hooda, D.S., Automatic Brown Spot and Frog Eye Detection from the Image Captured in the Field, American Journal of Intelligent Systems, Vol. 4 No. 4, 2014, pp. 131-134.

[137] A. Singh Rajput, S. Shukla, and S. S. Thakur, “Soybean leaf diseases detection and classification using recent image processing techniques,” ijsrtm, vol. 8, no. 3, pp. 01-08, Jul. 2020.

[138] E. C. Tetila et al., "Automatic Recognition of Soybean Leaf Diseases Using UAV Images and Deep Convolutional Neural Networks," IEEE Geoscience and Remote Sensing Letters, vol. 17, no. 5, pp. 903-907, May 2020, doi: 10.1109/LGRS.2019.2932385

[139] E. Miao, G. Zhou, and S. Zhao, “Research on Soybean Disease Identification Method Based on Deep Learning”, Mobile Information Systems, vol. 2022. Hindawi Limited, pp. 1–8, Aug. 22, 2022. doi: 10.1155/2022/1952936.

[140] Shrivastava, S., Singh, S.K., Hooda, D.S.: “Statistical texture and normalized discrete cosine transform-based automatic soya plant foliar infection cataloguing”, Br. J. Math. Comput. Sci., vol. 4, (20), pp. 2901–2916, 2014.

[141] J. A. Pandian, V. D. Kumar, O. Geman, M. Hnatiuc, M. Arif, and K. Kanchanadevi, “Plant Disease Detection Using Deep Convolutional Neural Network,” Applied Sciences, vol. 12, no. 14, p. 6982, Jul. 2022, Doi: 10.3390/app12146982.

[142] Reyes, Angie K. et al. “Fine-tuning Deep Convolutional Networks for Plant Recognition.” Conference and Labs of the Evaluation Forum, 2015.

[143] Mohanty, Sharada P et al. “Using Deep Learning for Image-Based Plant Disease Detection.” Frontiers in plant science, vol. 7, 1419, 2016, doi:10.3389/fpls.2016.01419

[144] S. Gharge, P. Singh,: “Image processing for soybean disease classification and severity estimation”, Emerging research in computing, information, communication and applications, (Springer, New Delhi, India), pp. 493–500, 2016.

[145] J. Gui , M. Mbaye, “Identification of Soybean Leaf Spot Diseases using Deep Convolutional Neural Networks,” International Journal Of Engineering Research & Technology (IJERT) ,Vol. 08, Issue 10, 2019.

[146] S.G. Mallat, “A theory for multiresolution signal decomposions: The wavelet representation”, IEEE Transactions on Pattern Analysis and Machine Intelligent, vol.11, pp 674-693. July 1989.

[147] C. Vimalraj, S. S. Blessia and S. Esakkirajan, "Image compression using wavelet packet and singular value decomposition," IEEE International Conference on Computational Intelligence & Computing Research, Coimbatore, India, 2012, pp. 1-6, doi: 10.1109/ICCIC.2012.6510184.

[148] A. Prakash, “Wavelet and its applications,” Int. J. Sci. Res. Comput. Sci. Eng. Inf. Technol, vol. 3, no. 8, pp. 95-108, Nov. 2018.

[149] T. Fan, “Research and realization of video target detection system based on deep learning,” International Journal of Wavelets, Multiresolution and Information Processing, vol. 18, no. 01, Article ID 1941010, 2020.
[150] He, K., Zhang, X., Ren, S., Sun, J., “Deep residual learning for image recognition”, Proceedings of the IEEE Conference on Computer Vision and Pattern Recognition, pp.770–778,2016.
[151] Szegedy et al., “Going deeper with convolutions”, Proceedings of the IEEE Conference on Computer Vision and Pattern Recognition, pp. 1–9,2015.
[152] Huang, Gao et al. “Densely Connected Convolutional Networks.” 2017 IEEE Conference on Computer Vision and Pattern Recognition (CVPR), pp. 2261-2269,2016.
[153] LeCun et al., “Gradient-based learning applied to document recognition”, Proceedings of the IEEE, vol. 86(11), 2278–2324, 1998.
[154] F. Chollet, “Xception: Deep Learning with Depthwise Separable Convolutions,” IEEE Conference on Computer Vision and Pattern Recognition (CVPR), IEEE, Jul-2017.